Isomeric ratios of high-spin states in neutron-deficient N≈126 nuclei produced in projectile fragmentation reactions

Ana María Denis Bacelar

A thesis submitted for the degree of
Doctor of Philosophy

2012

UNIVERSITY OF BRIGHTON

Declaration of Authorship

I declare that the research contained in this thesis, unless otherwise formally indicated within the text, is the original work of the author. The thesis has not been previously submitted to this or any other university for a degree, and does not incorporate any material already submitted for a degree.

Signed: _____

Date: _____

"There are two possible outcomes. If the results confirm the hypothesis, then you have made a measurement. If the results are contrary to the hypothesis, then you have made a discovery."

Enrico Fermi

UNIVERSITY OF BRIGHTON

Abstract

School of Engineering, Mathematics and Computing

Doctor of Philosophy

by Ana María Denis Bacelar

The population of high-spin isomeric states in neutron-deficient N≈126 nuclei has been studied in order to further understand the reaction mechanism of projectile fragmentation. The nuclei of interest were populated following projectile-fragmentation of a 1 GeV/A ^{238}U beam on a ^{9}Be target at GSI, Germany. The reaction products were selected and separated in the FRS FRagment Separator and brought to rest in an 8 mm plastic stopper placed at the focus of the RISING gamma-ray detector array. The results on the development of an add-back method for the RISING array are presented and discussed for source and in-beam data.

Twenty four previously studied nuclei with 84≤Z≤89 and 121≤N≤128 have been identified in four different FRS magnetic rigidity settings. Intensities of gamma-rays emitted in the decay of isomeric states with half-lives between 100 ns and 40 μs have been measured and used to obtain the corresponding isomeric ratios. Such ratios provide information on the probability of a nucleus being produced in a reaction in a given state.

Projectile fragmentation reactions at relativistic energies can be described by the two stage abrasion-ablation model. In this model, the reaction is seen as clean cut of the projectile. It considers the angular momentum to be generated by the number of nucleons abraded in the abrasion stage, while the ablation stage has a negligible effect in the angular momentum distribution. The angular momentum population of a state with a given spin is obtained assuming that all the states above that level will decay into it. This is the so-called sharp-cut-off approximation, and it is justified for isomers close to the yrast line. This is the case for all the isomers studied in this work. Results on the ratio between experimental and theoretical isomeric ratios will be discussed in the framework of the abrasion-ablation model, considering that only the abrasion or both, the abrasion and ablation, contribute to the angular momentum distribution. This new data is of great interest for the production of radioactive beams in an isomeric state in present and future nuclear physics facilities.

Acknowledgements

This thesis would not have been possible without the help of many people, who in one way or another contributed to this work. First I offer my gratitude and special thanks to my supervisors Prof. Alison Bruce and Dr. Zsolt Podolyák, who have supported me throughout this thesis, offering me their guidance, patience and knowledge when needed. I also remember the guidance of numerous people at GSI, who kindly helped me during the sometimes exhausting experiments. I would also like to thanks the opportunity to exchange ideas with my colleagues from the University of Surrey, who also helped me forgetting my days as the only student at Brighton, making me feel as part of their group. You all know who you are.

I can not end these acknowledgements without thinking of Chosbie, who cunningly did part of my coding with her little paws every time I would get up for a cup of tea. All those hours of 'fun' trying to find out which line of my code she had decided to conquer with her ideas! Also Quackers and Woofs are in my mind, the songs we sang together while trying to get me up in the morning will not be forgotten. And of course, L., thank you! You have been the best discovery during this time. and as you know I always say...when life begins to end it is better to call it buuu, or it gets nasty!

I would like to acknowledge the financial support of the Engineering and Physical Sciences Research Council (EPSRC), who funded my Ph.D studies.

Finally, my most sincere 'gracias' goes to my parents and brother, Maria Jesús, Manuel and Jose, for their love and support during this long journey.

A mi madre, padre y hermano con todo mi amor y cariño

Contents

List of Figures

List of Tables

Resumen en castellano

La población de estados isoméricos con alto spin en núcleos deficientes de neutrones con N≈126 ha sido estudiada con el fin de entender en más profundidad el mecanismo de reacción de la fragmentation de proyectiles. Los núcleos de interés fueron poblados después de una reaccion de fragmentación de un haz de ^{238}U con una energía de 1 GeV/A en un blanco de ^{9}Be, en el laboratorio GSI, Germany. Los productos de reacción fueron seleccionados y separados en el separador de fragmentos FRS, y frenados en una lámina de plástico de 8 mm colocada en el foco de la red de detectores de rayos gamma RISING. Los resultados sobre el desarrollo de un método add-back para RISING son presentados y discutidos para los datos obtenidos de fuentes radiactivas y de las reacción de fragmentación.

Veinticuatro núcleos estudiados previamente, con 84≤Z≤89 y 121 ≤N≤128, han sido identificados en cuatro diferentes configuraciones de rigidez magnética del FRS. Las intensidades de los rayos gamma emitidos en la desintegración de estados isoméricos con una vida media de entre 100 ns y 40 μs han sido medidas y utilizadas para obtener las proporciones isoméricas correspondientes. Tales proporciones dan información sobre la probabilidad que un núcleo tiene de ser producido en una reacción en un estado dado.

Las reacciones de fragmentación de proyectiles a energías relativistas pueden ser descritas por el modelo de abrasión-ablación. En este modelo, la reacción se ve como un corte limpio del proyectil. Se considera que el momento angular es generado por el nmero de nucleones erosionados en la etapa de abrasión, mientras que la etapa de ablación tiene un efecto despreciable en la distribución del momento angular. La población de momento angular de un estado con un spin dado se obtiene suponiendo que todos los estados por encima de ese nivel se desintegran en él. Esta es la denominada aproximación de corte afilado, y está justificada para isómeros cerca de la línea yrast. Este es el caso para todos los isómeros estudiados en este trabajo. Los resultados sobre la relación entre las proporciones de isómeros experimentales y teóricos se discutirá en el marco del modelo de abrasión-ablación, considerando que sólo la abrasión o ambos, la abrasión y la ablación, constribuyen a la distribución del momento angular. Estos nuevos datos son de gran interés para la producción de haces radiactivos en un estado isomérico tanto en las actuales instalaciones de física nuclear como en futuras instalaciones como la de FAIR en GSI.

Introduction

One of the major challenges in nuclear physics is to understand the properties and structure of atomic nuclei in terms of the forces between the neutrons and protons. There are two main processes from which nuclei can be studied, natural radioactivity and nuclear reactions, both resulting in the emission of radiation. The number of natural elements is limited, which restricts the possible studies to only a few nuclei. Therefore, nuclear reactions are a more convenient method to study the nuclear properties. When the energy of the projectile is large enough to overcome the Coulomb barrier and the impact parameter is small, the projectile can penetrate the target. Depending on the impact parameter and the energies involved, different reaction channels are open, such as fusion-evaporation, fission, deep inelastic collision or fragmentation reactions [1]. In a fusion-evaporation reaction two nuclei combine to form a compound nucleus followed by nuclear evaporation decay, where neutrons, protons and α particles are emitted. These sort of reactions are best suited to produce nuclei with high-spin states, due to the large angular momentum involved. The angular momentum transferred to the compound nucleus depends on the impact parameter and the linear momentum of the beam. Fusion-evaporation cross sections decrease significantly for heavy nuclei, where fission becomes a more competitive decay mode. When the compound nucleus is a heavy nucleus, fission into two nuclei strongly competes with the evaporation of nucleons and light particles. If a compound nucleus has a large excitation energy and a greater angular momentum than a critical value (at which the fission barrier disappears), fission becomes the dominant process. When the angular momentum generated in the reaction is too large to produce a stable nucleus, a deep inelastic collision takes places and the projectile and target spend some time interacting and exchanging particles; but contrary to fusion, they do not form a compound nucleus. Other type of reactions are peripheral projectile fragmentation reactions, where a heavy projectile bombards a light target, creating a prefragment in an excited state that decays via nuclear evaporation or fission. Fragmentation reactions have been proved to be an excellent method of producing nuclei both near the stability line and proton and neutron-rich exotic nuclei [2]. They are used in nuclear astrophysics to study the elements produced in stellar nucleosynthesis and the formation of matter in stars by

supernova explosions [3]. These reactions are a powerful technique to produce intense secondary radioactive ion beams. Therefore, the knowledge of realistic models of fragmentation reactions are of great interest for present and future nuclear physics facilities, e.g. the Super-FRS at GSI [4].

The aim of reaction mechanism studies is to understand the processes behind the collision of two nuclei. The main observables to study for a fragmentation reaction are the production cross sections and the longitudinal momentum distributions, which have been studied extensively [5, 6]. However, there is not so much information about angular momentum population in these reactions. The aim of this work is to study the population of high-spin states produced in the projectile fragmentation of a heavy-ion projectile on a light target. Previous studies in this area have found that the theory underestimates the population of high-spin states produced in these reactions [7, 8, 9]. This thesis reports on neutron-deficient nuclei with N≈126 which have been populated following projectile fragmentation of a ^{238}U beam with energy 1 GeV/A on a ^{9}Be target [10]. The choice of this region of the nuclear chart (shown in Fig. 1) was not arbitrary, since nuclei with 84≤Z≤89 and 121≤N≤128 have a large number of high-spin isomeric states with half-lives suitable to be studied in flight (100ns-40μs).

89				^{206}Ac	^{207}Ac	^{208}Ac	^{209}Ac	^{210}Ac	^{211}Ac	^{212}Ac	^{213}Ac	^{214}Ac	**^{215}Ac**	^{216}Ac	^{217}Ac
88	^{202}Ra	^{203}Ra	^{204}Ra	^{205}Ra	^{206}Ra	^{207}Ra	^{208}Ra	^{209}Ra	**^{210}Ra**	**^{211}Ra**	**^{212}Ra**	^{213}Ra	**^{214}Ra**	**^{215}Ra**	^{216}Ra
87	^{201}Fr	^{202}Fr	^{203}Fr	^{204}Fr	^{205}Fr	^{206}Fr	^{207}Fr	**^{208}Fr**	^{209}Fr	^{210}Fr	**^{211}Fr**	**^{212}Fr**	**^{213}Fr**	**^{214}Fr**	^{215}Fr
86	^{200}Rn	^{201}Rn	^{202}Rn	^{203}Rn	^{204}Rn	^{205}Rn	^{206}Rn	^{207}Rn	^{208}Rn	^{209}Rn	**^{210}Rn**	**^{211}Rn**	**^{212}Rn**	**^{213}Rn**	**^{214}Rn**
85	^{199}At	^{200}At	^{201}At	^{202}At	^{203}At	^{204}At	^{205}At	^{206}At	^{207}At	**^{208}At**	**^{209}At**	**^{210}At**	**^{211}At**	^{212}At	^{213}At
84	**^{198}Po**	^{199}Po	**^{200}Po**	^{201}Po	^{202}Po	^{203}Po	^{204}Po	^{205}Po	**^{206}Po**	^{207}Po	**^{208}Po**	^{209}Po	^{210}Po	^{211}Po	^{212}Po
83	^{197}Bi	^{198}Bi	^{199}Bi	^{200}Bi	^{201}Bi	^{202}Bi	^{203}Bi	^{204}Bi	^{205}Bi	^{206}Bi	^{207}Bi	^{208}Bi	^{209}Bi	^{210}Bi	^{211}Bi
82	^{196}Pb	^{197}Pb	^{198}Pb	^{199}Pb	^{200}Pb	^{201}Pb	^{202}Pb	^{203}Pb	^{204}Pb	^{205}Pb	^{206}Pb	^{207}Pb	^{208}Pb	^{209}Pb	^{210}Pb
Z/N	114	115	116	117	118	119	120	121	122	123	124	125	126	127	128

Figure 1: *Region of the nuclear chart where this work is focused. The colour code of the chart indicates the decay mode of each nuclei, where black, blue, pink and yellow cells correspond to stable, electron capture and β^+, β^- and α decay respectively. Also, the closed shells at Z=82 and N=126 are indicated within the thicker border lines. The twenty four nuclei with 84≤Z≤89 and 121≤N≤128 studied in this work are indicated in red colour font.*

Isomeric decay spectroscopy is an excellent tool to study the reaction mechanism of fragmentation reactions. Due to the distance between production target and delayed gamma-ray detection, the separation and identification of the nuclei of interest is possible, which

in other cases would be difficult due to the large number of ions produced at the target position. This method is called in-flight separation [11], and it is only possible for long-lived nuclei or isomers. Since we are interested in studying heavy ions with Z>80, the majority of the ions have to be fully stripped to obtain a good isotopic separation. Therefore the GSI facility and the inverse-kinematics technique used there are best suited for this type of experiment, where relativistic energies up to 1 GeV/A are required.

Intensities of gamma-rays emitted in the decay of isomeric states have been measured and used to obtain the corresponding isomeric ratios, which provide information on the probability of a nucleus being produced in a reaction in a given state. In order to study fragmentation reactions, the experimental isomeric ratios are compared with the predictions of the abrasion-ablation model [12, 13]. Details of these models are presented in Chapter 1. Chapter 2 describes the experimental details. The data analysis is described in Chapter 3, with the results, and interpretation and conclusions presented in Chapters 4 and 5 .

Chapter 1

Fragmentation reaction models

A projectile fragmentation reaction is a collision between a heavy ion projectile and a light target. The evolution of heavy ion reactions at relativistic energies is usually described in terms of two different time scales [14].

1. **Fast stage ($\sim 10^{-23}$ s).** The collision between the reaction partners takes place. The target interacts with some of the nucleons from the projectile transfering them an amount of energy and momentum. As a consequence of all the nucleon-nucleon collisions taking place, some nucleons from the projectile escape and some keep interacting with their neighbours. Therefore, considering that the collision time between projectile and target is short compared with the time between collisions of the nucleons inside the nuclei, the process can be seen in terms of the collisions between the individual nucleons. Once the transferred energy is uniformly distributed all over the resulting nucleus, the system is considered to be in pre-equilibrium.

2. **Slow stage ($\sim 10^{-21}$ s at 200 MeV**). When the prefragment formed in the fast stage is thermalised, the de-excitation of the nucleus takes place through different competing channels:

   - Evaporation of nucleons and light particles.
   - Fission

The fast stage can be described in the framework of different models, such as hydrodynamic, kinematic, abrasion and intra-nuclear-cascade models. Hydrodynamic models [15, 16] consider the nucleus as a viscous fluid and are used to describe heavy ion collisions with a low impact parameter. The kinematic model [17, 18] is used to study spin polarization and spin alignment. The idea in this model is the same as in the abrasion model.

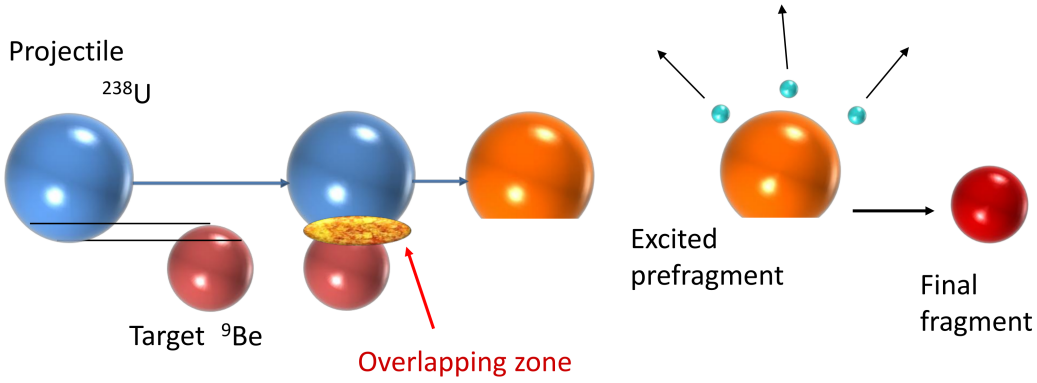

Figure 1.1: *A schematic of a heavy ion collision. In the first stage an excited prefragment is formed and in the second stage, the prefragment decays via particle evaporation or fission.*

It is based on a clean cut of the projectile and target during the collision. Using the conservation laws of linear and angular momenta, it is possible to obtain a relation between the momentum of the projectile and the internal angular momentum of the formed fragment. In the intra-nuclear cascade models (INC) [19, 20, 21] the reactions are described assuming a series of collisions between the nucleons in the projectile and all the individual nucleons in the target. Therefore this sort of model is commonly used to describe spallation reactions, where the projectile is defined by one nucleon which hits a heavy mass target at high energies. The slow stage is described using a statistical evaporation model, such as the ablation model. The following sections are focused on the abrasion-ablation model for the fast and slow stages, which is suitable to describe nucleus-nucleus collisions at relativistic energies.

1.1 Abrasion-ablation model

The abrasion-ablation model [12] is used to describe very peripheral fragmentation reactions. It comprises two stages, the fast abrasion stage followed by the ablation stage.

1.1.1 Abrasion stage

The abrasion model for relativistic heavy ion collisions is derived from Glauber's multiple scattering theory [22]. Glauber's formalism is used to describe nucleon-nucleus reactions at energies higher than 0.5 GeV per nucleon. The abrasion model, which was first introduced by Bowman, Swiatecki and Tsang [23], is a generalization of Glauber's theory for nucleus-nucleus collisions. It is based on a geometrical picture of the collision, where the projectile

is moving in a straight line and hits the target, leading to a clean cut of both reaction partners, as shown in Fig. 1.1. In the overlapping zone, many nucleon-nucleon collisions take place, while the non-overlapping zone is disturbed a little. This is justified at high energies, when the relative velocity between projectile and target is higher than the Fermi velocity of the nucleons. Therefore the excited prefragment continues its trajectory almost undisturbed.

The number of nucleons removed from the projectile or "abraded mass" is determined by the impact parameter of the reaction, and is proportional to the volume of the overlapping zone. For any given projectile-target combination, the abraded mass depends only on the impact parameter. It is assumed that an abraded nucleon has the same probability of being a proton or a neutron, and therefore the distribution of the neutron to proton ratio (N/Z) is obtained from statistical considerations. Under this assumption, the N/Z distribution of the prefragments remains the same as that of the projectile.

Originally the excitation energy of the preframents was determined by their excess surface energy [22]. However, it was found that this approximation underestimates the excitation energies and therefore a new statistical approach has been considered [12]. When the nucleons are abraded from the projectile, a number of single-particle levels are vacated and the excitation energy of the prefragment is calculated as the sum of the energies of the hole excitations. In order to obtain an estimation for the excitation energy, the nucleons are considered to move in a Woods-Saxon potential using the single-particle level density [24, 25].

The angular momentum distribution [13] of the nucleons removed during the abrasion stage is calculated by analogy with Goldhaber's description of the longitudinal momentum [26]:

$$\sigma^2 = \langle j_z^2 \rangle \frac{A'_f \left(A_p - A'_f \right)}{A_p - 1}, \tag{1.1}$$

where A_p and A'_f are the projectile and prefragment masses respectively. $\langle j_z^2 \rangle$ is the average square value of the z-projection of the angular momentum, and is calculated in a semi-classical consideration of the angular momentum for the square well potential:

$$\langle j_z^2 \rangle = 0.16 A_p^{2/3} \left(1 - \frac{2}{3}\beta \right), \tag{1.2}$$

where β is the quadrupole deformation parameter and the factor 0.16 is obtained from the Woods-Saxon potential, neglecting that the angular momentum distribution depends on the shape of the potential well and shell effects.

The number of hole excitations with angular momentum I is given by:

$$\rho_n\left(U,I\right)=\frac{2I+1}{2\sigma_n^2}exp\left(-\frac{I\left(I+1\right)}{2\sigma_n^2}\right)\rho_n\left(U\right), \tag{1.3}$$

where $\rho_n(U)$ is the total density of n-hole excitations, with excitation energy U, and σ is the so-called spin cut-off parameter which depends on the energy and the number of hole states [27].

Considering the state equations for U and σ, the spin cut-off parameter can be written in a similar way to Goldhaber's formula, allowing the calculation of the angular momentum distribution of n-hole excitations for a given excitation energy distribution.

$$\sigma_n^2=0.234\left(1-\frac{U}{n\epsilon_f}\right)A_p^{2/3}\frac{n\left(A_p-n\right)}{A_p-1}, \tag{1.4}$$

with ϵ_f the Fermi energy, n the number of hole states and with angular momentum projection:

$$\langle j_z^2\rangle=0.234\left(1-\frac{U}{n\epsilon_f}\right)A_p^{2/3}. \tag{1.5}$$

At the end of the abrasion stage, the excitation energy is redistributed in the prefragment of the compound nucleus. At this moment the prefragment is characterized by its excitation energy, mass, charge and angular momentum.

1.1.2 Ablation stage

During the ablation stage [28], if the excitation energy is above the particle emission threshold, the excited prefragment evaporates nucleons and light particles until the final fragment is formed, or it undergoes fission if the energy is above the fission barrier. At this stage it is considered that the evaporation of particles during the ablation stage does not modify the orbit of the nucleons in the formed prefragment. To prove this assumption, a calculation of the energy thermalised during the abrasion stage is done. According to some calculations [29, 30], the time required to reach the equilibrium is:

$$\tau\left(t\right)=\frac{2\times10^{-22}MeV\cdot s}{e^*\left(t\right)}, \tag{1.6}$$

where e* is the excitation energy per nucleon. Assuming that the deposited energy is linear as a function of time: e*=C_1t, with:

$$C_1=\frac{E'}{A't_1}, \tag{1.7}$$

where A′ and E′ are the mass and total excitation energy of the prefragment and t_1 the abrasion time. Thus the amount of energy which is not thermalised can be calculated from the equation:

$$\frac{de}{dt} = C_1 - \frac{e}{\tau}. \tag{1.8}$$

The results show that the fraction of energy thermalised in the prefragment during the abrasion is very small, about 10% [12]. Therefore it is assumed that the orbits of the nucleons remaining in the prefragment are not disturbed during the ablation.

In the Weisskopf-Ewing statistical approach used to describe the ablation stage, the change of angular momentum distribution is not treated because of the small angular momentum carried by the emitted nucleons and light particles. Therefore, the angular momentum distribution of the final fragments is the same as that of the prefragments, and can be calculated as follows:

$$\sigma\left(I\right) = \frac{2I+1}{2\sigma_f^2} exp\left(-\frac{I\left(I+1\right)}{2\sigma_f^2}\right), \tag{1.9}$$

where σ_f is the spin cut-off parameter of the final fragment. Assuming that the number of evaporated nucleons is proportional to the abraded mass, then the mass of the final fragment can be expressed as:

$$A_f = A_p - n\left(\nu+1\right), \tag{1.10}$$

where A_f and A_p are the final fragment and projectile masses, and ν represents the mean number of nucleons evaporated per abraded mass unit. Since the excitation energy induced per nucleon abraded is about 27 MeV [31] and the evaporation of one nucleon decreases this energy by 13 MeV, a parameter of $\nu = 2$ can be assumed, and the spin cut-off parameter can be written as follows:

$$\sigma_f^2 = 0.16 A_p^{2/3}\left(1 - \frac{2}{3}\beta\right)\frac{\left(A_p - A_f\right)\left(\nu A_p + A_f\right)}{\left(\nu+1\right)^2\left(A_p - 1\right)}. \tag{1.11}$$

The angular momentum distribution in peripheral fragmentation reactions at relativistic energies can be calculated using the ABRABLA Monte Carlo code, based on the abrasion-ablation model, continuously being developed at GSI, Germany. The code has been proven to provide good agreement between experiment and theory describing fragmentation reactions [32, 33, 34].

The angular momentum distribution of the fragmentation residues calculated using Eqs:1.9

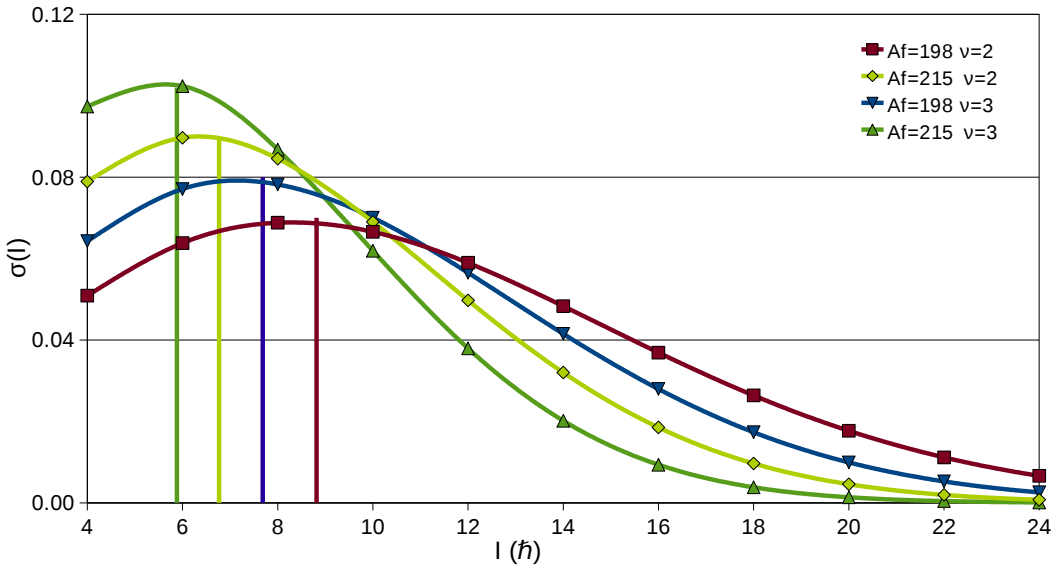

Figure 1.2: *Angular momentum distribution for fragments with mass 198 and 215 for ν=2 and 3, calculated using Eqs:1.9 and 1.11.*

and 1.11 is shown in Fig.1.2 using ν=2 and 3 to show the distribution varies. Mass fragments of A=198 and 215 have been used, as they are the lightest and heaviest nuclei measured in this work and it has been assumed that for both cases the nuclei are not deformed (β=0) and the projectile mass is 238. The spin cut-off is also shown as a vertical line for each case. The figure shows that as more nucleons are removed from the projectile the excitation energy increases and the angular momentum distribution becomes wider. The result of this is a larger probability of producing higher spin states. When the parameter ν is increased from 2 to 3 for the same mass number, the distribution becomes narrower.

1.2 Relativistic transport (ART) and Sequential Binary Decay (SBD) model

More recently, new calculations [35] have been performed in order to determine the angular momentum distribution in fragmentation reactions. This new approach is based on a combination of all the stages of the dynamical evolution. The first part of the collision is treated in the framework of a relativistic transport model (ART) which gives the size and excitation energy of the prefragment. These parameters are used as inputs into the ABRABLA code and the angular momentum distribution of the prefragment is obtained. During the second stage the prefragment undergoes statistical sequential binary decay (SBD) until the final stable fragment is formed.

1.3 Isomeric ratios

Experimentally we can determine only the total population of all the states decaying into the level of interest. This is quantified in terms of the isomeric ratio R_{exp}, which is defined as the probability that, following a reaction, a nucleus is produced in an isomeric state:

$$R_{exp} = \frac{Y}{N_{imp} F G}, \tag{1.12}$$

where N_{imp} is the number of implanted ions, F and G are correction factors and Y is the observed decay yield calculated as:

$$Y = \frac{N_\gamma \left(1 + \alpha_{tot}\right)}{E_{ff} b}, \tag{1.13}$$

where N_γ is the number of counts of the gamma line depopulating the isomer, α_{tot} and b are the total conversion factor and the absolute branching ratio, and E_{ff} the efficiency.

Due to decay losses as the ion travels from the formation point to the measuring station, the isomeric ratio has to be corrected for the time of flight:

$$F = exp\left[-\left(\lambda^{q_1}\frac{TOF_1}{\gamma_1} + \lambda^{q_2}\frac{TOF_2}{\gamma_2}\right)\right], \tag{1.14}$$

where TOF_1 (TOF_2) is the time-of-flight through the first (second) stage of the FRS [1] and γ_1 (γ_2) are the corresponding Lorentz factors. The TOF and Lorentz factor through the first part of the FRS are not determined experimentally, but obtained using the LISE code [36]. λ_1 (λ_2) is the decay constant for the charge state q_1 (q_2).

The finite detection efficiency correction factor is determined as:

$$G = exp\left(-\lambda t_i\right) - exp\left(-\lambda t_f\right), \tag{1.15}$$

where t_i and t_f are the gamma delay times used in the off-line analysis to produce the delayed-gamma spectra.

For fully stripped ions:

$$\lambda^0 = \lambda \sum_i \frac{b_i}{1 + \alpha_{tot}^i}. \tag{1.16}$$

where i is the number of transitions decaying from the energy level of interest.

[1] The FRS is the fragment separator where the reaction residues of interest are selected. It consists of two stages and detailed information is given in Chapter 2.

In some reactions more than one isomer is populated in the same nucleus and a lower-lying isomer can be fed by the delayed decay of the higher-lying isomer. If the upper state decays with probability b_{UL} to the lower state, the isomeric ratio of the lower-lying isomeric is determined as follows:

$$R^L_{exp} = \frac{Y_L}{N_{imp}F_L G_L} - b_{UL}\frac{R_U}{F_L G_L}\left[\frac{\lambda_L G_U - \lambda_U G_L}{\lambda_L - \lambda_U}F_U + \frac{\lambda^0_U}{\lambda^0_L - \lambda^0_U}G_L\left(F_U - F_L\right)\right] \quad (1.17)$$

where L and U represent the lower and upper-lying isomeric states.

In order to compare the experimental results with the predictions of the abrasion-ablation model, the theoretical calculation of the isomeric ratio assumes that all states with spin greater than that of the isomeric state ($I \geq I_m$) will decay into it. Therefore the theoretical value gives an upper limit, since there is always a probability of the nucleus decaying via a transition bypassing the isomer. This is called the sharp cut-off approximation and has been justified for isomers lying close in energy to the yrast line [13]. Integrating Eq. 1.9 between I_m and infinity, the probability of a nucleus produced in a fragmentation reaction being populated in an isomeric state I_m is given by:

$$\rho_{theo} = \int_{I_m}^{\infty} \sigma(I)\,\mathrm{d}I = exp\left[-\frac{I_m\left(I_m+1\right)}{2\sigma_f^2}\right] \quad (1.18)$$

where σ_f^2 is the spin cut-off parameter, given by Eq: 1.11, where the quadrupole deformation parameters β have been obtained from [37]. Fig. 1.3 shows how the theoretical isomeric ratio varies with spin for two different mass fragments changing the parameter ν from 2 to 3.

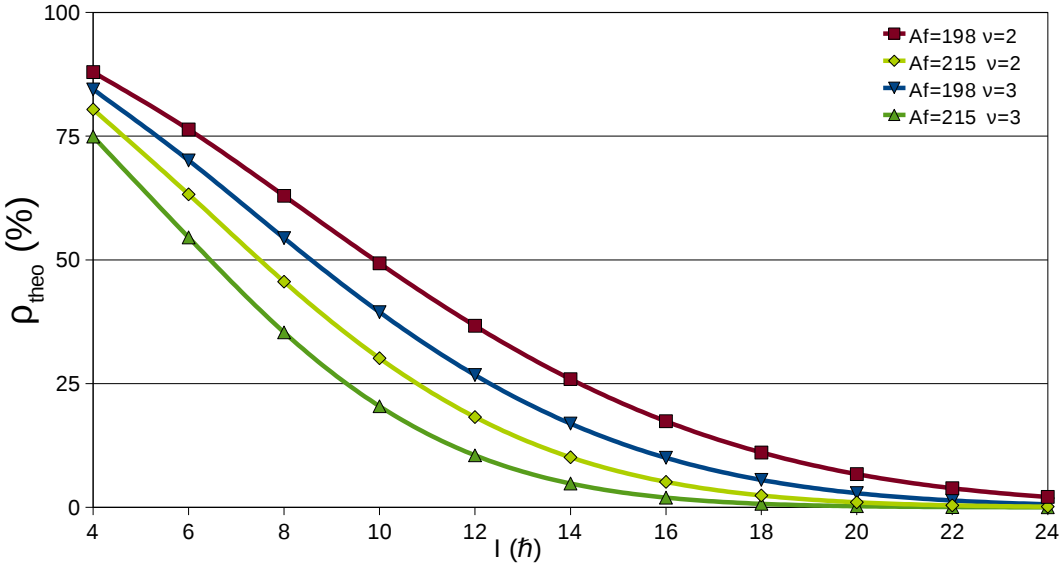

Figure 1.3: *Theoretical isomeric ratios as function of spin for fragment masses of 198 and 215 for ν equal 2 and 3, calculated using Eq. 1.18.*

Ion	I^{π}	R_{exp}[%]	$\rho_{theo}^{ABRABLA}$[%]	$\rho_{theo}^{ART+SBD}$[%]
^{211}Fr	$29/2^{+}$	5.7(19)	9.4	10.03
^{212}Fr	15^{-}	7.5(18)	8.5	9.15
^{213}Fr	$29/2^{+}$	12(8)	11.1	10.82
^{214}Ra	17^{-}	6.8(23)	2.4	3.20
^{215}Ra	$43/2^{-}$	3.1(6)	0.21	0.82
^{215}Ac	$(29/2^{+})$	4.8(12)	3.8	-

Table 1.1: *Experimental isomeric ratios from [7] and theoretical values calculated using ABRABLA [7] and ART+SBD [35].*

Experimentally there are nuclear decays that bypass the isomeric state of a given nucleus, therefore the ratio between the experimental and theoretical isomeric ratios is expected to be equal to or less than one. Recent work [7, 8] has reported that the experimental data for spins greater than $17\hbar$ contradicts the abrasion-ablasion model, with measured isomeric ratios larger than the calculated ones. Fig. 1.4 shows the experimental isomeric ratios compared with the predictions from the ABRABLA and ART+SBD models, and the calculations are shown in Table 1.1. This discrepancy between theory and experiment at high spins was thought to be due to a collective component of angular momentum in the prefragment which is expected to increase with spin [7]. More recently [35], better agreement with the data has been obtained by considering the abrasion stage in the framework of a relativistic transport model and the ablation stage as a sequential binary decay, as it can be seen from the red points in Fig. 1.4. The isomeric ratios obtained in

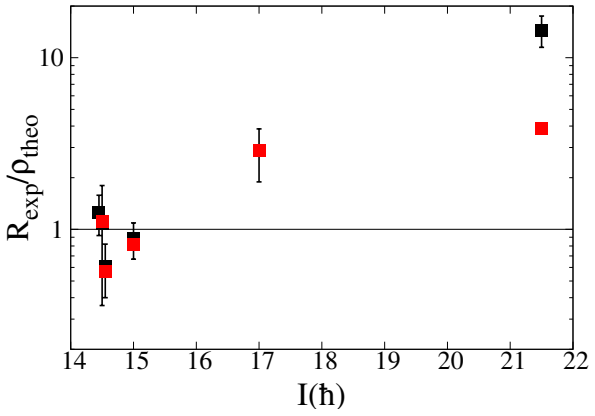

Figure 1.4: *Ratios between experimental and calculated isomeric ratios. The black points represent the experimental values compared with ABRABLA [7] and the red points are compared with ART+SBD [35].*

this thesis, and presented in Chapter 4, will be compared with the results of applying the abrasion-ablation model, extending the amount of available data for high-spin states.

Chapter 2

Experimental procedure

The population of high-spin states produced in the projectile fragmentation of a ^{238}U (1 GeV/A) beam on a ^{9}Be target has been studied. In order to study the angular momentum population of the reaction products, precise isotopic identification and gamma-ray spectroscopy are needed. The complexity of these measurements requires specific experimental circumstances which are discussed in detail in the following sections. All these challenging requirements are fulfilled at the Gesellschaft für Schewerionenforschung GSI facility in Darmstadt, Germany, where the data forming the basis of this thesis has been collected as part of the stopped beam campaign within the Rare ISotopes INvestigations collaboration (RISING) [38]. The GSI facility, shown in Fig. 2.1, consists mainly of the UNILAC linear accelerator combined with the SIS18 heavy-ion synchrotron as the accelerator system, and the FRagment Separator which separates and identifies the reaction products. In the following sections, a brief introduction to the primary beam production and acceleration, and reaction products separation and identification is presented.

2.1 The accelerator system

The accelerator system at GSI consists of three parts, the ion source, the UNILAC linear accelerator [40] and the SIS18 heavy ion synchrotron [41], as shown in Fig. 2.2. The atoms from either the MUCIS/MEVVA (MUltiCusp Ion Source/MEtal Vapour Vacuum Arc) or PIG (Penning Ionisation Gauge) ion sources are ionised by means of a high current gas discharge, extracted, pre-accelerated and injected into the UNILAC. The beam extracted from the ion source generally comprises different isotopes in different ionisation states, and therefore Low Energy Beam Transport (LEBT) devices are employed to separate the ions of interest and focus them with the correct acceptance into the accelerator.

Figure 2.1: *An overview of the GSI facility [39]. The UNILAC linear accelerator is followed by the SIS18 synchrotron where the heavy ion beams are accelerated to energies of 1 GeV/A prior to being injected into the FRagment Separator.*

Figure 2.2: *A detailed schematic of the ion sources feeding the UNILAC universal accelerator, which acts as a pre-accelerator for the SIS18 synchrotron [40].*

The ions are injected into the first part of the linear accelerator, the high current injector (HSI), consisting of a 36 MHz Radio Frequency Quadrupole (RFQ) structure followed by an inter-digital H-mode Wideröe structure. Fig. 2.3 shows the RFQ structure, formed by a quadrupole tube with an RF voltage applied to its electrodes accelerating the ions from 2.2 to 120 keV/A. Further acceleration is achieved in the H-mode structure, where alternate cylindrical electrodes (drift tubes) are connected to opposite terminals of the RF voltage. Longer drift tubes containing triplets of quadrupoles are alternated for focusing purposes. When the RF voltages are maximum on each electrode, the beam is accelerated in every other gap, exiting the electrodes when the field in the next gap changes polarity. Energies of up to 1.4 MeV/A are achieved at this point for $^{238}U^{10+}$. Following pre-acceleration in the HSI, the beam passes through a gas stripper in order to increase the charge state and facilitate further acceleration in the last part of the UNILAC. This is a 108 MHz Álvarez structure, consisting of four tanks and 150 drift tubes with the electromagnetic field in phase for consecutive electrodes, accelerating the beam in each gap up to an energy of 13.5 MeV/A for $^{238}U^{28+}$. At the end of the UNILAC, fifteen resonators adjust the ion speed, accelerating or decelerating the ions to final energies between 2 to 18 MeV/A.

Figure 2.3: *The Radio Frequency Quadrupole structure locate at the entrance of the linear accelerator [40].*

In the entrance of the SIS18 synchrotron [42] a thin carbon foil increases the charge state of the ^{238}U beam to 73^+. Fig. 2.4 shows a schematic of the SIS18, which consists of 12 identical sections evenly placed along its 216 metre long perimeter. Each section comprises two dipoles to deflect the beam, a quadrupole triplet to focus and a set of sextupoles to correct chromatic aberrations in the beam. As shown in blue in Fig. 2.4, two radio frequency cavities are placed opposite each other in the ring, in order to accelerate the beam each revolution by means of a maximum 16 kV voltage. The SIS18 operates in high-vacuum in order to avoid the beam stripping and capturing electrons through collisions with the gas. The maximum energy achievable in the synchrotron is 1 GeV/A for $^{238}U^{73+}$, due to its 18 Tm magnetic rigidity; and this energy beam has been used for the experiments presented in this work.

After acceleration, the beam is guided to the FRagment Separator (FRS) through an extraction beam line. The maximum intensity achieved in the SIS18 is $\sim 10^9$ particles per second for a uranium beam. In the experiments presented here, the intensity of

Figure 2.4: *A schematic of the SIS18 synchrotron [41]. Note in blue the two RF cavities which accelerate the beam.*

the 1 GeV/A ^{238}U beam was reduced to 10^6 particles per 10 seconds spill length due to technical problems with the accelerator. The projectile fragmentation reaction takes place when the beam impinges onto a 2.5 mg/cm^2 ^{9}Be production target placed at the entrance of the FRS. The target thickness was chosen using the LISE++ code [36], as a compromise between the number of secondary nuclear reactions and the secondary beam intensity.

2.2 The FRagment Separator (FRS) and charge states separation

The projectile fragmentation reaction products enter the FRS [44], where they are selected and separated in terms of their mass-to-charge ratio (A/Q). As shown in Fig. 2.5, the FRS is a four stage achromatic magnetic separator. Each stage consists of a dipole, a set of quadrupoles grouped in a triplet and a doublet, and two sextupoles. The quadrupoles define the horizontal and vertical emittance of the beam and focus the beam along the FRS. The sextupoles placed before and after the dipoles allow the beam optics to be corrected for chromatic aberrations. The FRS is suitable for heavy-ion beams with magnetic

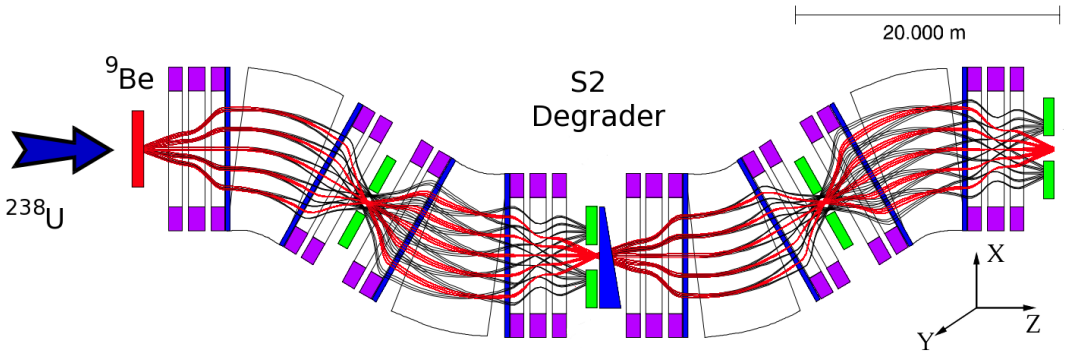

Figure 2.5: *A schematic of the FRS FRagment Separator comprising of four dipoles (white), quadrupole triplets and doublets (purple) and sextupoles (blue) placed before and after the dipoles. Note the S2 degrader in the middle of the separator. Adapted from [43].*

rigidities between 5 and 18 Tm, determined by the maximum magnetic field of 1.6 T and the 11.25 m curvature radius of the dipoles.

Charged particles in an electromagnetic field experience a force governed by the Lorentz force law [45]:

$$\vec{F} = Q\left(\vec{E} + \vec{v} \times \vec{B}\right), \tag{2.1}$$

where Q is the ionic charge in units of the electric charge (1.602×10^{-19} Coulombs), $\vec{v}$ is the ion's velocity and $\vec{E}$ and $\vec{B}$ are the electric and magnetic fields respectively. The velocity of the ions is perpendicular to the magnetic fields of the dipoles and as such, their trajectory is described by a circular orbit, experiencing a force which depends on the ions mass and velocity, and radius of curvature of the dipoles (ρ):

$$\frac{mv^2}{\rho} = QvB \tag{2.2}$$

At relativistic energies the mass of the ion is $m = \gamma m_0 = \gamma Au$, where A is the atomic mass, u is the atomic mass unit (931 MeV/c^2) and γ is the relativistic factor defined as:

$$\gamma = \sqrt{\frac{1}{1-\beta^2}} \quad \text{with} \quad \beta = \frac{v}{c}, \tag{2.3}$$

where c is the speed of light. The ions passing through the fragment separator follow different trajectories depending on their momentum (velocity) and given by the magnetic rigidity of the dipoles. Therefore, the reaction products can be separated in terms of their A/Q ratio:

$$\frac{A}{Q} = \frac{B\rho}{\beta\gamma uc} \tag{2.4}$$

By measuring the momentum of the ions and knowing the magnetic rigidity used to select the nuclei of interest ($B\rho$), the fragments are separated at the end of the FRS in terms of their A/Q ratio. Measuring Q, A can be obtained and the nuclei can be identified in terms of their mass and charge.

According to the Bethe-Bloch equation [46], the energy loss of ions passing through matter does not depend on the square of the nuclear charge Z^2, but rather on the square of the ionic charge Q^2, therefore good charge state separation is fundamental for the correct identification of the nuclei of interest [47]. The variation of the ionic charge depends on two processes: electron stripping and electron capture. For the relativistic energies involved in this experiment the probability of electron stripping is higher than for electron capture, implying that any captured electron will be easily stripped off by a layer of stripper foil. At lower energies, the probability of an ion picking up electrons increases. This aspect becomes important during the fragment separation process, when the ions are slowed to approximately half the incident energy of the primary beam. Fig. 2.6 shows the charge state distributions for different uranium beam energies in a carbon foil, illustrating how at lower energies the distribution does not contain only bare ions as opposed to the highest energy case, where the distribution is narrower and mainly composed of bare ions. Foils made of Nb material are good electron strippers, thus stripper foils are inserted after the production target, degrader and between the two ionization chambers placed after the FRS, where the reactions products pass through a sufficient amount of matter and are likely to pick up electrons. The Nb foil thickness was chosen as a compromise between its efficiency to strip off electrons and their influence on the beam optics.

Figure 2.6: *Charge state distributions of ^{238}U projectiles impinging onto a carbon foil [47].*

In the intermediate stage of the FRS (S2), all the fragments with the same A/Q ratio are focused on the same point in the horizontal plane. Introducing a wedge of material, the so-called degrader, the ions lose energy according to the square of their ionic charge, following different trajectories depending on their energy loss.

The degrader at S2 is shown in Fig. 2.7. By changing the variable thickness of the Aluminium wedges, selecting a plate from the ladder and putting the discs at a particular

angle, the beam optic properties can be altered in the second stage of the FRS. In this experiment the degrader was arranged for the FRS to operate in achromatic mode, achieving a good horizontal separation of the fragments at the final focal plane. In other experiments such as in α and β decay studies, where the ions need to be implanted at different depths, the monochromatic mode is used.

Figure 2.7: *A schematic of the degrader at S2 [48].*

The energy loss in the degrader is determined from the change in the Lorentz factor γ between the first and second stages of the FRS. The kinetic energy of ions travelling at relativistic energies can be expressed as:

$$T = mc^2 - m_0c^2 = (\gamma - 1)\, m_0c^2 = (\gamma - 1)\, Auc^2 \tag{2.5}$$

Therefore the energy loss through the degrader is:

$$\Delta T = \Delta\gamma Auc^2 \tag{2.6}$$

From Eqs: 2.4 and 2.6, the Lorentz factor can be calculated in both stages of the FRS, and the energy loss in the degrader is calculated as follows:

$$\Delta E_{deg} = uc^2 A \left[\sqrt{1 + \left(\frac{\left(1 - \frac{S2_{pos} - M_2 S^{TA}_{pos}}{D_2}\right)\left(\frac{B_1+B_2}{2}\right)\left(\frac{\rho_1+\rho_2}{2}\right)}{\frac{A}{Q}uc} \right)^2} - \sqrt{\frac{1}{1-\beta^2}} \right] \tag{2.7}$$

where $S2_{pos}$ and S^{TA1}_{pos} are the positions at S2 and S1 respectively, $B_1(B_2)$ and $\rho_1(\rho_2)$ are the magnetic fields and radius of curvature of first (second) half of the FRS.

[1] S^{TA}_{pos} is the position at the production target, where the beam is considered to be centred and therefore $S1^{TA}_{pos}$=1.

The ions lose energy in the degrader depending on their charge state, therefore ions stripping or picking up electrons at S2 can be easily identified. This method provides information on the change in the charge of the ions, but not the actual nuclear charge, therefore the energy loss in the degrader method is combined with the information from two ionisation chambers placed after the FRS. By selecting fragments that do not change their charge in the degrader, the A/Q ratio at the exit of the FRS is determined with the certainty that only fully stripped ions are being considered.

At the end of the FRS the ions are separated and identified combining the information from the magnetic fields applied to the dipoles and from a set of detectors placed along and at the end of the FRS. Fig. 2.8 shows the set-up used during the experiment. In the next sections the nuclei identification techniques and detectors used for that purpose, will be explained in detail.

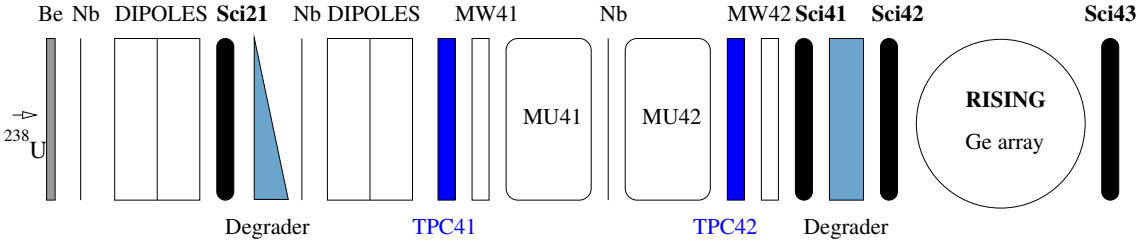

Figure 2.8: *A schematic of the FRagment Separator and the set-up at the final focal plane during the S347 experiment.*

2.3 Isotopic identification

The fragments are separated in terms of their A/Q ratio, given by Eq. 2.4, which can be split into three parts:

- $B\rho$: the magnetic rigidity across the second half of the FRS is determined from the magnetic field applied to the dipoles and their radius of curvature:

$$B\rho = \left(\frac{B_3 + B_4}{2}\right)\left(\frac{\rho_3 + \rho_4}{2}\right)\left(1 - \frac{S4_{pos} - M_4 S2_{pos}}{D_4}\right) \tag{2.8}$$

  where $S4_{pos}$ and $S2_{pos}$ are the horizontal positions at the final and intermediate focal planes, D_4 is the dispersion and M_4 the magnification of the beam between the S2 and S4:

$$M_4 = \frac{D_4}{D_2} \tag{2.9}$$

- $\beta\gamma$: the velocities of the fragments can be determined from the time-of-flight through the second half of the FRS, measured by means of two scintillators. Sci21 and Sc41, as shown in Fig. 2.8.

- *uc*: is a constant value approximately equal to 3.11 MeV/c.

The magnetic rigidities are selected depending on which region of the nuclear chart is studied and the determination of the velocity of the ions from the time-of-flight is explained in the following section.

2.3.1 Time-of-flight (TOF) determination

The velocity of the ions is determined from the TOF between two scintillation detectors, Sci21 and Sci41, as shown in Fig. 2.8.

Scintillation detectors [49] are based on the light produced by ionizing radiation in certain materials. The incident ions excite the atoms and molecules in the material, which subse-

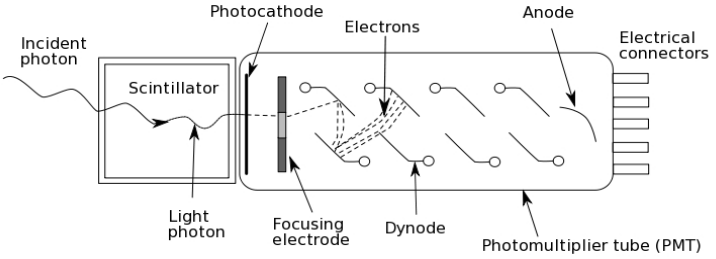

Figure 2.9: *A schematic of a scintillation detector coupled to a photomultiplier tube.*

quently de-excite producing light. The photons emitted by the scintillation material are then collected and converted into an electric current by means of a PhotoMultiplier Tube (PMT). As shown in Fig. 2.9, a PMT consists mainly of three parts: a photo-cathode, an electron multiplier section and an anode. Photons are absorbed in the photo-cathode by the photoelectric effect and release electrons. The electrons are accelerated by means of the applied voltage, and focused towards the electron multiplier section, consisting of a series of electrodes called dynodes. The geometry of the dynodes is designed to produce a cascade of new electrons in each stage, which are collected in the anode, producing the desired electric pulse.

The scintillators used during the experiment were made of BC420 plastic material [50], which is especially suitable for timing applications due to its short decay time and high efficiency for light production. One PMT is coupled at each side of each scintillation

detector. The scintillators have a thickness of 5 mm and an active area of 200×80 mm, which has been proven to be a good compromise to preserve the optical properties of the spectrometer [50]. The time resolution of these detectors is about 10.6 ps for a ^{238}U beam, which corresponds to a spatial resolution of about 1.6 mm. As shown in Fig. 2.10, the output signals from the two PMTs are fed into the START and STOP inputs of time-to-amplitude converters (TAC), for which the magnitude of their outputs is related to the position in the x direction.The two PMTs attached to each scintillator provide two TOF values from the time difference between left-left and right-right.

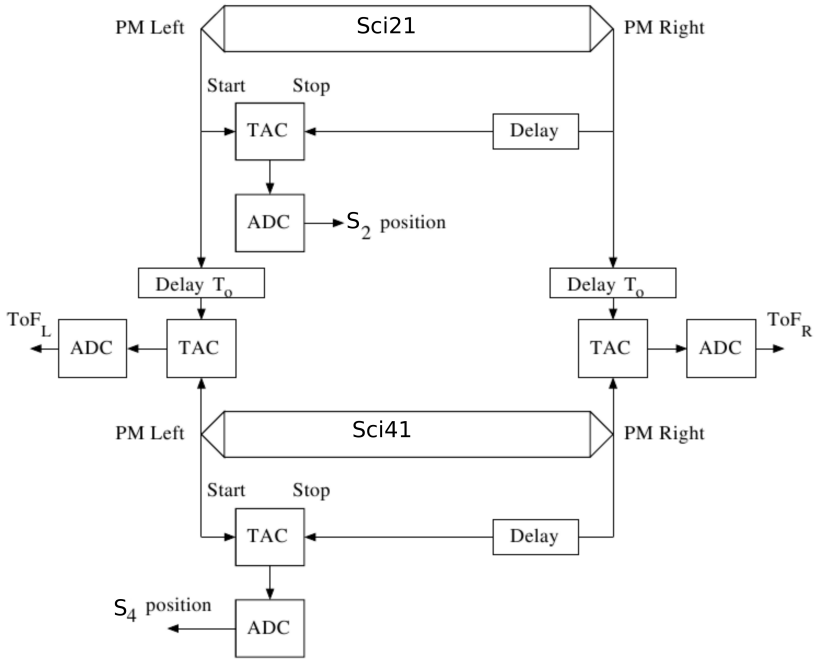

Figure 2.10: *A schematic of the set-up for the TOF measurement.*

The different length cables for both scintillators introduce an effective delay time T_d between the time signals in Sci21 (T1) and Sci41 (T2), such that $T_2 + T_d > T_4$. Therefore the real TOF is:

$$TOF = T_d - TOF^* = \frac{l}{v}, \tag{2.10}$$

where TOF* is the measured time of flight, l is the distance between the scintillators and v is the velocity of the ions.

TOF measurements are also affected by the ion interaction point along the horizontal position of the scintillator itself, since the time collection can be different depending on the distance from the interaction point to the PMT. This effect can be corrected using the horizontal positions at S2 and S4 calculated from the positions in Sci21 and

Sci41 respectively, and taking into account the refractive index of the scintillator material (n=1.58 for BC420 [51]):

$$TOF_{corr} = TOF + \left(t_2^{coll} - t_4^{coll}\right) = TOF + \frac{n}{c}\left(S2_{pos} - S4_{pos}\right) \tag{2.11}$$

- Calibrations -

To calibrate the scintillators, multiwire detectors are placed behind the scintillators [2], and then are illuminated simultaneously with a defocused primary beam. The calibration coefficients are determined by fitting the dependence of the tracked calibrated position in the multiwires with the time difference in the scintillators to a second order polynomial, as shown in Fig. 2.11.

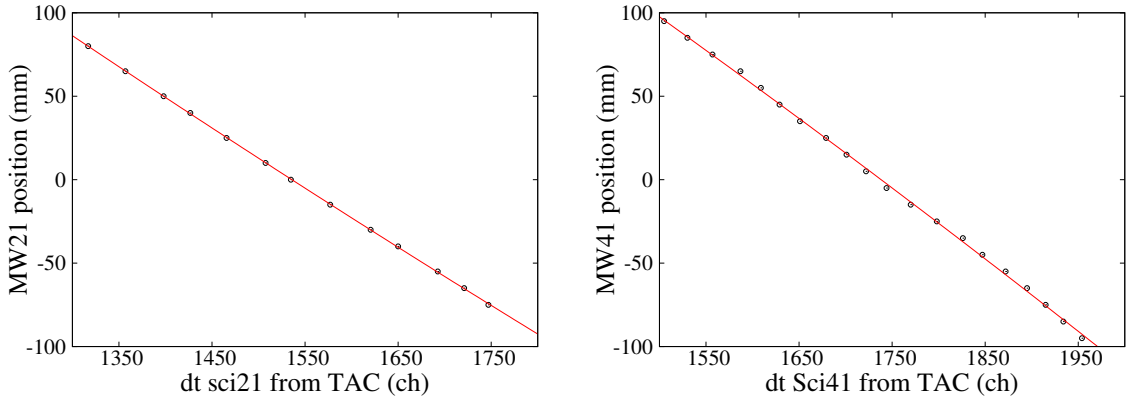

Figure 2.11: *Position calibration of scintillators Sci21 and Sci41 using MW41 and MW42 respectively.*

For the TOF calibration, three primary beam energies were used, corresponding to specific relativistic velocity parameters β:

$$E_{beam} = m_0c^2\left(\gamma - 1\right) \tag{2.12}$$

$$\beta = \sqrt{1 - \left(\frac{m_0c^2}{E_{beam} + m_0c^2}\right)} \tag{2.13}$$

Fig. 2.12 shows the measured time-of-flight TOF* plotted as a function of $1/\beta$ and fitted to a linear equation as follows:

$$TOF_{corr} = T_d - TOF^* \tag{2.14}$$

$$TOF^* = a + \frac{b}{\beta}, \tag{2.15}$$

where $|b|$ times the speed of light represents the average flight length (l) and a is the delay time applied to Sci21.

[2] The multiwire detectors calibration is explained in Section 2.4.1.1.

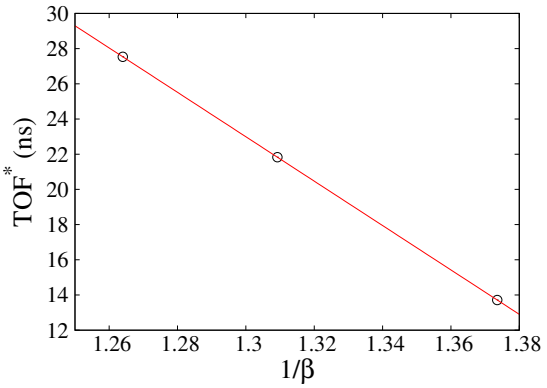

Figure 2.12: *Time-of-flight calibration.*

E (MeV/u)	β	TOF* (ns)	TOF$_{corr}$ (ns)
427.508	0.7283	13.713	173.269
511.837	0.7638	21.828	165.154
591.461	0.7911	27.535	159.447

Table 2.1: *Primary beam energies used for the TOF calibration and results.*

An average in-flight path length of 37.8186(12) m and a delay time T_d of 186.982(5) ns are obtained. The inputs and results of the calibration are shown in Table 2.1.

2.4 Charge determination

The nuclear charge of the ions is determined from the energy lost by the particles passing through the gas of an ionization chamber. Ionisation gas detectors [49] are based on the effects of a charged particle passing through a gas. When an ion passes through a gas-filled detector, the atoms are ionised, creating a track of free electrons and positive ions, called ion pairs. In the presence of an electric field , the charges move with a drift velocity which depends on the electric field applied, the gas pressure and the mobility. The positive ions drift in the direction of the electric field, while the free electrons move in the opposite direction. At high applied voltage, not exceeding 10 kV, the electric field is enough to neglect recombination of the charges, and all the ion pairs created contribute to the ion current.

It is important to distinguish between the energy loss of the incident particle and the energy deposited in the detector, since only the latter is measurable. Therefore the pulse-height resolution is an important factor in these type of detectors. The position dependence on the pulse amplitude is minimised using a grided ion chamber, where the active volume is divided into two parts by a Frisch grid. Two MUlti-Sampling-Ionization-Chamber (MUSIC) detectors [52] were used during the experiment to determine the nuclear charge of the ions. The two chambers were placed after the FRS, with a Nb stripper foil in between, as shown in Fig. 2.8. The MUSIC detector is an eight anode ionization chamber filled with tetrafluoromethane gas (CF_4) at room temperature and atmospheric pressure, as shown in Fig. 2.13.

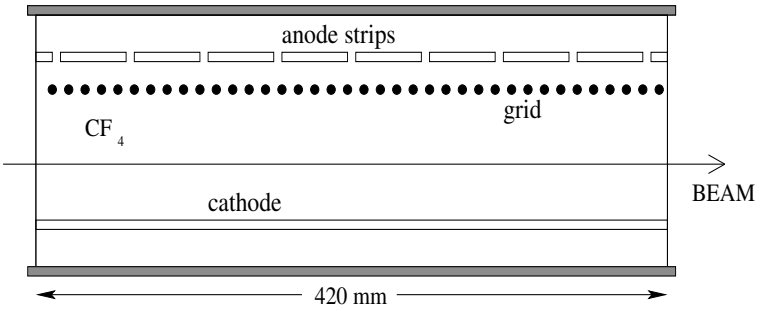

Figure 2.13: *A schematic of the MUlti-Sampling-Ionization Chamber (MUSIC) adapted from [53].*

The energy loss in the MUSIC detector is calculated combining pair-wise products of signals from the eight anodes. Three corrections must be applied to determine an accurate nuclear charge:

- Position dependence $f(x)$: the signals from each anode differ from each other due to recombination effects of the ions in the gas, so that the MUSIC detectors response is position dependent.
- Velocity dependence $g(v)$: ions with different velocities deposit energy at different rates. A calibration for several beam energies is performed to calibrate the response of the MUSIC detector to different energies, i.e. velocities.
- Pressure dependence P(t): The gas in the MUSIC detectors is kept at ambient conditions, therefore variations in the atmospheric pressure and temperature can change the detector response.

Thus the energy loss can be expressed as:

$$\Delta E = f\left(Z, v, x, P\right) \simeq Z^2 \frac{f\left(x\right)\ P\left(t\right)}{g\left(v\right)} \tag{2.16}$$

In order to perform these corrections, the ions need to be tracked along their trajectories through the MUSIC detectors. This is done using multiwire and time-projection chamber detectors, which are described in detail in the following sections. Also the calibrations necessary to obtain $f(x)$, $g(v)$ and $P(t)$ will be described.

2.4.1 Ion tracking

The position of the ions is tracked using either two multiwire detectors, MW41 and MW42; or two time-projection chambers, TPC41 and TPC42, as shown in Fig. 2.8.

2.4.1.1 Multiwire

A set of MultiWire Proportional Chambers (MWPC) [54] was installed along the beam line. One detector was placed in the intermediate focal plane only for the calibration of scintillator Sci21, and removed during the experiment due to the inhomogeneities introduced in the beam optics. The other two detectors, MW41 and MW42 were kept in the beam line during the experiment, as shown in Fig. 2.8.

As shown in Fig. 2.14, each chamber consists of five parallel wire planes, filled with a gas mixture of argon, CO_2 and alcohol. The wire directions on cathodes X and Y are orthogonal and the anode plane is placed diagonally to the cathodes. A second structure, the pre-gap, consists of two meshes, T and G. For the heavy ions studied in this experiment, the voltage from the anode is high enough to amplify a sufficient number of electrons and there is no need for pre-amplification. The ionised free electrons produced in the gas migrate to the nearest anode, and a signal is induced in the X and Y cathodes. The readout is done by connecting a delay line to each end of the wires of each cathode. The signal propagates through both sides of the line and is amplified and fed into the STOP of a time-digital-converter (TDC), where the START input is given by the anode signal. This produces four amplified signals, x_L, x_R, y_U and y_D.

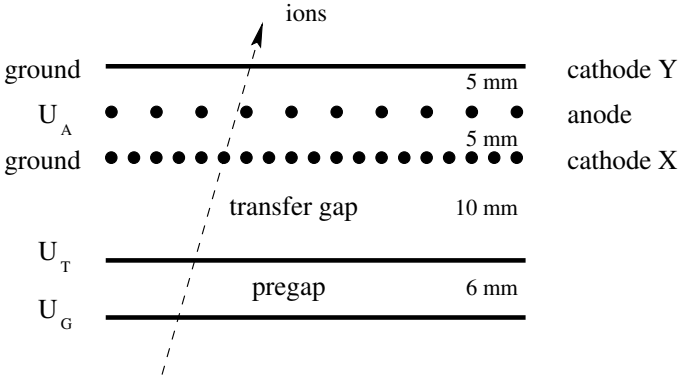

Figure 2.14: *A schematic of a MultiWire Proportional Counter (MWPC) adapted from [55].*

These delayed signals, together with the anode signal, allow the unambiguous determination of the position of the ions passing through the detector. The x (y) position is given by the time difference between left (down) and right (up), as follows

$$mw_x = x_R - x_L \tag{2.17}$$

$$mw_y = y_D - y_U \tag{2.18}$$

The calibration coefficients to convert time into distance units depend on the length of the delay lines used, and the offset calibration is obtained by aligning the primary beam

with the current grid and taking the mean value of the resulting spectrum. For heavy ions the MWPC detector offers a spatial resolution of about 1 mm [54] and it covers a range from -100 mm (left, up) to 100 mm (right, down).

2.4.1.2 Time Projection Chamber (TPC)

Two TPC detectors (TPC41 and TPC42) were used during the experiment, placed in front of MW41 and MW42 respectively as shown in Fig. 2.8. They were used for tracking the ions and achieved a resolution better than 0.5 mm [56].

Fig. 2.15 shows a schematic of the TPC used during the experiment, consisting of four anodes and one cathode, and filled with P10 gas (90% Ar, 10% CH_4) at atmospheric pressure, with an active volume of 240×65×40 mm^3. The anodes are connected by a 240 mm long delay line and their signals are amplified and separated into two outputs, energy and time. The signals given by the delay line allow an unambiguous determination

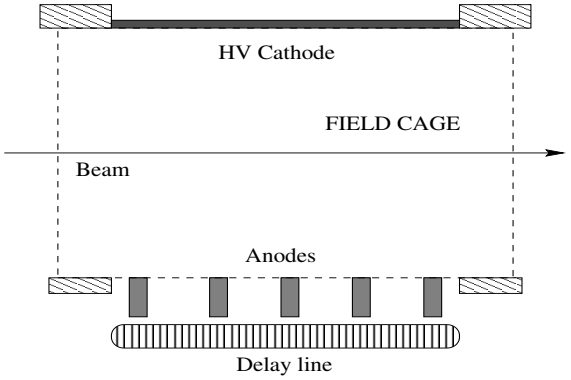

Figure 2.15: *Schematic of a Time-Projection Chamber or TPC.*

of the x and y positions. The y position is determined from the electron drift times from the anodes. This position has not been used during the analysis, so no further details are provided. The x position is calculated as the time difference between the arrival of the signals to the right and left ends of the delay line:

$$tpc_x = tpc_R - tpc_L \tag{2.19}$$

The propagation time along the delay line is constant and given by:

$$(tpc_R + tpc_L) - 2tpd_d = tpc_b, \tag{2.20}$$

where tpc_R and tpc_L are the time signals from the right and left ends of the delay line respectively, tpc_d is the electron drift time, given by the anode, and tpc_b is the time

associated to the length of the delay line. This condition can be used to reject events in which the position is not within three times the r.m.s. of the tpc_b distribution. The position is accepted if at least two of the four measurements, each corresponding to the four tpc_d times from the four anodes, fulfil this condition.

2.4.1.3 Calibrations: obtaining $f(x)$, $g(v)$ and P(T).

The position dependence calibration factor $f(x)$ is obtained by illuminating the MUSIC detectors with a defocused ^{238}U beam and evaluating the relation between the energy loss and the position across the detector. This position of the ions along the MUSIC detectors is obtained from the interpolated position between MW41 and MW42 (the same applies for the TPC detectors). Fig. 2.16 shows the energy loss dependence on the distance from the anode to the interaction point of the ions due to recombination effects expressed as a polynomial of fifth order:

$$\Delta E^{pos}_{corr} = a + b \times S4_{pos} + c \times S4^2_{pos} + d \times S4^3_{pos} + e \times S4^4_{pos} + f \times S4^5_{pos}, \qquad (2.21)$$

where the coefficient a is the maximum energy loss, corresponding with the ions passing through the centre of detector, so the position correction to be used in Eq. 2.16 is:

$$f(x) = \frac{a}{\Delta E^{corr}_{pos}} \qquad (2.22)$$

Fig. 2.17 shows the calibration of the MUSIC detector response to the velocity of the

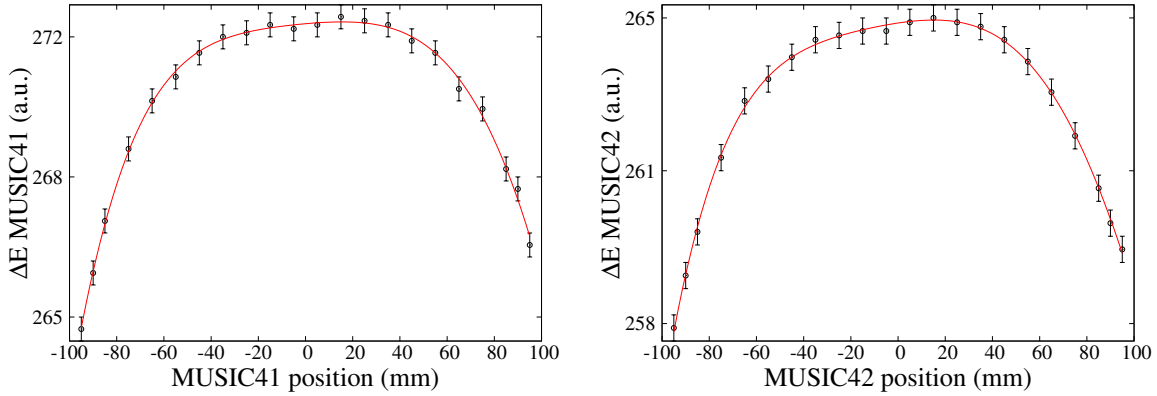

Figure 2.16: *The energy loss in the MUSIC detectors as a function of the x position for a defocused beam.*

ions. The velocity correction $g(v)$ was obtained by fitting the energy loss as a function of the velocity parameter β for three different monoenergetic beams:

$$\Delta E^{vel}_{corr} = a + b \times \beta + c \times \beta^2, \qquad (2.23)$$

so the velocity correction to be used in Eq: 2.16 is:

$$g\left(v\right) = \frac{1}{\Delta E_{corr}^{vel}} \tag{2.24}$$

Another factor affecting the measurements is the pressure of the gas within the cham-

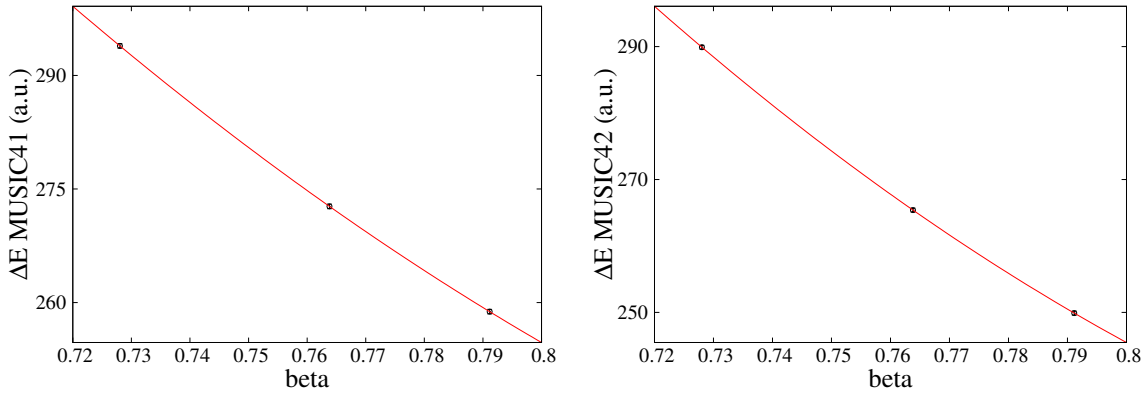

Figure 2.17: *The energy loss in the MUSIC detectors as a function of the velocity of the ions.*

ber, which is kept at atmospheric pressure, and as such varies with time as the ambient conditions change. Therefore, for the first time, an automatic system was installed in the MUSIC detectors to allow the data to be corrected for varying pressures on an event-by-event basis:

$$\Delta E_{corr}^{P} = \Delta E_{raw} \times \frac{P_{ref}}{P_{cal}}, \tag{2.25}$$

where P_{ref} is the reference pressure measured at the beginning of the experiment and P_{cal} is the calibrated pressure obtained from of the raw signal from the MUSIC detectors:

$$P_{cal} = a + b\Delta P_{raw}, \tag{2.26}$$

a and b are obtained from calibrating the MUSIC detectors for several pressure values close to ambient conditions. The pressure correction factor to be used in Eq: 2.16 is:

$$P(t) = \frac{P_{ref}}{P_{cal}} \tag{2.27}$$

The pressure correction was not used in the final data analysis, since the benefits were not immediately obvious.

The charge of the ions is calculated as the product between the primary beam proton number and a correction factor to scale the energy loss according to that of the fragment. The correction factor is given by the ratio of the velocity and position correction factors,

$g(v)$ and $f(x)$ from Eqs. 2.24 and 2.22 [3]:

$$Z = \sqrt{Z_{beam}^2 \frac{g(v)}{f(x)}} \tag{2.28}$$

Fig. 2.8 shows that after the isotopic and charge identification, the ions are further slowed down in a second degrader, before they are finally brought to rest at the final focal plane, where gamma-ray spectroscopy is performed.

2.5 Gamma-ray spectroscopy

For gamma-ray spectroscopy studies there are two major categories of detectors: inorganic scintillation detectors such as NaI(Tl) and germanium semiconductor detectors. Scintillators have a better efficiency, but germanium detectors have better resolution and this makes them the preferred choice for high resolution studies in nuclear physics. In a semiconductor detector [49], electrons are excited from the valence to the conduction band due to thermal excitations and gamma-ray interactions. Because germanium semiconductors have a low energy gap (1.12 eV) between the two bands, they must be maintained at 77 K with liquid nitrogen in order to reduce thermal noise. In that way, the noise is reduced and only gamma-ray interactions will create electron-hole pairs that will contribute to the energy signal.

- RISING -

Fig. 2.18 shows the RISING array in its stopped-beam configuration [57] consisting of 15 cluster detectors from the decommissioned Euroball set-up. The array was placed in a close-packed configuration around a passive stopper at the final focal plane of the FRS. Each individual cluster comprises seven hexagonal HPGe crystals. The 105 crystals were arranged in three annular rings of five clusters each at 51°, 90° and 129° with respect to the beam line axis, with an average distance to the centre of the array of 22 cm.

Two pre-amplifier outputs from each crystal are sent to separate electronic branches, providing a digital signal for energy and time and an analogue signal for very short and long timing purposes. The digital signal is processed by a Digital-Gamma-Finder (DGF) [58], which provides a time difference between the implanted ion and the delayed gamma-ray detected by the HPGe crystal. The maximum range achieved with the DGF modules is 400 μs with a 25 ns/channel time step. The DGF modules also provide information

[3] The pressure correction factor $P(t)$ given by Eq. 2.27 can be included into the denominator if the pressure correction is used.

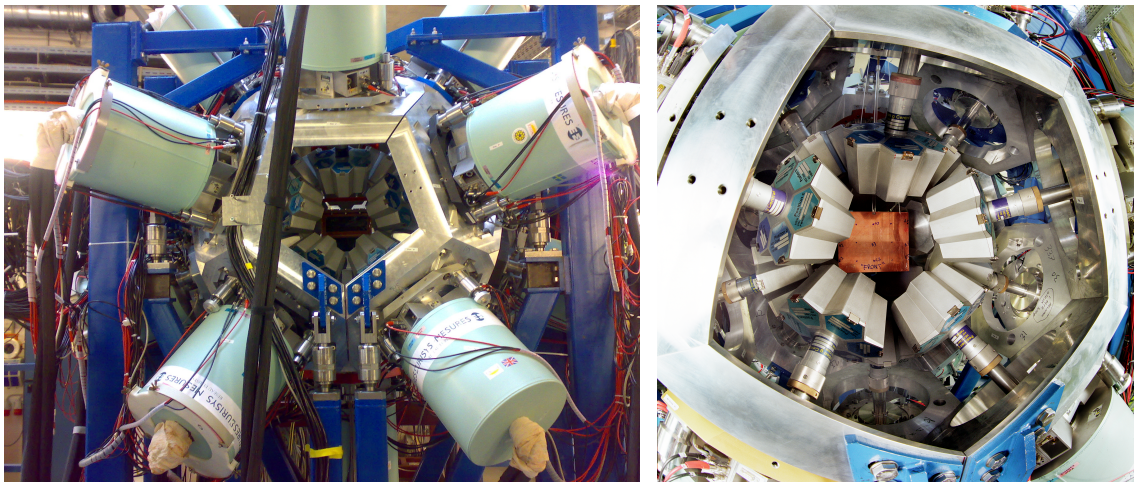

Figure 2.18: *Photographs of the RISING array in its stopped-beam configuration. The stopper is placed at the centre of the array and the beam direction is coming out of the page.*

on the energy of the gamma rays. The analogue signal from the pre-amplifiers is sent to a Timing-Filter-Amplifier followed by a Constant-Fraction-Discriminator (TFA-CFD), which produce two outputs sent to separate TDC modules, one short range (1 μs range and 0.293 ns/channel step) and one long range time (800 μs range and 0.729 ns/channel step). The implantation trigger for both branches is given by scintillator Sci41.

The absolute efficiency of the RISING array was calculated with a multi-gamma source containing ^{241}Am, ^{133}Ba, ^{137}Cs and ^{60}Co, and also a ^{152}Eu source placed at several positions around the stopper. A pulser was used to trigger the DGF acquisition instead of the Sci41 signal. Half of the data acquired during the experiment was taken using an 8 mm Perspex passive stopper in front of an active stopper box containing Double Sided Strip Silicon Detectors (DSSSD), which meant that the final focal plane was 6 cm off the centre of the array, as shown in Fig. 2.19. For this configuration, there is no efficiency calibration data, and therefore a Geant4 simulation [59, 60] was used to obtain the efficiency [61]. The other half of the data was acquired using only the centred active stopper, for which efficiency calibration data was taken. When the ions are brought to rest in the stopper, the gamma-rays emitted by the nuclei have to travel a certain distance through the stopper material, which depends on the material composition and the position and depth of implantation. Fig. 2.20

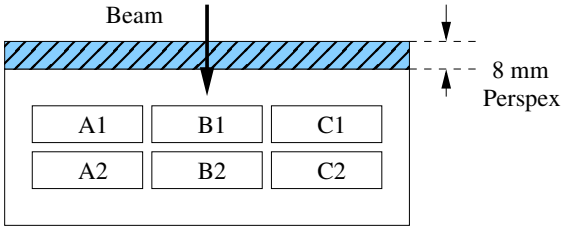

Figure 2.19: *A schematic of the 8 mm Perspex passive stopper placed in front of the active stopper box containing six silicon detectors.*

shows the absolute efficiency of the RISING array when the source is placed at six different locations, left, middle and right positions in front and behind the box corresponding to A1, B1, C1, A2, B2, C2 in Fig. 2.19 around the active stopper box. The efficiency has been obtained only for the digital time branch[4]. For energies lower than 80 keV the efficiency decreases ∼2% when the source is placed behind the box. The total absolute efficiency has been calculated as an average between the measured efficiency in both sides of the box, and corresponds to the red curves in Fig. 2.20 and 2.21, calculated as [62]:

$$E_{ff} = exp\left[\left(A + Bx + Cx^2\right)^{-G} + \left(D + Ey + Fy^2\right)^{-G}\right]^{-1/G}, \tag{2.29}$$

where:

$$x = ln\left(\frac{E(\text{keV})}{100}\right) \quad \text{and} \quad y = ln\left(\frac{E(\text{keV})}{1000}\right). \tag{2.30}$$

The blue curve in Fig. 2.21 corresponds to the simulated efficiency for the passive stopper in front of the box configuration.

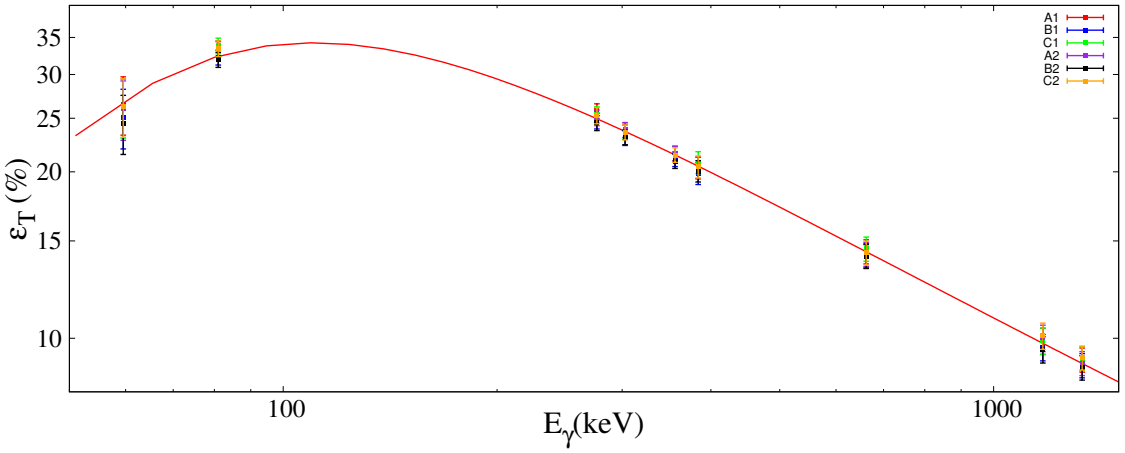

Figure 2.20: *Absolute efficiency for the RISING array at different locations around the active stopper box. The six positions, A1, B1, C1, A2, B2 and C2 correspond to the positions around the active stopper box, as indicated in Fig. 2.19.*

Due to the amount of bremsstrahlung and X-rays produced when the ions come to rest in the stopper, the efficiency is reduced by the probability of a gamma ray from the so-called prompt flash being absorbed by a crystal, and thus, "blinding" the detector for possible subsequent gamma rays happening during the same event. The corrected efficiency is

[4]The analogue timing has not been used for the data analysis due to the interest in measuring low energy transitions and the low efficiency for energies below 200 keV for the analogue time branch.

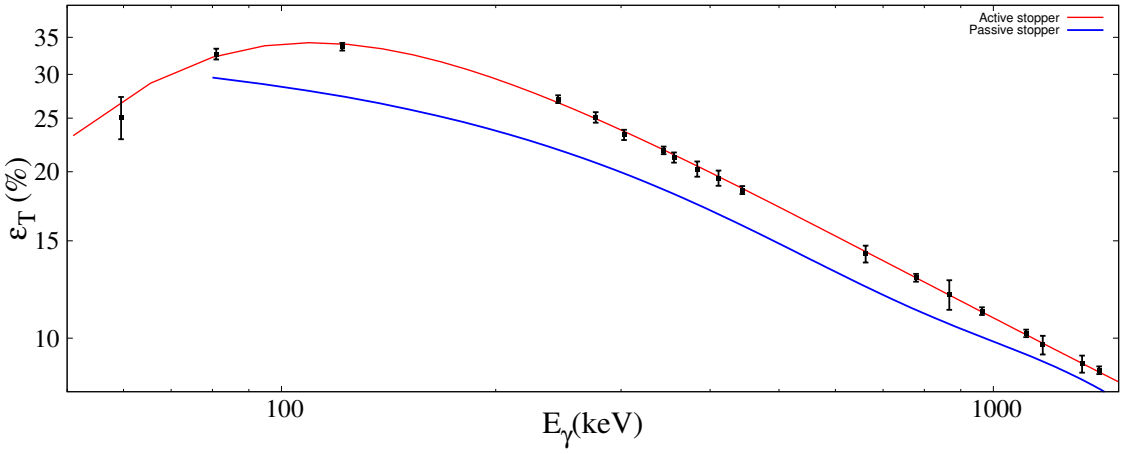

Figure 2.21: *Absolute efficiency for the RISING array for the two configurations used during the experiment. The red curve corresponds to the measured efficiency when only the active stopper box was used, and the blue one corresponds to the Geant4 simulation for the case in which the passive stopper was placed in front of the box.*

calculated as follows:

$$E_{ff}^{corr} = E_{ff}\,(1-P) = E_{ff}\left(1 - \frac{prompt\ crystal\ multiplicity}{105}\right), \tag{2.31}$$

where 105 is the total number of crystals in the array and the prompt crystal multiplicity represents the median of the distribution of crystals with energy signals below 400 keV and for which the time difference between implantation and detection is less than 250 ns in each event. The "blinding" factor P is calculated for each of the FRS sets of data, and the results are presented in Table 2.2. The efficiency of the RISING array will therefore be reduced by 22% in the ^{212}Rn, 25% in the ^{214}Th, 9.5% in the ^{213}Fr and 11% in the ^{214}Ra data sets due to the prompt flash.

The efficiency is also influenced by the number of Compton scatter events. In such case, the wrong energy is measured, the background is increased and the efficiency is reduced. An add-back routine can be used to identify and reconstruct such events, adding the energy of the scattered gamma rays together. This is discussed further in Section 3.4.

Data set	^{212}Rn	^{214}Th	^{213}Fr	^{214}Ra
P	0.2189	0.2464	0.0950	0.1126

Table 2.2: *The "blinding" factors, given the probabilities of a germanium crystal being blinded by the prompt flash for each FRS setting.*

2.6 Data AcQuisition and data format

In the experiment described in this thesis, there were six Data AcQuisition (DAQ) branches [63] in seven crates (FRS, TPC, Scalers, DGF, TDC, Silicon times and Silicon energies). The DAQ system uses the Multi-Branch-System MBS, developed at GSI and used to handle all the data coming from the different electronic branches. These branches run independently with different triggers connected by a trigger bus cable. The time matching of the events is done by the GSI time-stamp module TITRIS. The digitization of the detector signals is made using VME modules (ADC, QDC and TDC) which are readout by a VME RIO3 processor. The data is finally sent via the network to a PC, which is the event builder. The data is then ready to be stored or used for on-line data analysis purposes. Fig. 2.22 shows a diagram with the RISING and FRS DAQ branches.

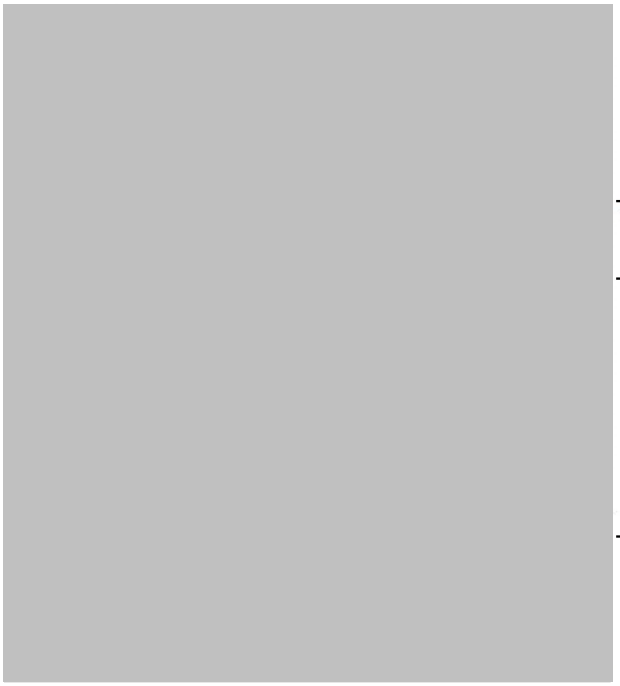

Figure 2.22: *A schematic of the Data AcQuisition system showing the DGF and FRS branches (taken from [63]).*

		Triggers				
Subevent	ID(dec/hex)	1	2	4	7	8
FRS	10/A	•	•	•	•	•
Scalers	60/3C	•	•	•	•	•
DGF	31/1F	○	•	•	○	•
Ge T	40/28	○	•	•	○	•
Si T	45/2D	○	•	•	○	○
Si E	50/32	○	•	•	○	○
TPC	60/14	○	•	○	○	○

Table 2.3: *The triggers defined during the experiment and the crates read out in each case. The subevent IDs are represented in decimal and hexadecimal format.*

The data is organised in an event-by-event mode in buffers of 16360 words. The MBS writes the data in swapped word order (byte2, byte1, byte4, byte3) format with words of length 16 bits (2 bytes) in hexadecimal format. Each event comprises seven different subevents or branches written in the following order: FRS, Scalers, DGF (energy and time), Ge timing (SR, LR), Si timing, Si energy and TPC. Table 2.3 shows the different triggers used during the experiment, and the branches which are read out for each trigger.

In this experiment, implantation events with a trigger of 2 are of interest. Every event and subevent is characterised by a header which consists of eight words, with the first two words containing information on the length of the given event or subevent. The event header contains the trigger number for that event and also an event counter, so that only events with the trigger of interest can be selected for the data analysis. The subevents can be recognised by the ID numbers included in the header, which are provided in Table 2.3. An example containing an event with an implantation trigger of 2 is represented in Fig. 2.23. The first three lines are the beginning of a buffer, and right after the first event begins (red). This events are formed by the subevents FRS (009A number of words and type 000A), scalers (0046 number of words and type 003C), DGF (0100 number of words and type 001F), Ge time including short and long range times (00A2 number of words and type 0028), Silicon times (0008 number of words and type 002D), Silicon energies (0024 number of words and type 0032) and TPC (number of words 0AE0 and type 0014).

```
0008000 3FE8 0000 000A 0001 3FE8 0100 CACD 000C
0008010 0013 0000 0000 0000 A699 480D 0328 0000
0008020 0001 0000 02CE 0000 0000 0000 0000 0000
0008030 037C 0000 000A 0001 0000 0002 5A7B 0239
0008040 009A 0000 000A 0001 000A 1300 D70C 00F7
0008050 2C5A 01F7 3289 02F7 0002 4200 44BA 4004
0008060 44E3 4005 E07F 4411 0008 4A00 482B 4810
0008070 4A49 4811 4958 4812 498D 4813 4874 4814
0008080 4AF7 4815 49C2 4816 49CE 4817 E07F 4C11
0008090 0020 6A00 4610 6800 4074 6810 4684 6801
00080A0 48A0 6811 4814 6802 4062 6812 4080 6803
00080B0 4627 6813 4072 6804 4F47 6814 403C 6805
00080C0 4614 6815 407D 6806 4086 6816 454E 6807
00080D0 4EB3 6817 49D8 6808 49F6 6818 4A23 6809
00080E0 4A3B 6819 4A22 680A 4A04 681A 4A28 680B
00080F0 49F9 681B 49F4 680C 49F2 681C 4A27 680D
0008100 4990 681D 4A3B 680E 4998 681E 4A0A 680F
0008110 49AE 681F E07F 6C11 0017 5A00 446F 5800
0008120 4256 5810 4975 5801 423C 5811 48E5 5802
0008130 424E 5812 4994 5803 4230 5813 4249 5804
0008140 4275 5814 4087 5805 4247 5815 4FE6 5806
0008150 425A 5816 427F 5817 5FFD 5808 5FFD 5809
0008160 5FFD 580A 425A 580B 4166 580C 427C 580D
0008170 496D 580E 4AC8 580F 9FFF 5C88 0046 0000
0008180 000A 0001 003C 1300 2000 6A00 8A8D 0144
0008190 60BD 00DF 281A 0000 DF17 0000 B6E8 0008
00081A0 25C6 0054 0000 0000 1124 00D4 34C0 0011
00081B0 0000 0000 24BB 0037 0000 0000 140D 0000
00081C0 140C 0000 0000 0000 44A3 000A 70E4 0367
00081D0 8956 000E 98F7 0338 0CE0 0011 F3F6 2B3F
00081E0 E858 000E 0000 0000 0000 0000 0000 0000
00081F0 CE87 0002 3734 0008 5DA9 0008 1E73 13ED
0008200 808D 0006 3355 0004 2F9C 0004 0000 6C00
0008210 0100 0000 000A 0001 001F 0901 0001 000D
0008220 0213 1103 FFE1 ECCD ECCF 0003 558B 54ED
0008230 558E 16E3 000B 056E 1103 0003 ECCD 0213
0008240 0004 FFE1 54EC ECCF 02E1 5595 0004 000F
0008250 0213 1103 FFE1 ECCD ECCF 000E 558F 54EC
0008260 558E 0470 558B 0659 000D 08CC 1103 0005
0008270 ECCD 0213 0003 FFE0 54EA ECCF 0557 558C
0008280 2916 558A 0007 000B 0213 1103 FFE1 ECCD
0008290 ECCF 0002 5590 54EB 000D 02F8 1103 0008
00082A0 ECCD 0213 0009 FFE1 54EB ECCF 1DCF 558A
00082B0 1EAB 558A 0009 000D 0213 1103 FFE1 ECCD
00082C0 ECCF 000A 558E 54EB 55A8 0006 000B 34FA
00082D0 1103 000B ECCD 0213 0004 FFDF 54E9 ECCF
00082E0 6089 5589 000C 000B 0213 1103 FFDF ECCD
00082F0 ECCF 0001 5596 54E9 000D 0321 1103 000E
0008300 ECCD 0213 0003 FFDF 54E8 ECCF 0772 5590
0008310 0C6F 558C 000F 000D 0213 1103 FFE1 ECCD
0008320 ECCF 0005 5593 54E9 558A 02FE 000B 2130
0008330 1103 0010 ECCD 0213 0001 FFE0 54E8 ECCF
0008340 0F18 5640 0013 000B 0213 1103 FFE1 ECCD
0008350 ECCF 0008 55A7 54E8 000D 3ABC 1103 0014
0008360 ECCD 0213 0003 FFE1 54DF ECCF 0537 5643
0008370 2F07 563E 0015 000B 0213 1103 FFDF ECCD
0008380 ECCF 0002 5641 54DF 000D 070B 1103 0016
0008390 ECCD 0213 0006 FFE1 54DF ECCF 19B0 558B
00083A0 02DA 5595 0017 000B 0213 1103 FFDF ECCD
00083B0 ECCF 0001 558B 54DF 000B 18B7 1103 0018
00083C0 ECCD 0213 0002 FFE1 54DE ECCF 02B9 5596
00083D0 001A 000B 0213 1103 FFE1 ECCD ECCF 0008
00083E0 558C 54DE 000B 07EB 1103 001C ECCD 0213
00083F0 0001 FFE0 54DE ECCF 0193 558F 001D 000D
0008400 0213 1103 FFE1 ECCD ECCF 000C 558E 54DE
0008410 55A7 0324 4321 397E 00A2 0000 000A 0001
0008420 0028 0900 0600 3A00 489D 3811 4837 3812
0008430 487F 3813 48BC 3814 48AF 3815 48A8 381A
0008440 8E84 3C80 0F00 5200 48A9 5000 48C2 5001
0008450 4907 5002 48E1 5012 4934 5003 4875 5004
0008460 4855 5005 484A 5006 47F0 5018 48D8 5019
0008470 491F 501A 4925 501B 4795 501C 48CB 500E
0008480 48CC 501E 8E84 5480 0400 6A00 4809 6802
0008490 4818 6812 4872 681C 48C0 681E 8E84 6C80
00084A0 0200 8200 48DC 8011 488E 800B 8E84 8480
00084B0 0047 9840 2D26 1410 2D2C 1510 2D1F 1A10
00084C0 2D39 1110 2D49 1210 2D33 1310 2D0D 2310
00084D0 2D0D 3B10 2D3C 2010 2D45 2110 2D17 2210
00084E0 2D2F 2E10 2D31 3210 2D33 3910 2D19 3A10
00084F0 2D33 3E10 2D55 2410 2D6A 2510 2D63 2610
0008500 2D83 3810 2DB2 3C10 2D20 5E10 2D34 5C10
0008510 2D5A 4210 2D5F 5210 43A9 5210 43CC 4010
0008520 43B9 4510 43B3 5110 43BA 5510 442E 4110
0008530 4431 4210 4435 4310 442C 4610 43E1 5E10
0008540 2D2A 6B10 2D15 7110 65D2 7D10 2522 7E12
0008550 25F6 7F12 0028 9820 0000 BABE A699 480D
0008560 0328 0000 0008 0000 000A 0001 002D 0901
0008570 8E03 2680 00FE A840 0000 A820 0024 0000
0008580 000A 0001 0032 0900 0100 2A00 405E 280B
0008590 8E84 2C80 0100 3A00 406E 380A 8E84 3C80
00085A0 0100 4A00 407C 481F 8E84 4C80 8E03 5E80
00085B0 0100 6A00 4060 6807 8E84 6C80 0100 7A00
00085C0 4072 7808 8E84 7C80 0000 BABE 0AE0 0000
00085D0 000A 0001 0014 1300 0008 2A00 A818 00CA
00085E0 01CA 00C6 783E 0014 ED54 0012 DE0D 0015
00085F0 AD33 0007 FB56 00D2 0001 0000 0000 2C00
0008600 0010 4200 4408 4010 43FA 4011 43FA 4012
0008610 43FF 4013 4231 4014 4338 4015 4242 4016
0008620 4346 4017 4049 4018 404C 4019 4046 401A
0008630 4047 401B 425F 401C 4440 401D 4253 401E
0008640 444B 401F D042 4409 0010 4A00 46A4 4800
0008650 46CD 4801 4701 4802 46D9 4803 494D 4804
0008660 471F 4805 4979 4806 4744 4807 4724 4808
0008670 471A 4809 4723 480A 470F 480B 49C4 480C
0008680 477B 480D 4992 480E 476C 480F D042 4C09
0008690 0000 6600 0011 8200 402B 8000 477B 8010
00086A0 47F4 8011 47DA 8012 477F 8013 4681 8014
00086B0 4707 8015 46D5 8016 475B 8017 4816 8018
00086C0 48B7 8019 4751 801A 47FD 801B 47A3 801C
00086D0 4888 801D 4717 801E 47C5 801F E080 8411
00086E0 0012 8A00 4618 8800 4640 8801 4618 8802
00086F0 46AB 8803 46E0 8804 4863 8805 475F 8806
0008700 484E 8807 463D 8808 4635 8809 45EB 880A
0008710 4627 880B 468B 880C 47E4 880D 46B1 880E
0008720 4DDE 881E 4791 880F 4622 881F E080 8C11
```

Figure 2.23: *An example of the data format structure. Grey: first buffer header. Red: first event header. Blue: subevent headers in the following order: FRS, scalers, DGF, TDC, Silicon times, Silicon energies, TPC.*

Chapter 3

Data analysis

The data forming the basis of this work was collected in two consecutive experiments. The first one was part of the RISING stopped beam campaign where two sets of data were collected, centred around ^{212}Rn and ^{214}Th. The other two sets, centred on ^{213}Fr and ^{214}Ra, were collected in a experiment from the FRS group at GSI, studying α-decay spectroscopy. Only gamma-ray information has been analysed from the latter two settings. Table 3.1 shows the relevant information for each setting.

	FRS setting			
	^{212}Rn	**^{214}Th**	**^{213}Fr**	**^{214}Ra**
Approximate acquisition time (h)	5	7	9	7
Beam intensity (pps)[1]	$2{\cdot}10^6$	$2{\cdot}10^6$	$1{\cdot}10^8$	$1{\cdot}10^8$
Perspex stopper thickness (mm)[2]	8	8	-	-
Active stopper box	IN	IN	IN	IN
S2 degrader thickness (g/cm^2)	3	3	3	3
S2 degrader angle	78.2	77.9	78.0	77.9
S4 degrader thickness (g/cm^2)	2.184	1.500	2.619	2.236
$\mathbf{B}_1$ (ρ=10.9682 m)	1.1256	1.0784	1.1169	1.1076
$\mathbf{B}_2$ (ρ=11.1669 m)	1.0864	1.0406	1.078	1.0683
$\mathbf{B}_3$ (ρ=11.3127 m)	0.8218	0.7597	0.8074	0.7943
$\mathbf{B}_4$ (ρ=11.2512 m)	0.8261	0.7636	0.8117	0.7986

Table 3.1: *Details of the FRS settings for the four data sets considered in this thesis.*

[1] pps is the acronym for particles per second.

[2] The passive stopper was used in front of the active stopper box only for the ^{212}Rn and ^{214}Th data sets.

3.1 Cleaning conditions

As explained in Chapter 2, the identification of the transmitted nuclei is based on time-of-flight measurements, particle tracking information, and energy loss measurements on an event-by-event basis. To obtain a clear identification of the transmitted nuclei, the information from all detectors needs to be correlated to ensure that all the detectors record valid data for each event. Also the transmission losses due to secondary reactions produced when the fragments are slowed down need to be discarded in order to obtain a clean identification and separation. In the following sections, these cleaning conditions will be explained in detail and data from the ^{212}Rn data set will be used for this purpose.

3.1.1 Noise in the multiwire detectors

Multiwire detectors are used to track the ions through the final part of the set-up, as shown in Fig. 2.8. The signal detected in each of the X and Y cathodes propagates through both ends of the delay line and is fed into the START and STOP of a TDC. Thus, the sum of the two signals should be a constant and equal to the length of the delay line, calculated as follows:

$$mw_x^{sum} = x_L + x_R - 2 \times anode, \tag{3.1}$$

where the anode signals are subtracted to make the sum independent of the trigger. Fig. 3.1 shows the results of applying Eq: 3.1 to the data for MW41 and MW42. Only events within the red lines, where both ends of the delay line have a good signal, are used to track ions passing through the multiwires.

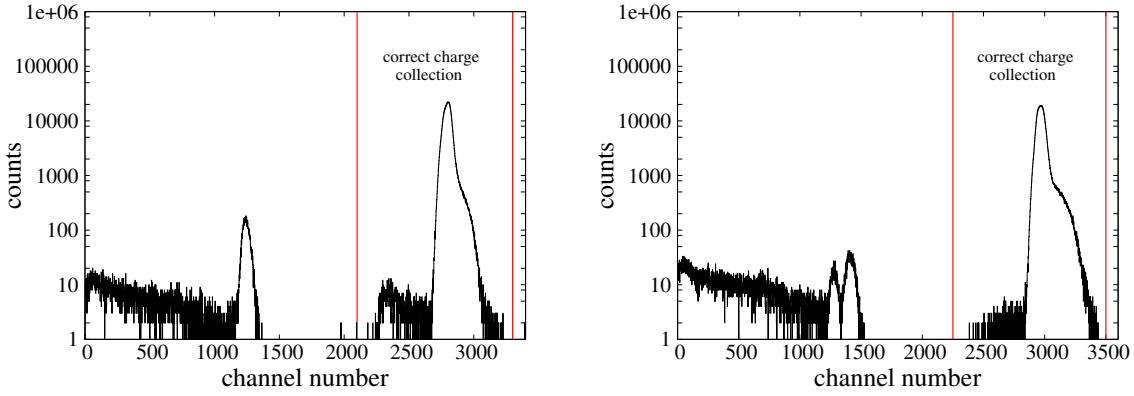

Figure 3.1: *Sum conditions calculated for MW41 (***left***) and MW42 (***right***). Events inside the red lines have a time which corresponds to the length of the delay line, and are accepted as valid events.*

3.1.2 Scintillator Sci21 light collection

As shown in Fig. 2.8, scintillator Sci21 is placed at the intermediate focal plane S2 and used together with Sci41 to calculate the TOF of the ions. Therefore, it is crucial to reject the events in which an incorrect charge collection is measured in one of the photomultipliers of Sci21 with respect to the position measured from the left and right photomultiplier tubes of the scintillator. Fig. 3.2 shows the charge collection in the left and right photomultipliers as a function of the position in the scintillator. There is a clear correlation between the charge collection and the measured position, thus a gate is applied to select the events with the correct relation.

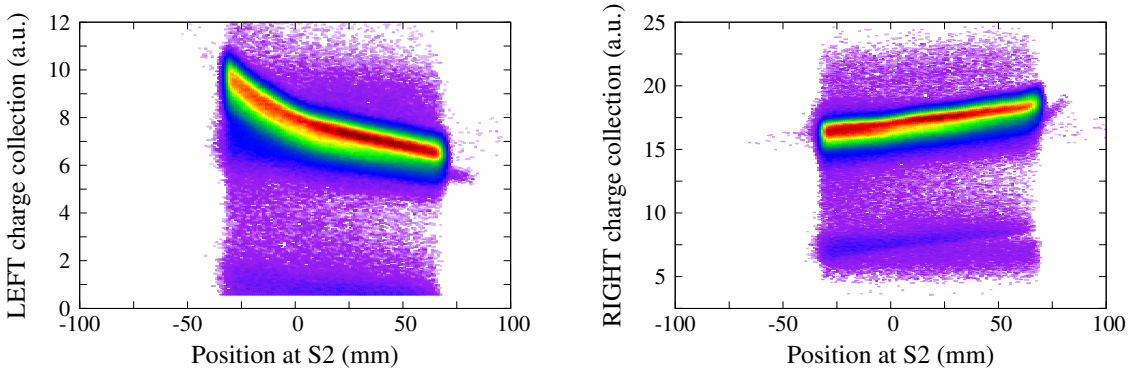

Figure 3.2: *Charge collected on the left PMT (***left***) and the right PMT (***right***) in Sci21 as a function of the position calculated using both PMTs.*

3.1.3 Energy loss in the intermediate degrader and charge states

In the majority of events, the projectile fragmentation reaction products are produced fully stripped (Z=Q). However, as explained in Section 2.2, when the ions pass through a layer of matter such as the degrader at S2, collisions within the medium take place, which can produce a change in their charge state. This process depends primarily on the energy, mass and ionic charge of the ions. Thus, in order to improve the identification, the energy loss in the degrader method (Bρ-Δp-Bρ) is used to identify the different charge states [64]. The energy loss in the degrader is related to the change in the Lorentz factors between the first and second stages of the FRS, as described by Eq: 2.7.

Fig. 3.3 shows the charge of the ions measured with the MUSIC detectors as a function of the energy loss through the S2 degrader. The different bands show the nuclei that did not change their charge state passing through the degrader ($\Delta q = 0$), picked up one or two electrons ($\Delta q = -1$, $\Delta q = -2$), or lost an electron ($\Delta q = +1$). If only $\Delta q = 0$ nuclei

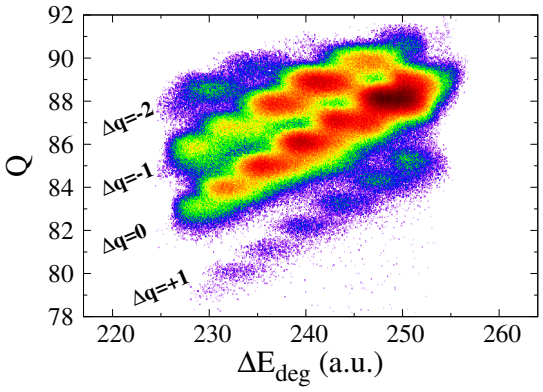

Figure 3.3: *Energy loss through the degrader as a function of the ionic charge measured with the MUSIC detectors.*

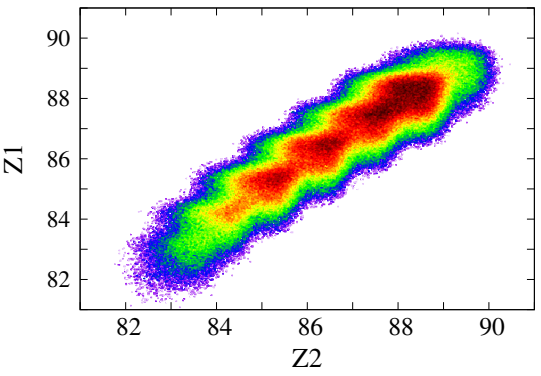

Figure 3.4: *Nuclear charge from MUSIC41 and MUSIC42 detectors when only fully stripped Q=Z nuclei are selected.*

are selected, the nuclear charge calculated from the signals from MUSIC41 and MUSIC42 detectors can be determined, as shown in Fig. 3.4.

3.1.4 Secondary reactions in the final degrader at S4

In order to fully stop the nuclei at the final focal plane at S4, they need to be slowed in an aluminium degrader placed between Sci41 and Sci42, as shown in Fig. 2.8. By measuring the energy loss of the nuclei passing through Sci42 as a function of the charge measured in the MUSIC detectors, events in which secondary nuclear reactions take place in the degrader can be identified and rejected in the data analysis. Fig. 3.5 shows a plot of the change of the charge measured with the MUSIC detectors as a function of the energy loss in Sci42, and indicates how a gate can be applied to select the nuclei that have not suffered any reaction in the degrader. In the data for the ^{212}Rn data set shown in the figure, 20% of the events undergo a nuclear reaction at the degrader at S4.

3.1.5 Veto detector

During the stopping process, not all the nuclei come to rest at the final focal plane. Some continue their trajectory until detected in the so called “veto” detector (Sci43), placed behind the RISING array, as shown in Fig. 2.8. Nuclei produced during nuclear reactions in the stopper will also be detected in the veto detector. Fig. 3.6 shows the veto detector signal. Events on the left of the red dividing line are stopped in the passive stopper and therefore valid event, while events on the right correspond to nuclei not being stopped at the final focal plane and are discarded from the data analysis.

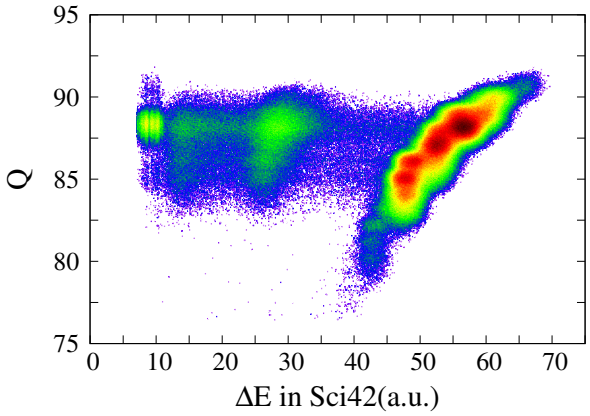

Figure 3.5: *The charge measured with the MUSIC detectors as a function of the energy loss in Sci42.*

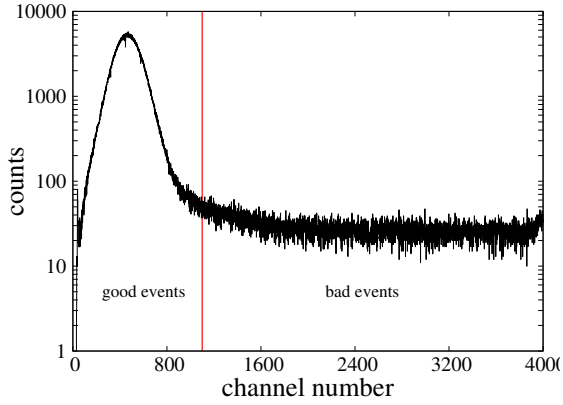

Figure 3.6: *The charge collection in the veto detector Sci43.*

3.2 Particle Identification

The identification of the nuclei of interest is done in terms of the A/Q ratio given by Eq. 2.4 and the nuclear charge Z. Fig. 3.7 shows the position of the nuclei at S4 plotted as a function of the A/Q ratio for the ^{212}Rn data set when the cleaning conditions are not applied (left) and when they are (right). On the plot on the left, the nuclei are overlapped because there are nuclei with the same A/Q ratio but different Z being implanted at the same position at the final focal plane. In addition, the noise coming from the scintillation and multiwire detectors is also included. After the cleaning conditions are applied, the identification plot contains only fully stripped nuclei which have been produced in a projectile fragmentation reaction, travelled through the FRS and stopped in the middle of the RISING array. Therefore in the plot on the right, each "blob" corresponds to a nucleus with a given A/Q and Z.

The A/Q ratio can also be plotted as a function of the position at the intermediate focal plane at S2, as shown in Fig. 3.8. As for the previous case, the left panel corresponds to the unclean data and the right panel represents the data after cleaning conditions are applied. On the top corner of the clean plot there is a small "blob" which comes from not fully stripped ions, which have not been cleaned during the energy loss through the intermediate degrader cleaning condition. Those events have also been removed from subsequent analysis.

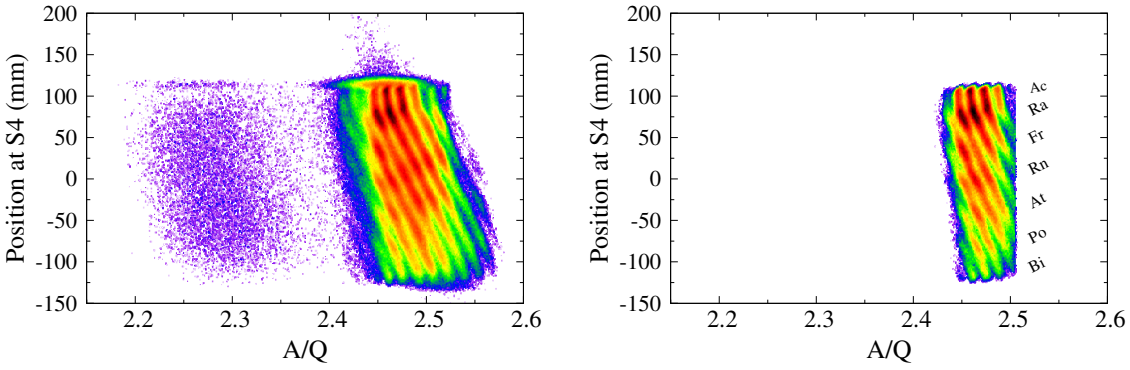

Figure 3.7: *The identification plot of the position at S4 as a function of the A/Q ratio for the ^{212}Rn data set without cleaning conditions (***left***) and with cleaning conditions (***right***). Each 'blob' on the clean plot corresponds to a nucleus with a given A/Q and Z.*

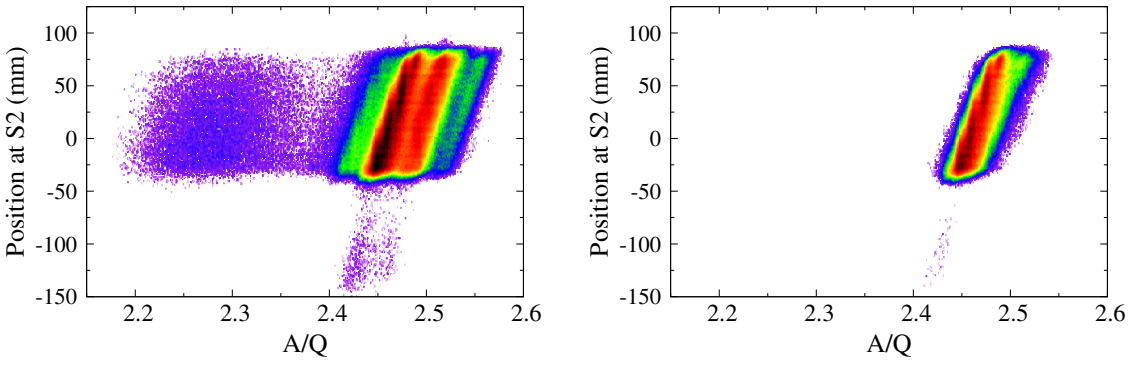

Figure 3.8: *A plot of the position at the intermediate focal plane at S2 as a function of the A/Q ratio without cleaning conditions (***left***) and with cleaning conditions (***right***). On the clean plot, a small 'blob' from not fully stripped ions and located on the top right band, has been also removed in the data analysis.*

All nuclei studied in this work have been previously reported, so the identification could be done without a charge identification on the identification plot. On the other hand, Fig. 3.9 shows a plot of the position at S4 as a function of the charge, indicating how well separated the different charges are, so separate A/Q plots can be extracted by gating on each Z separately. The charge identification on the left of Fig. 3.9 was produced

without applying any cleaning conditions and the one in the right includes all the cleaning conditions. The four bands seen in the left panel correspond to the different charge states and thus the gate on Q=Z nuclei leaves only the fully stripped nuclei, as shown in the right panel. All the information needed to obtain an unambiguous identification is provided by

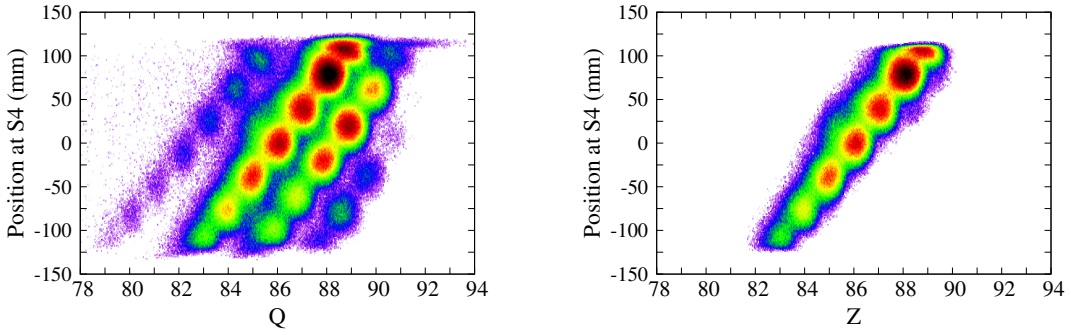

Figure 3.9: *The identification plot of the position at S4 as a function of Z for the ^{212}Rn data set without cleaning conditions (***left***) and with cleaning conditions (***right***).*

the A/Q and Z identification plots as shown in Fig. 3.10. In order to take advantage of the good charge separation, a gate on each Z is applied and an identification plot of the position at S4 as a function of A/Q is obtained for each charge. Fig. 3.11 shows the A/Q identification plot for each Z and on the bottom right panel the identification plot when no initial gate on Z is applied. A better separation of the different isotopes is achieved when the identification of A/Q is obtained for each Z. Each "blob" in this plots corresponds to

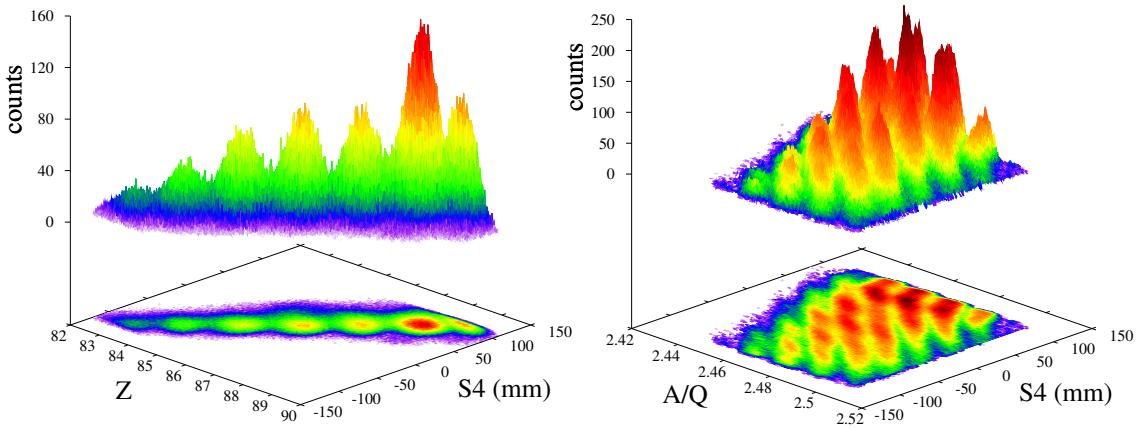

Figure 3.10: *The isotopic and charge identification plots for the ^{212}Rn data set.* **Left:** *Position at S4 as a function of Z.* **Right:** *Position at S4 as a function of A/Q. Gating on each Z on the left panel an independent A/Q identification plot can be obtained as shown in Fig. 3.11.*

a different nucleus, and gating on each of them, it is possible to obtain energy and timing information on the gamma rays emitted during their decay.

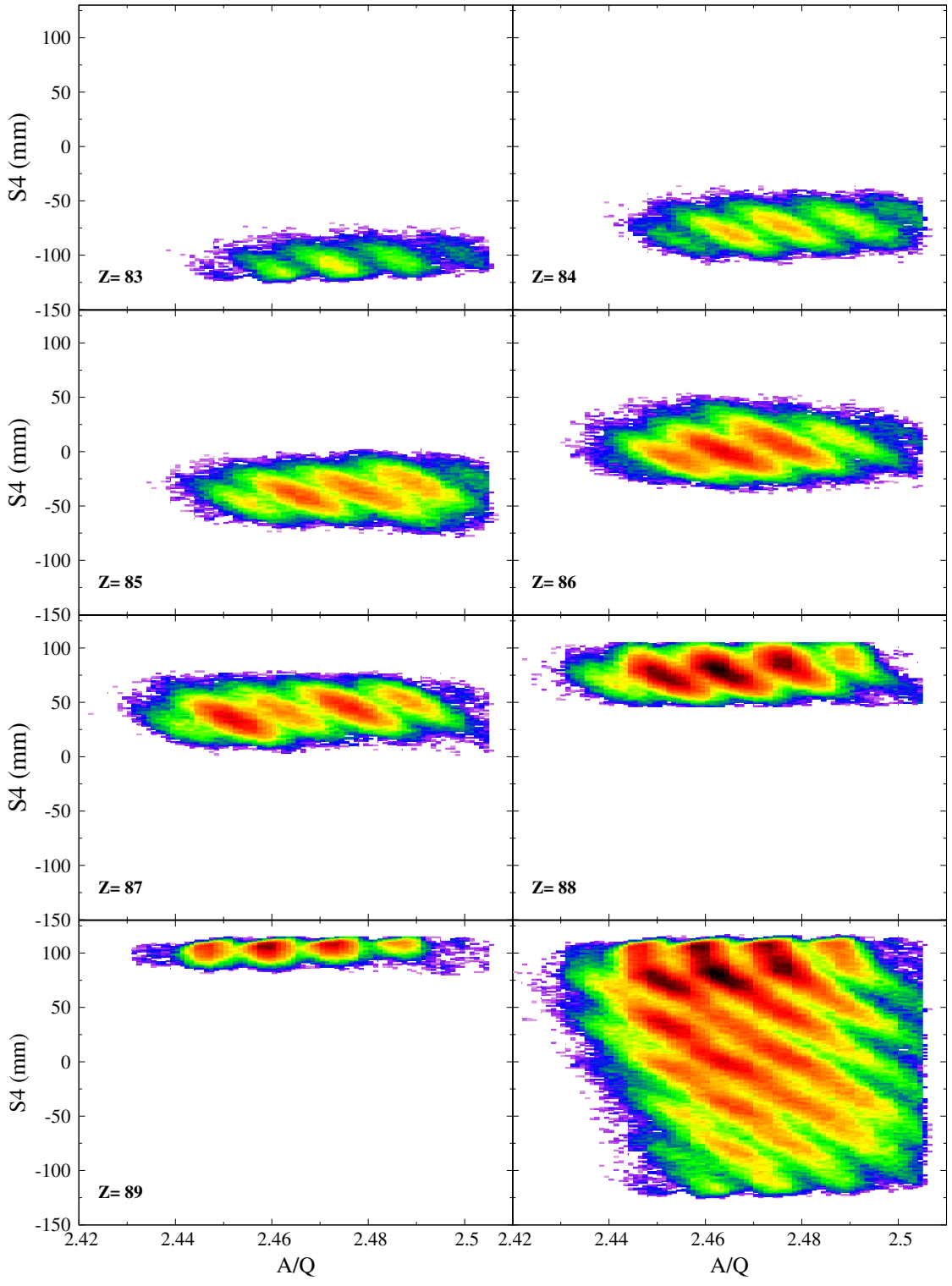

Figure 3.11: *The position at S4 as a function of A/Q for the ^{212}Rn data set gating on Bi, Po, At, Rn, Fr, Ra and Ac nuclei. The panel on the bottom right corner shows the A/Q identification plot when all Z are included. A clearer separation is obtained when an A/Q plot is obtained for each element.*

3.3 Isomeric-state identification

States which have an isomeric decay are identified by creating a matrix of the gamma-ray energy versus the time difference between implantation and detection for each nucleus. Fig. 3.12 shows the energy-time matrix on the left and the corresponding energy projection for ^{213}Rn on the right. The horizontal lines on the matrix are the gamma rays decaying from isomeric states. The so-called prompt flash is represented by the intense band to the left of the energy-time matrix.

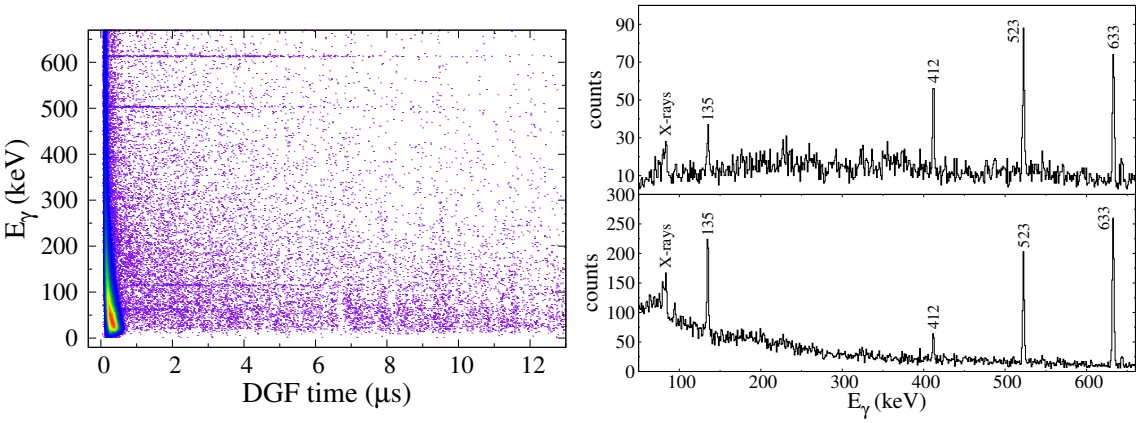

Figure 3.12: Left: *Energy-time matrix for ^{213}Rn.* **Right:** *Gamma-ray energy projections from the energy-time matrix for ^{213}Rn showing short and long time windows in the top and bottom panels respectively.*

3.3.1 Timing information and half-life fitting

The half-lives of the isomeric transitions are obtained from the energy-time matrix by projecting the energies of interest onto the time axis. Background subtraction is applied by selecting time projections above and below the energy of the transition of interest and normalising the number of counts to the same number of channels. Fig. 3.13 shows an example of the time projection of a transition, the normalised background and the final decay after background subtraction. The isomeric decay is then fitted to Eq. 3.2 to determine the half-life $t_{1/2}$. Due to the background reduction there is a probability of having a number of counts less than or equal to zero, which makes the fitting process difficult and therefore a random background constant C is added:

$$N(t) = N_0 e^{-\frac{ln2}{t_{1/2}}t} + C \tag{3.2}$$

If a nucleus has two isomers such as the number of decays from the upper isomer is $N_U(t)$ with a decay constant of λ_U, and then decays from the lower isomer $N_L(t)$ with a decay

constant λ_L, the half-life of the upper isomer feeding into the lower one and the half-life of the lower one are fitted as follows:

$$N_U(t) = N_{U0}e^{\lambda_U t} + C_U \tag{3.3}$$

$$N_L(t) = N_{L0}e^{-\lambda_L t} + \frac{\lambda_U}{\lambda_L - \lambda_U} N_{U0}\left(e^{-\lambda_U t} - e^{-\lambda_L t}\right) + C_L, \tag{3.4}$$

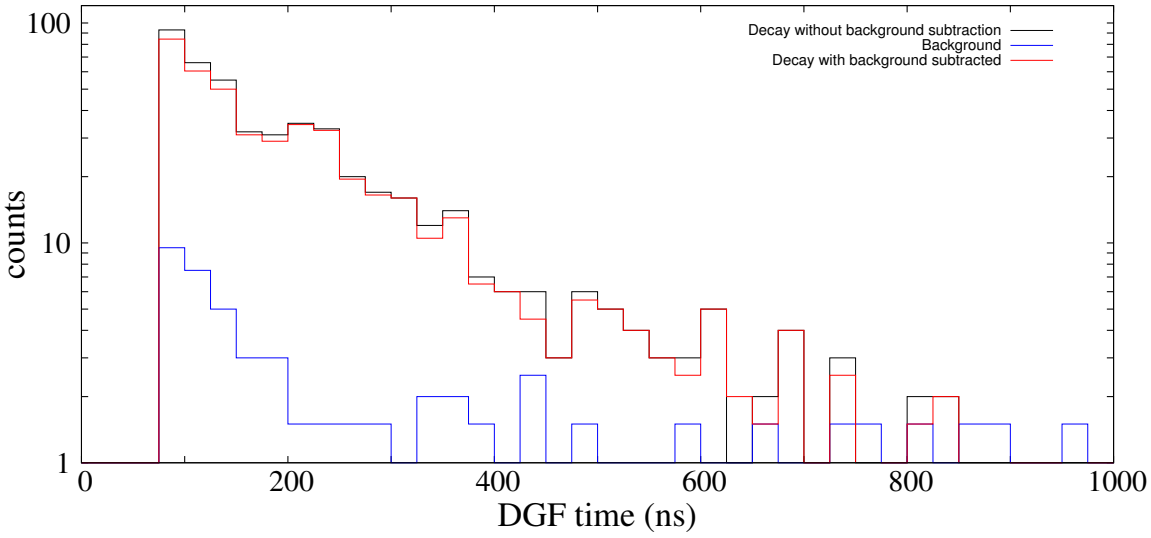

Figure 3.13: *An example of the time decay of an isomeric state. In black is the projection on the time axis of the transition. In blue is the normalised background projection. In red is the isomeric decay after background subtraction, from which the isomer half-life is extracted.*

3.4 Improving the quality of the energy spectrum: an add-back method for the RISING array

The RISING array consists of 15 clusters, each of which comprises seven close packed hexagonal HPGe crystals, making a total of 105 crystals. Fig. 3.14 shows a photograph of one of the hemispheres of the RISING array. The main mechanism of interaction of gamma rays at energies between 500 keV and 10 MeV with a germanium crystal (Z=32) is via Compton scattering [65]. Within this energy range and with the highly packed crystal configuration, photons can interact with one of the HPGe crystals and subsequently scatter to neighbouring crystals until the photon loses all its energy. If this is the case, only part of the energy is absorbed and detected within the first crystal, leading to an increase in the background and a decrease in the efficiency. This aspect can be quantified by

means of the peak-to-total ratio (P/T), defined as the number of counts in the full energy photo-peak divided by the total number of counts in the energy spectrum. The add-back method tries to reconstruct such events by adding together the energies which belong to the same gamma ray, but are deposited in different crystals due to Compton scattering. Two different scenarios can be considered for add-back algorithms applied in the RISING array: add-back within a cluster and add-back between different clusters. In this thesis, only add-back within a cluster is presented.

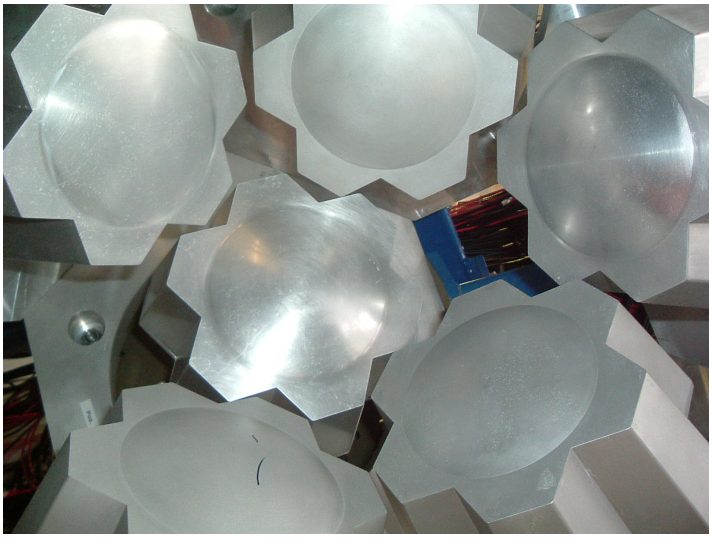

Figure 3.14: *A photograph of one of the hemispheres of the RISING array showing the cluster structure, each consisting of seven hexagonal high purity germanium crystals.*

To study the different add-back algorithms, a ^{60}Co source which has two gamma-ray transitions with energies 1173 keV and 1332 keV was used. Also a ^{152}Eu source was used to study the dependency of Compton scattering events with energy. Subsequently, the add-back routines were tested using two in-beam data sets, the ^{212}Rn setting collected during the experiment presented in this thesis, and the ^{98}Zr setting from a previous experiment (S300) at GSI in December 2006.

In order to quantify the effect of Compton scattering in the array, three factors need to be considered:

- **Crystal multiplicity:** the number of crystals that fire[3] in the array per event.
- **Cluster multiplicity:** the number of crystals that fire in a cluster per event.
- **Gamma rays per event:** the number of gamma rays detected in the array per event after reconstruction .

[3]A crystal has fired when it has non-zero energy and time signals.

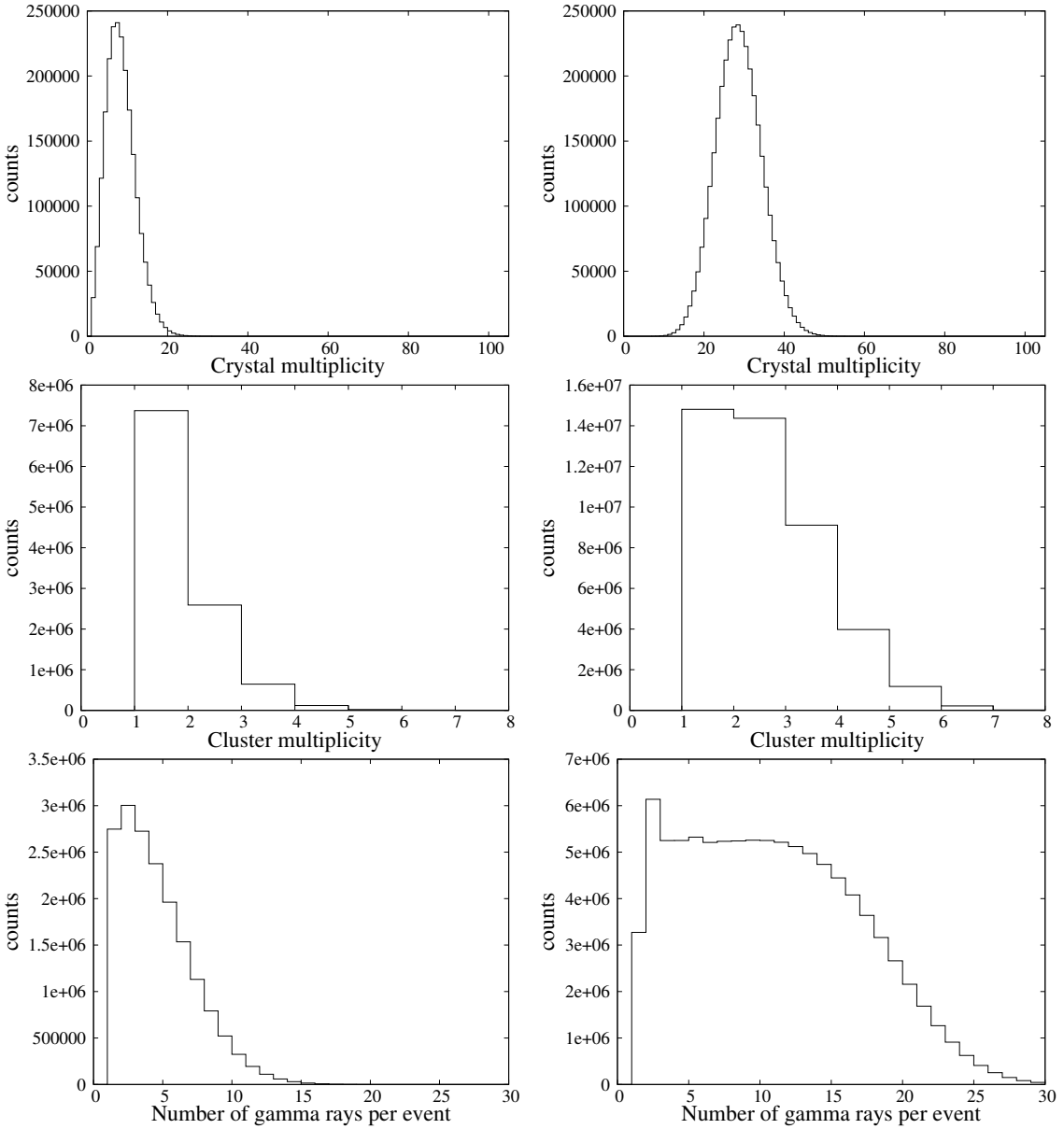

Figure 3.15: ***Upper:*** *crystal multiplicity.* ***Middle:*** *cluster multiplicity.* ***Lower:*** *number of gamma rays in each event. Data for* ^{60}*Co is shown on the left and* ^{152}*Eu on the right. Note the different scales for the different plots.*

The crystal and cluster multiplicities, and the number of gammas per event are shown in Fig. 3.15 for ^{60}Co on the left and for ^{152}Eu on the right. Due to the larger number of transitions in ^{152}Eu compared to ^{60}Co, the number of Compton scatter cases in a given event is larger. This is indicated in Fig. 3.15, where a distribution maximum of 8 crystals fire in each event for ^{60}Co compared with 29 crystals for ^{152}Eu. The same situation occurs with the cluster multiplicity and the number of gamma rays per event. Table 3.2 shows the cluster multiplicity distribution for both sources. Multiplicity 1 cases are those in which only one crystal has fired in a cluster, multiplicity 2 corresponds to two crystals firing and in multiplicity 3, three crystals have fired in a given cluster. Note that in each event,

different clusters can register different multiplicity cases, thus we refer to multiplicity cases and not multiplicity events. The results shown in Table 3.2 for ^{60}Co show that 92.6% of the events correspond to cluster multiplicities of 1 and 2, while for ^{152}Eu only 66.8% of the data corresponds to multiplicity 1 and 2 cases or 87.7% to multiplicity 1, 2 and 3 cases. This means that in the former case add-back could be implemented only for multiplicities 1 and 2, while for the latter, multiplicity 3 would also need to be considered.

Cluster mult.	1	2	3	4	5	6	7
^{60}Co (%)	68.5	24.1	6.0	1.1	0.2	∼0	∼0
^{60}Co (cases)	7371188	2590974	644448	119268	19716	7786	662
^{152}Eu (%)	33.9	32.9	20.9	9.1	2.7	0.5	∼0
^{152}Eu (cases)	14811399	14368478	9110743	3975283	1174922	220310	19002

Table 3.2: *Cluster multiplicity probabilities and number of cases for each multiplicity for ^{60}Co and ^{152}Eu source data.*

When more than one crystal fires in a cluster, the energy and time signals associated with the crystals must satisfy two conditions if they are to be considered as belonging to the same gamma ray:

1. The crystals which have fired must be adjacent. Fig. 3.16 shows the schematic of a cluster detector and its given numeration.

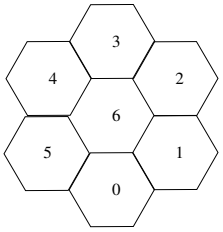

Figure 3.16: *A schematic of a cluster of the RISING array. The crystals are numbered anticlockwise in such way that the middle one is always the last one.*

2. The time difference between the time signals from the crystals that have fired should be short enough to ensure that they belong to the same gamma ray. Fig. 3.17 shows the logic used to calculate the time difference for multiplicities 2 and 3. For multiplicity 2 (M2) cases, the time is defined as the difference between the time signals for the scattered gamma ray:

$$dt_{M2} = abs\,(T1 - T2) \tag{3.5}$$

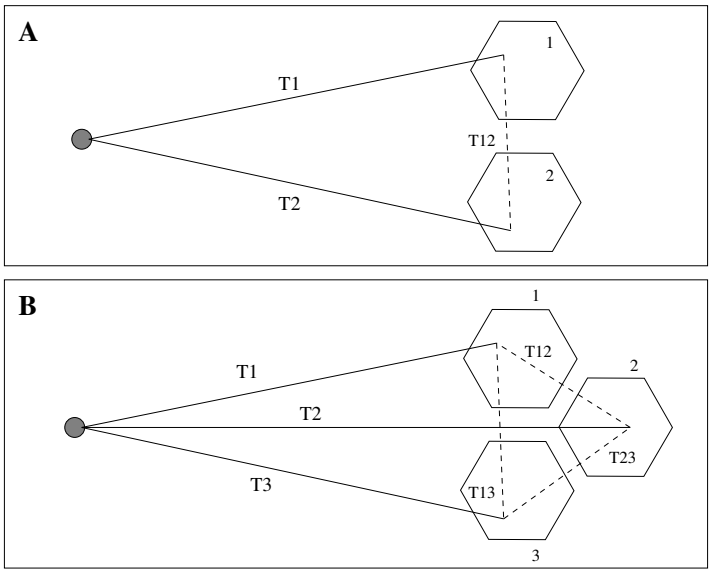

Figure 3.17: *A diagram of the time difference conditions for multiplicities two (***upper***) and three (***lower***), where T1, T2, and T3 are the DGF time signal from the fired crystals.*

For multiplicity 3 (M3) cases, the time is calculated as an average of the time differences from the three different trajectories that the scattered gamma ray can follow depending on the initial crystal, as follows:

$$\mathbf{1} = \frac{(T12 + T23) + (T13 + T23)}{2} \tag{3.6}$$

$$\mathbf{2} = \frac{(T12 + T13) + (T13 + T23)}{2} \tag{3.7}$$

$$\mathbf{3} = \frac{(T13 + T12) + (T12 + T23)}{2} \tag{3.8}$$

$$dt_{M3} = \frac{\mathbf{1} + \mathbf{2} + \mathbf{3}}{3} = \frac{2}{3}(T12 + T23 + T13) \tag{3.9}$$

where $T12 = abs(T1 - T2)$, $T23 = abs(T2 - T3)$ and $T13 = abs(T1 - T3)$. This logic is shown in Fig. 3.17. Fig. 3.18 shows the time difference distribution obtained using these algorithms for ^{60}Co. From the distributions, a time difference of 500 ns for multiplicity 2 cases and 625 ns for multiplicity 3 was chosen, in agreement with previous estimates [57].

If both conditions are satisfied, the two (three) energy signals for multiplicity 2 (multiplicity 3) cases are added together as a single gamma ray. The typical charge collection time for a HPGe crystal is longer than half a microsecond [49], which makes it impossible to identify which of the energy signals is detected first. Therefore the time signal associated with the added-back gamma ray is given by the time associated with the highest energy gamma-ray.

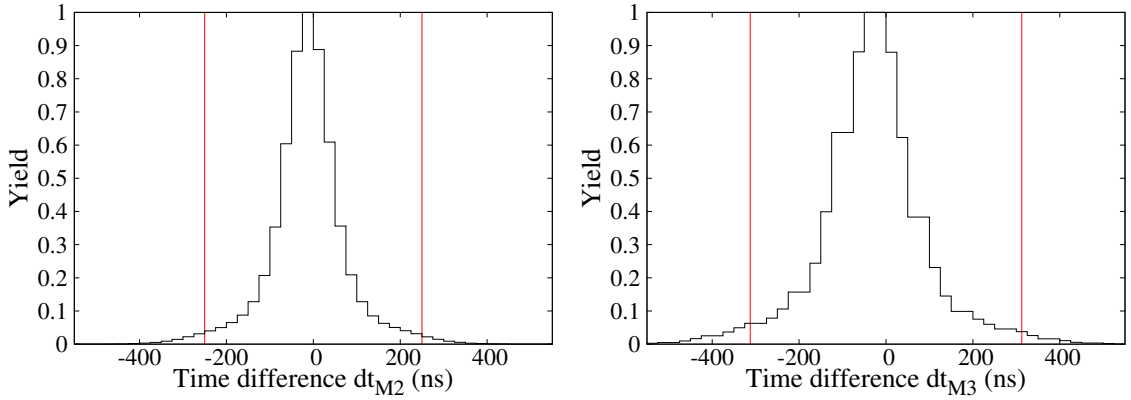

Figure 3.18: *The time difference distributions for multiplicities 2 (***left***) and 3 (***right***) for* ^{60}*Co.*

In the following sections, the case in which no add-back is applied is presented and compared with the results of applying add-back taking into account the different multiplicity cases. Firstly, the algorithm applied to multiplicities 1, 2 and 3 are discussed independently. Afterwards, the results of add-back applied when multiplicities up to three are considered are presented for ^{60}Co and ^{152}Eu source data. At the end of the chapter the results of add-back applied to in-beam data are presented and discussed.

3.4.1 No add-back

When no add-back is applied, all the energy signals measured in each fired crystal are included in the energy spectrum as separate gamma rays. Fig. 3.19 shows the ^{60}Co energy spectrum constructed in this way, and Table 3.3 shows the P/T ratios for the different peaks calculated with background subtraction.

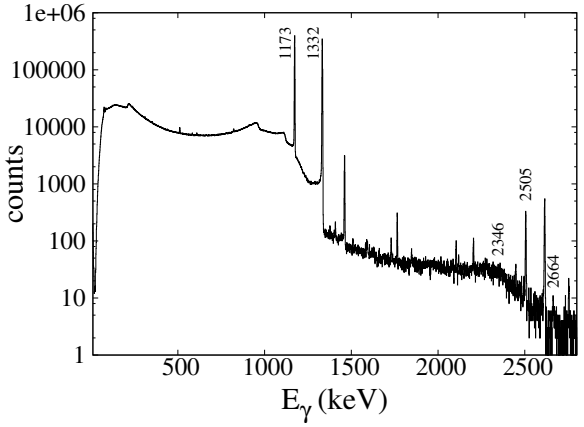

Figure 3.19: ^{60}*Co energy spectrum when no add-back method is applied.*

E (keV)	counts	P/T (%)
1173	1135142	7.5
1332	1050806	7.0
2346	44	2.9 10^{-4}
2505	1182	0.0078
2664	41	2.7 10^{-4}
total	15043960	

Table 3.3: *Peak-to-total ratios with background subtraction.*

The energy spectrum shows the 1173 keV and 1332 keV gamma-ray transitions in ^{60}Co. The unlabelled peaks are from background radiation: 1462 keV from ^{40}K, 1764 keV and 2204 keV from ^{214}Bi (^{238}U decay chain), 2103 keV and 2614 keV from ^{208}Tl (^{232}Th decay chain) and 2753 keV from ^{22}Na (cosmic rays). The 2505 keV peak correspond to events in which the two gamma rays in the cascade (1173+1332 keV) are detected in coincidence in the same crystal. The 2346 keV and 2664 keV peaks are random coincidences, where two 1173 keV or 1332 keV gamma rays are detected simultaneously from different decays due to the high counting rate and the time window of the DAQ. Table 3.3 shows the P/T ratios for the 1173 and 1332 keV gamma rays, 2505 keV peak true coincidences, and 2346 and 2664 keV chance coincidences. In the following sections these P/T ratios are compared with those obtained as a result of applying different add-back algorithms for each multiplicity case.

3.4.2 Multiplicity 1

Multiplicity 1 cases are defined as those in which only one crystal within a given cluster has fired. In this case, the gamma-ray energy and time are considered as a single gamma ray absorbed in the crystal, as shown in Fig. 3.20. If during the same event two or more crystal have fired within a cluster, those cases are rejected and not added to the energy spectrum.

Fig. 3.21 shows the energy spectrum constructed in this way, compared with the one in which no add-back is applied. The total number of counts in the spectrum is approximately equal to the number of multiplicity 1 cases shown in the cluster multiplicity Table 3.2. Table 3.4 shows the P/T ratios obtained considering only multiplicity 1 cases. The P/T increases from 7.5% in Table 3.3 to 10.6% at 1173 keV, but the number of counts in the photopeak decreases by 31%. The P/T ratios for the true and random coincidence events are essentially the same as for the no add-back applied case.

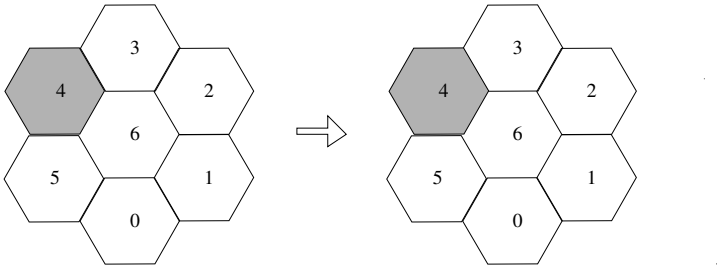

Figure 3.20: *A diagram of a multiplicity 1 case. The left part represents the cluster before add-back is applied and the right one, after add-back is applied.*

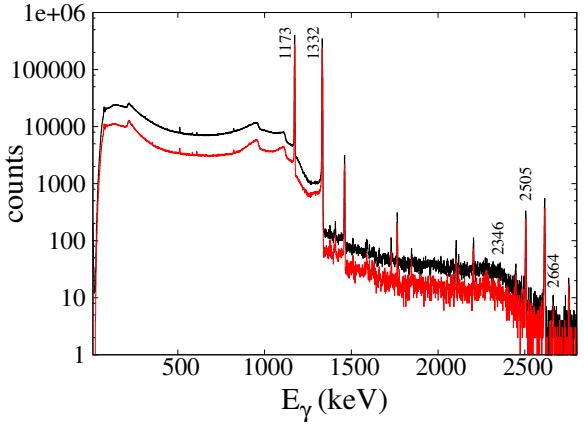

Figure 3.21: ^{60}*Co energy spectra for multiplicity 1 cases (red) compared with the no add-back applied case (black).*

E (keV)	counts	P/T (%)
1173	780138	10.6
1332	719796	9.8
2346	17	2.3 10^{-4}
2505	833	0.011
2664	18	2.3 10^{-4}
total	7370592	

Table 3.4: *Peak-to-total ratios with background subtraction for multiplicity 1 cases.*

3.4.3 Multiplicity 2

Multiplicity 2 cases are defined as those in which only two crystals have fired within a given cluster. When the two crystals within a cluster are adjacent and the associated time difference defined in Eq. 3.5 is shorter than 500 ns, the energies are added together as a single gamma ray and the time signal assigned is the one associated with the higher energy signal. The added-back gamma ray is assigned to the crystal in which the energy deposited is greater. Otherwise, the two energy signals are considered as two separate single gamma rays. Fig. 3.22 shows the scheme for a multiplicity 2 case. There are twelve different combinations of two adjacent crystals, and nine combinations of non-adjacent.

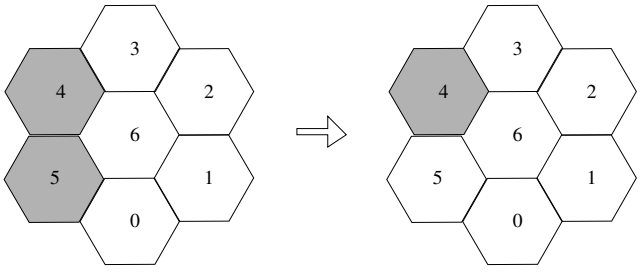

Figure 3.22: *Diagram of a multiplicity 2 case. Two adjacent crystals have fire and if the time difference between the signals is less than 500 ns, the energies are added together and assigned to the crystal with the highest energy. There are twelve possible combinations of having two adjacent crystals in a cluster.*

Fig. 3.23 compares the energy spectrum as a result of applying add-back for multiplicity 2 cases with the spectrum with the no add-back applied case. In order to compare the total number of counts in the spectrum with the total number of multiplicity 2 cases given in Table 3.2, is necessary to know how many of the multiplicity 2 cases have fulfilled the add-back conditions. Of the 2590974 multiplicity 2 cases, 49.7% are add-back, so

2590974×0.497×1γ + 2590974×0.503×2γ makes a total of ∼3894000 counts, which is approximately equal to the total number of counts in the energy spectrum, as shown in Table 3.5. Fig. 3.24 shows in red the energy spectrum for the 49.7% of cases with the energies added-back compared with the spectrum of the same cases treated as single gamma rays. The added-back case results in a clear reduction in the background and a corresponding improvement in the P/T.

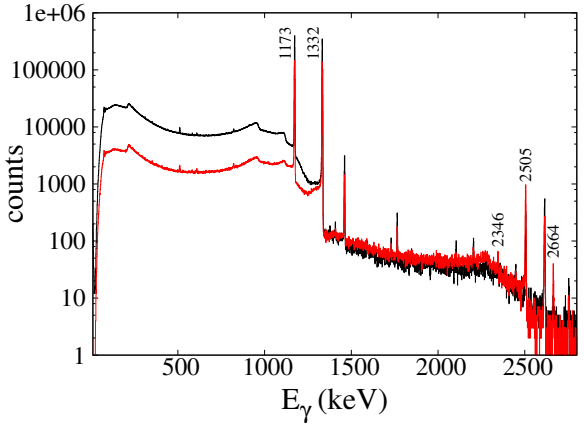

Figure 3.23: ^{60}*Co energy spectra for multiplicity 2 events (red) compared with the no add-back applied case (black).*

E (keV)	counts	P/T (%)
1173	503104	12.9
1332	477647	12.3
2346	145	0.0037
2505	4041	0.10
2664	146	0.0038
total	3891352	

Table 3.5: *Peak-to-total ratios with background subtraction for multiplicity 2 cases.*

Table 3.5 shows the P/T values for multiplicity 2 cases extracted from the spectrum in Fig. 3.23. The P/T increases from 7.5% in Table 3.3 to 12.9% at 1173 keV. The number of counts and P/T ratios in the true and random coincidence peaks is larger than for previous cases, implying that in some of the multiplicity 2 cases, two real gamma rays are being added together incorrectly. This can occur if the 1173 and 1332 keV gamma rays in the decay are detected in two different crystals within a cluster in a time shorter than the 500 ns time difference condition.

3.4.4 Multiplicity 3

Multiplicity 3 cases are defined as those in which three crystals have fired within a given cluster. As shown in Fig. 3.25, two subcases can be distinguished within a multiplicity 3 case when two or three crystals are adjacent:

1. **Three adjacent crystals:** If the time difference between the three signals, as defined in Eq: 3.9, is shorter than 625 ns, and the three crystals are adjacent, as defined on the top panel in Fig. 3.25, then the three energy signals are added together as a single gamma ray. The time signal assigned to the gamma ray is the

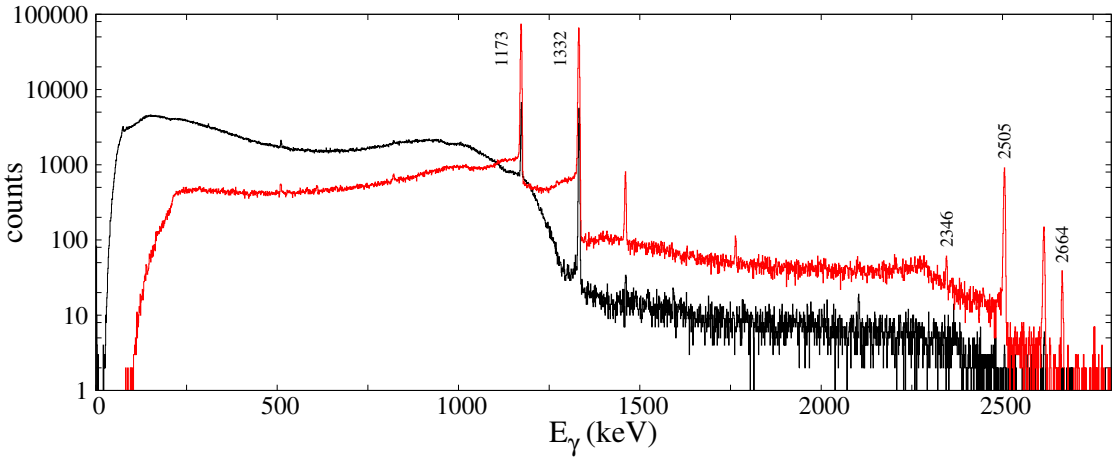

Figure 3.24: *Energy spectrum of the multiplicity 2 cases that satisfied the add-back conditions. The red spectrum shows the two gamma ray energies added together and in the black spectrum the energies are treated as separate gamma rays.*

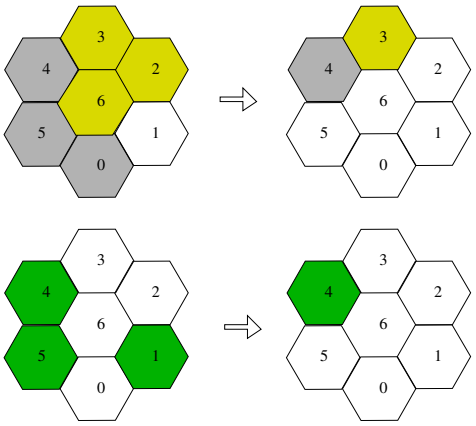

Figure 3.25: *A diagram of a multiplicity 3 case. The upper panel shows the two possible configurations of adjacent multiplicity three cases, triangular configuration (yellow) and linear configuration (grey). The lower panel shows the multiplicity 3 case, when two crystals are adjacent and one is not.*

time associated with the highest energy signal, and the gamma ray is assigned to that same crystal. The crystals can be adjacent in two different configurations:

(a) Triangular configuration: The upper panel in Fig. 3.25 shows in yellow an example of three adjacent crystals in a triangular configuration. There are six different combinations of crystals in that configuration.

(b) Linear configuration: The upper panel in Fig. 3.25 shows in grey an example of three adjacent crystals in a linear configuration. There are fifteen different combinations of crystals in that configuration.

2. **Two adjacent crystals and one not (2+1):** If two of the three crystals are adjacent as defined in the lower panel of Fig. 3.25, and their time difference, as defined in Eq: 3.5, is shorter than 500 ns, then their two energy signals are added together as a single gamma ray. This is equivalent to the multiplicity 2 case, discussed in Subsection 3.4.3, so the time and crystal number are assigned to the crystal with the higher energy. The energy and time signals from the non adjacent crystal are considered as a separate gamma ray.

If the adjacency and time conditions are not satisfied, the three energy signals and associated times are treated as three separate gamma rays.

Each combination of crystals is characterised by a given combination number. Fig. 3.26 shows the combination numbers when the multiplicity 3 add-back conditions are fulfilled, for the three different adjacency configurations: triangular, linear and two crystals adjacent and one not. In 37% of the cases three adjacent energy signals were added-back, of which 20% and 17% were in the triangular and linear configurations respectively. In 41% of the cases, two energy signals were added-back and the third one was treated as a separate gamma ray from a non-adjacent crystal. Only 22% of the cases did not satisfy the add-back conditions and were therefore treated as three separate gamma rays.

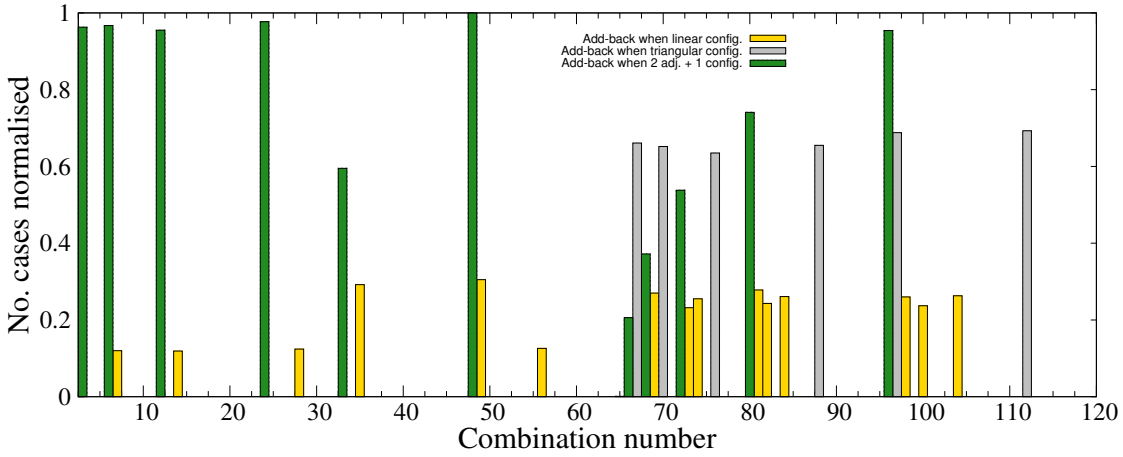

Figure 3.26: *Combination number calculated for three crystals, showing the normalised number of cases of an add-back case, for triangular configuration cases (grey), linear configuration cases (yellow) and 2+1 cases (green).*

Fig. 3.27 compares the energy spectrum as a result of applying add-back for multiplicity 3 cases with the no add-back applied case. In order to compare the total number of counts in the energy spectrum with the total number of multiplicity 3 cases given in Table 3.2, it is necessary to know how many of the multiplicity 3 cases have fulfilled the add-back conditions. Of the 644448 multiplicity 3 cases, 37% correspond to add-back between three

crystals, and 41% are two in add-back plus one. Thus, 0.37×644448 + 0.41×644448×2γ + 0.22×644448×3γ makes a total of around 1.2 million counts which is consistent with the number indicated in Table 3.6

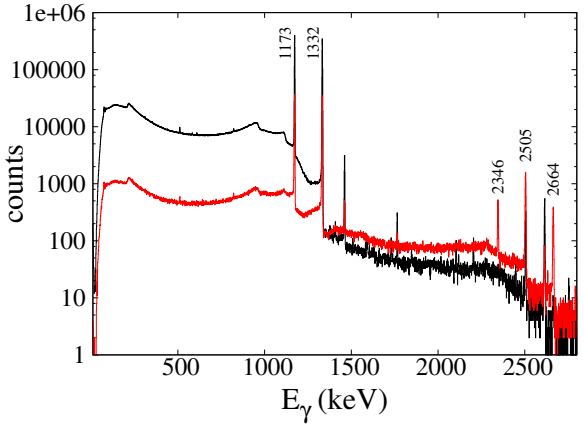

Figure 3.27: *^{60}Co energy spectra for multiplicity 3 events (red) compared with the no add-back applied case (black).*

E (keV)	counts	P/T (%)
1173	135938	11.4
1332	130185	10.9
2346	2153	0.18
2505	7693	0.64
2664	1944	0.16
total	1195336	

Table 3.6: *Peak-to-total ratios with background subtraction for multiplicity 3 cases.*

Fig. 3.28 shows in red the energy spectrum for the 37% of cases in which the three energy signals were added-back together compared with the spectrum of the same cases when the energies are treated as separate gamma rays. It is clear from the figure that the added-back case results in a clear reduction in the background and an improvement in the P/T ratio.

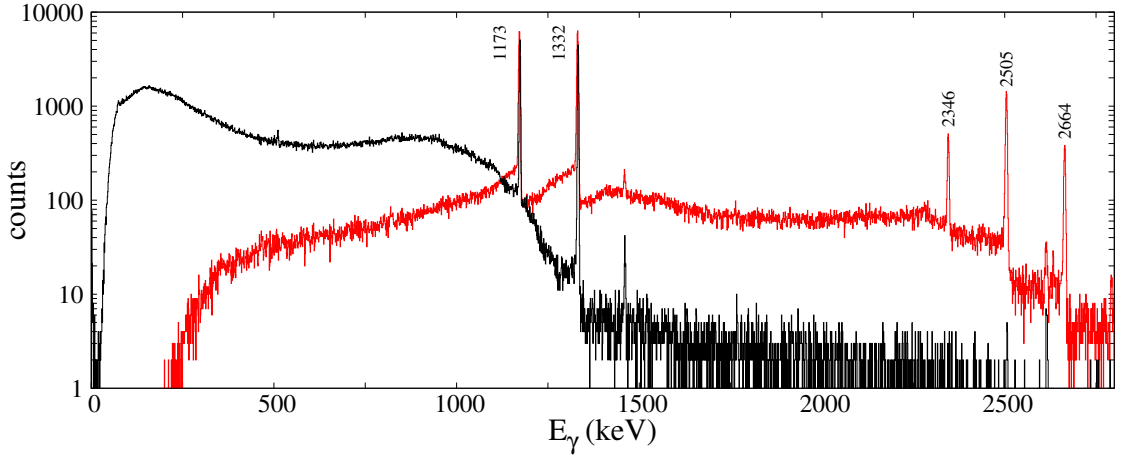

Figure 3.28: *Energy spectrum of the multiplicity 3 cases that satisfied the add-back conditions. The red spectrum shows the three gamma ray energies added together and in the black spectrum the energies are treated as separate gamma rays.*

The P/T ratio increases from the 7.5% in Table 3.3 to 11.4% for the 1173 keV peak. As in the multiplicity 2 case, the number of true and random coincidences also increases.

3.4.5 The results of applying add-back to the ^{60}Co and ^{152}Eu source data

Fig. 3.29 combines Figs. 3.21, 3.23 and 3.27 and shows the energy spectra measured for the ^{60}Co source for multiplicities up to three separately, compared with the case in which no add-back algorithm is applied. Multiplicities higher than 3 are not considered due to their low probability, as shown in Table 3.2. These cases have been rejected and are not included in the energy spectra.

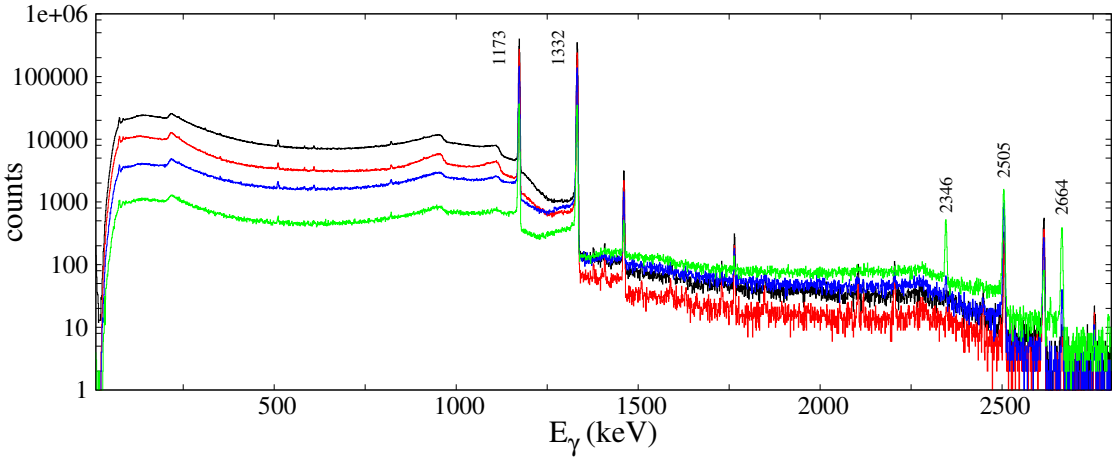

Figure 3.29: *^{60}Co energy spectra for multiplicities 1 (red), 2 (blue) and 3 (green) compared with the no add-back applied case (black).*

Fig. 3.30 shows the energy spectrum when multiplicities 1 and 2 cases are considered, and Table 3.7 shows the calculated P/T ratios. Multiplicities greater than 2 are rejected and not included in the spectrum. The peak to total ratio improves from 7.5% in Table 3.3 to 11.4% and the number of counts in the photopeak increases by 13% for the 1173 keV peak compared with the case in which no add-back is applied.

Fig. 3.31 compares the energy spectrum when add-back is applied to multiplicity 1, 2 and 3 cases, with the case in which no add-back algorithm is applied. Table 3.8 shows the calculated P/T ratios, which increase from 7.5% in Table 3.3 to 11.4% and the number of counts increase by 25% for the 1173 keV transition when multiplicities up to 3 are considered. Comparing the results from Tables 3.7 and 3.8, the P/T ratios do not change when multiplicity 3 cases are also considered. This is not unexpected since Table 3.2 shows that multiplicity 3 cases represent only 6% of the ^{60}Co source data, and are therefore expected to have only a small effect.

Table 3.9 summarizes the results of the add-back algorithms for the ^{60}Co source data. The P/T ratios show that in order to improve the quality of the energy spectrum multiplicities 1 and 2 should be considered. When multiplicity 3 cases are also included, the P/T ratios

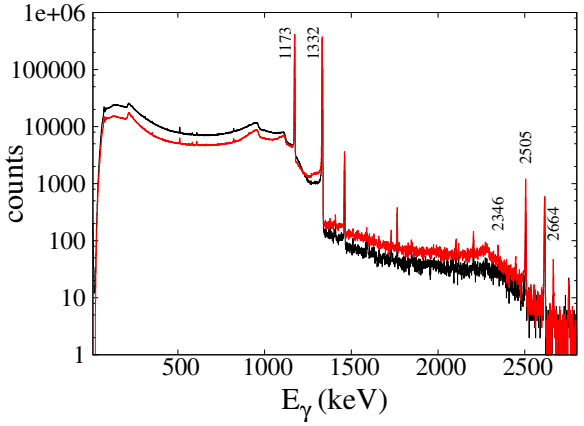

Figure 3.30: *^{60}Co energy spectra for multiplicities 1 and 2 (red) compared with the no add-back applied case (black).*

E (keV)	counts	P/T (%)
1173	1284208	11.4
1332	1198542	10.6
2346	189	0.0017
2505	4896	0.043
2664	167	0.0015
total	11261944	

Table 3.7: *P/T ratios with background subtraction when add-back is applied to both multiplicity 1 and 2 cases.*

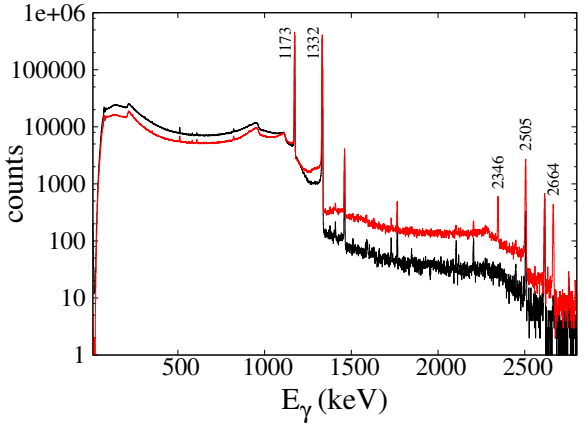

Figure 3.31: *^{60}Co energy spectra for multiplicities 1, 2 and 3 (red), compared with the no add-back applied case (black).*

E (keV)	counts	P/T (%)
1173	1419397	11.4
1332	1329122	10.7
2346	2285	0.018
2505	12567	0.10
2664	2111	0.017
total	12457280	

Table 3.8: *P/T ratios with background subtraction when add-back is applied to multiplicities 1, 2 and 3.*

E (keV)	**No add-back**	**M1**	**M2**	**M3**	**M1+M2**	**M1+M2+M3**	
	P/T (%)	P/T (%)	P/T (%)	P/T (%)	P/T (%)	P/T (%)	Improvement (%)
1173	7.5	10.6	12.9	11.4	11.4	11.4	52
1332	7.0	9.8	12.3	10.9	10.6	10.7	53
2346	2.9 10^{-4}	2.3 10^{-4}	0.0037	0.18	0.0017	0.018	-60
2505	0.0078	0.011	0.10	0.64	0.043	0.10	-12
2664	2.7 10^{-4}	2.3 10^{-4}	0.0038	0.16	0.0015	0.017	-62

Table 3.9: *Summary of the P/T ratios obtained for the ^{60}Co source data when no add-back is applied and when multiplicity 1, 2, 3, 1+2 and 1+2+3 cases are considered. Also the improvement in the P/T for the latter case is shown.*

do not change significantly but the number of counts in the photopeak increases by 11% compared with the case in which only multiplicity 1 and 2 cases are taken into account. Therefore, including multiplicities up to three in the add-back algorithm has the benefit

of increasing the number of counts in the photopeak (see Tables 3.7 and 3.8), while the P/T remains approximately constant.

Due to the large number of gamma rays in ^{152}Eu in the energy range between 121 keV and 1.4 MeV, an analysis of the add-back algorithm as a function of gamma ray energy can be performed. The probability of Compton scattering increases with increasing energy, so the add-back algorithm should provide better results for higher energy transitions. Fig. 3.32 compares the energy spectrum for ^{152}Eu when add-back is applied considering multiplicity 1,2 and 3 cases with the no add-back applied case, and Table 3.10 shows the calculated P/T ratios. As for the ^{60}Co source data, multiplicities greater than 4 are not considered and therefore those cases are not included on the analysis when add-back is applied. Fig. 3.33 shows the improvement in the calculated P/T ratios for ^{152}Eu when add-back is applied as a function of transition energy. It shows a clear increase in the P/T ratios for higher energies as expected.

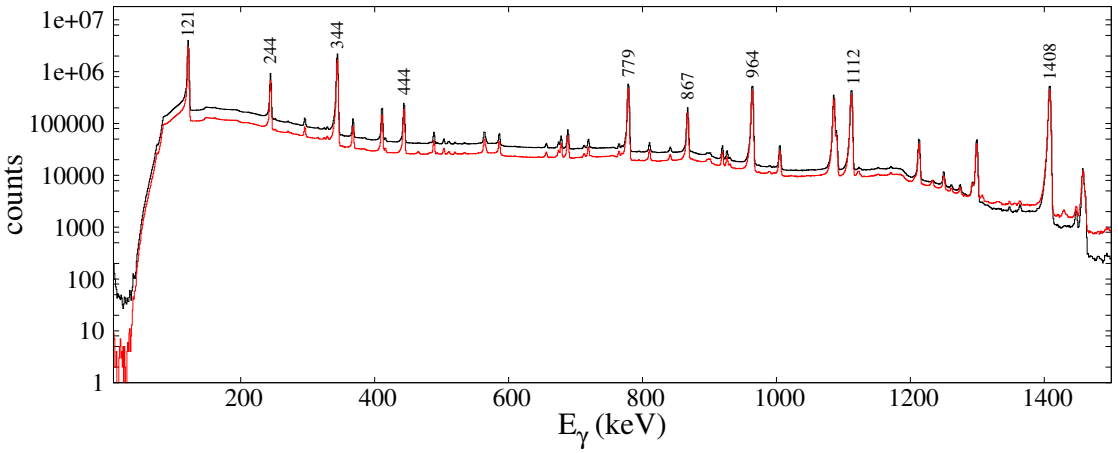

Figure 3.32: ^{152}*Eu energy spectra when add-back is applied to multiplicity 1, 2 and 3 cases (red), compared with the no add-back applied case (black).*

The results of applying add-back to ^{60}Co source data show that the P/T ratios improve significantly, from 7.5% to 11.4% for the 1173 keV transition, with an increase of 25% in the number of counts in the photopeak. The situation is different for the ^{152}Eu source data, where the P/T ratio increases from 1.5% to 1.9% for the 1112 keV transition, but the number of counts in the photopeak decreases by 13%. For large crystal and cluster multiplicities, as is the case for the ^{152}Eu source data, the results of applying add-back are a slight increase of the P/T, but the number of counts in the photopeak decreases.

	No add-back		Add-back		
E (keV)	counts	P/T (%)	counts	P/T (%)	Improvement (%)
121	9555225	10.2	7238638	10.9	6.9
244	1992554	2.2	1538115	2.3	4.5
344	5791458	6.2	4546168	6.9	11.3
444	589454	0.63	470893	0.71	12.7
779	1657588	1.8	1392027	2.1	16.7
867	528549	0.56	438843	0.66	17.8
964	1678145	1.8	1435703	2.2	22.2
1112	1440876	1.5	1255901	1.9	26.7
1408	1887832	2.0	1650302	2.5	25.0
total	94037720		66131992		

Table 3.10: *^{152}Eu peak-to-total ratios with background subtraction when add-back is applied to multiplicity 1,2 and 3 cases (***right***), compared with the case in which no add-back is applied (***left***). Also the improvement as a result of applying add-back is shown.*

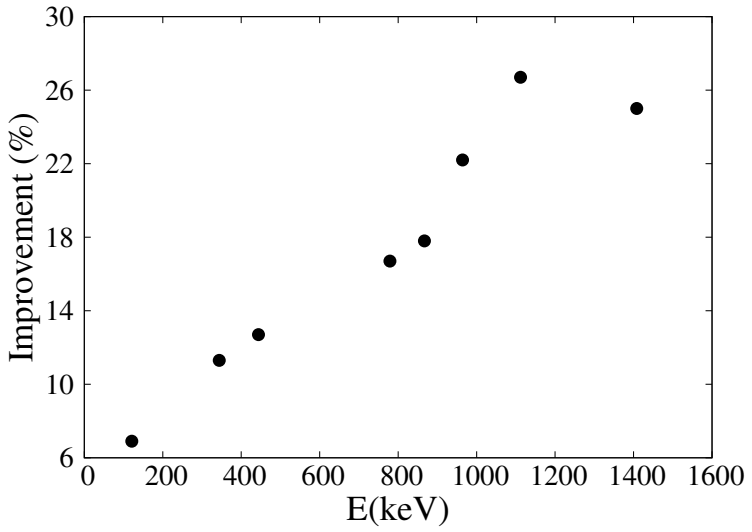

Figure 3.33: *Improvement in the peak-to-total ratios as a function of the gamma ray energy when add-back is applied to multiplicity 1, 2 and 3 cases for ^{152}Eu source data.*

3.4.6 The results of applying the add-back algorithm to the in-beam data

The add-back algorithms applied to the source data in the previous sections have been also tested on the in-beam data. Two different data sets have been used, the ^{212}Rn data set collected in the experiment presented in this work, and the ^{98}Zr data set, collected during a previous experiment at GSI, in December 2006. In this data, the acquisition is triggered by Sci41 and remains open for 100 μs. Therefore any gamma-rays which arrive during this time interval are included in each event.

3.4.6.1 The effect of using add-back for multiplicity 1, 2 and 3 cases on transitions in ^{211}Rn

Fig. 3.34 shows the cluster and crystal multiplicities, and the number of gamma rays per event after applying add-back including multiplicity 1, 2 and 3 cases for the ^{212}Rn data set. The figure shows that the number of crystals that have fired in an event is large, similar to the ^{152}Eu case shown in the right panel in Fig. 3.15. The probability of having one or more crystals that have fired within a cluster in an event is shown in Table 3.11, where 85 % of the data corresponds to cluster multiplicity 1, 2 and 3 cases.

Cluster multiplicity	1	2	3	4	5	6	7
^{212}Rn (%)	35.3	30.7	19.0	9.3	3.9	1.6	0.2

Table 3.11: *Cluster multiplicity probabilities for the ^{212}Rn setting.*

The effect of the add-back algorithm when multiplicity 1, 2 and 3 cases are considered, is studied for transitions in ^{211}Rn, populated in the ^{212}Rn data set. This nucleus has three gamma rays in cascade (120, 918 and 540 keV), decaying from a 596 ns isomer. The large range of energies is ideal to test the add-back algorithm at low and high energies. Cluster multiplicities greater than 3 have not been included in the analysis. Fig. 3.35 compares the energy spectrum calculated in this way with the case in which add-back is not applied. The added-back energy spectrum shows a sudden increase in the number of counts between 200 and 500 keV, due to the inclusion of events from the prompt-flash in the time difference calculation. This is due to the add-back algorithm picking up the small time differences associated with prompt flash events as real gamma rays and adding them together. If those events are rejected, then, the spectrum on Fig. 3.36 is obtained, where the small "bump" disappears without affecting the number of counts in the peaks. The P/T ratios are calculated for the latter case and shown in Table 3.12

	No add-back		Add-back		
E (keV)	counts	P/T (%)	counts	P/T (%)	Improv. (%)
120	231	1.43	152	1.61	12.6
540	765	4.73	465	4.92	4.0
918	562	3.48	381	4.03	15.8
total	16161		9445		

Table 3.12: *^{211}Rn peak-to-total ratios when add-back is not applied (***left***), and when add-back is applied considering multiplicities 1,2 and 3 for events outside the prompt flash (***right***). The last column shows the improvement in the P/T ratios when add-back is used.*

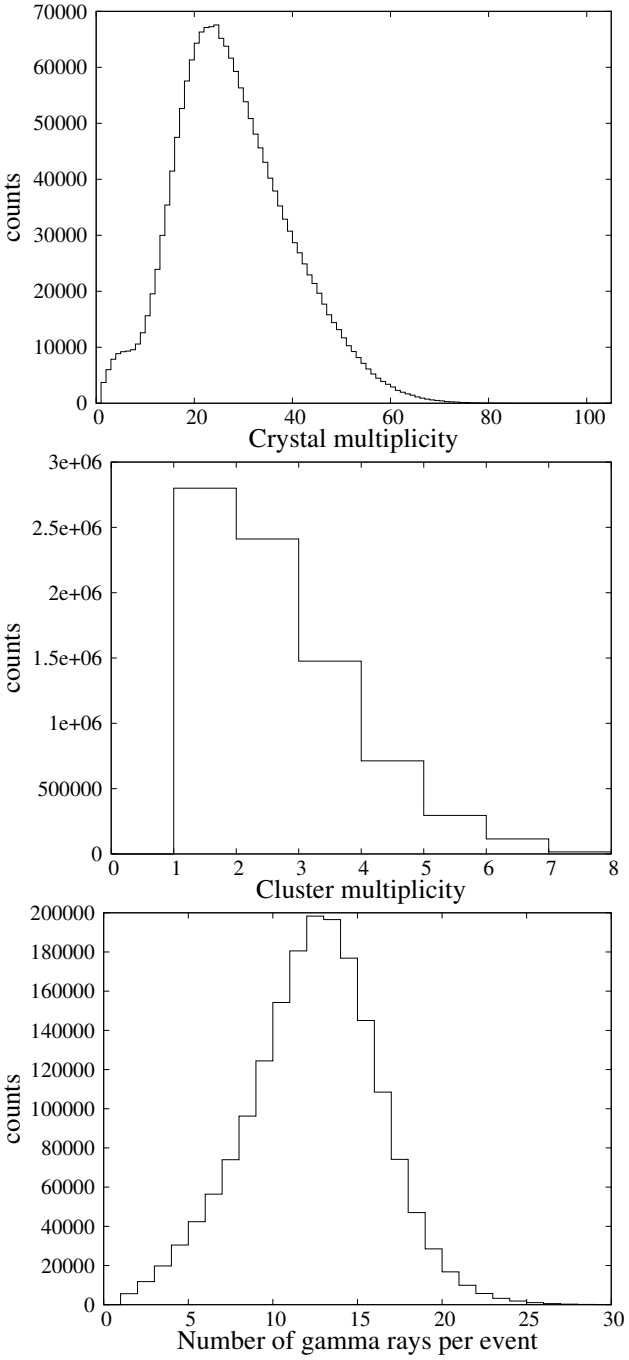

Figure 3.34: ***Upper:*** *crystal multiplicity* ***Middle:*** *cluster multiplicity* ***Lower:*** *number of gamma rays in each event after applying add-back for multiplicity 1, 2 and 3 cases for the* ^{212}Rn *data set. Note the different scales for the different plots.*

The results in Table 3.12 show that the P/T increases when add-back is applied, but the number of counts in the peaks decreases between 32% and 40% depending on the peak.

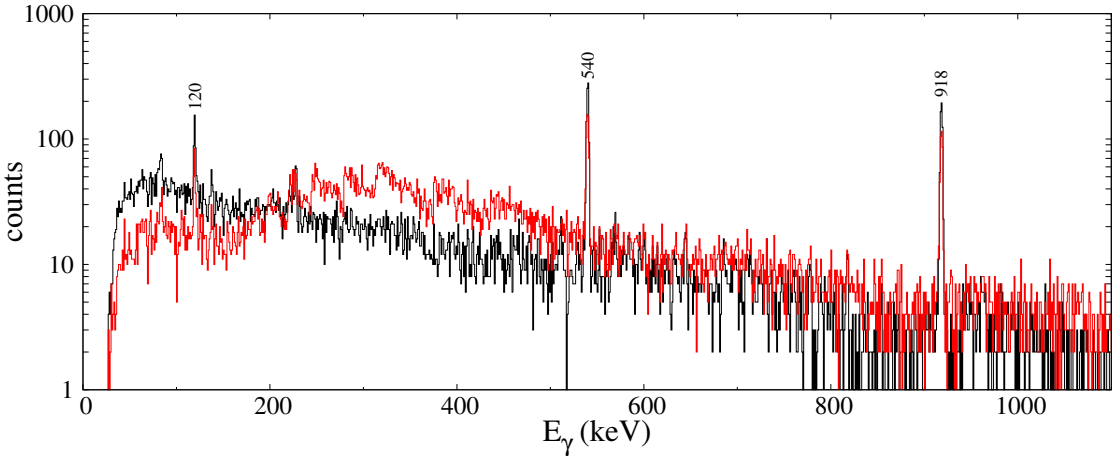

Figure 3.35: ^{211}*Rn energy spectrum when no add-back is applied (black) compared with the case in which add-back is applied to multiplicity 1,2 and 3 cases (red).*

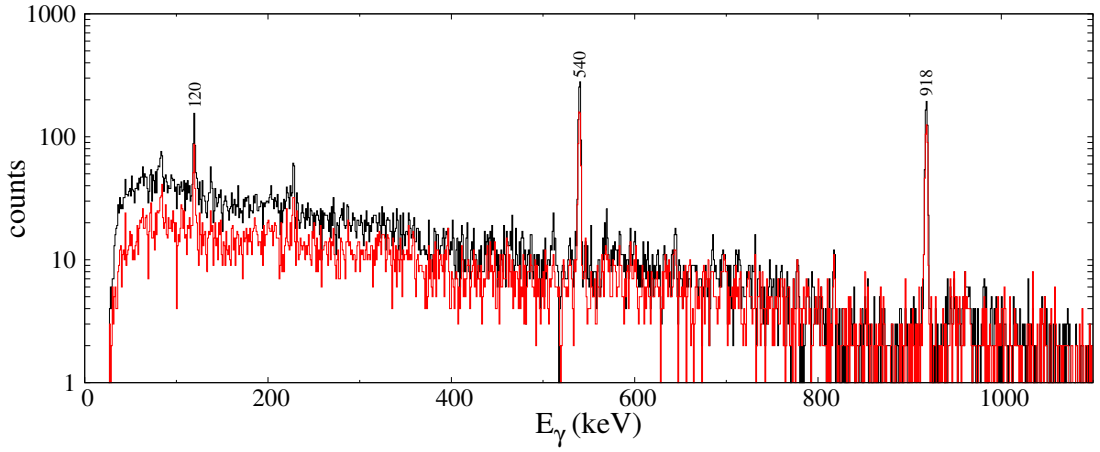

Figure 3.36: ^{211}*Rn energy spectrum when no add-back is applied (black) compared with the case in which add-back is applied to multiplicity 1,2 and 3 cases (red) when the events from the prompt flash are excluded from the time difference calculation.*

3.4.6.2 The effect of including multiplicity 4, 5, 6 and 7 cases in the add-back algorithm on transitions in ^{211}Rn

All the energy signals measured in multiplicity 4, 5, 6 or 7 cases were rejected in all add-back algorithms up to now. For the ^{212}Rn data set, they account for 15 % of the data. Fig. 3.37 compares the energy spectrum when no add-back is applied (black) with the following cases:

- Multiplicity 1, 2 and 3 cases separately when add-back is applied as explained in previous sections. These are labelled M1 to M3.

- Multiplicity 4, 5, 6 and 7 cases separately when no add-back is applied and all the energy signals are included as single gamma rays. These are labelled M4 to M7.
- Multiplicity 4, 5, 6 and 7 added together and all the energy signals are included as single gamma rays. This is labelled M4-M7.

The spectra for each of the multiplicity cases from 4 to 7, show that for a number of events, the gamma rays of interest are detected within the same cluster. The P/T ratios can be calculated again also including multiplicity cases higher than 3 treating the energy signals as single gamma rays. This is done in Fig. 3.38, which shows in red the energy spectrum when add-back is applied to multiplicity 1, 2 and 3 cases, and multiplicity 4, 5, 6 and 7 cases are treated as single gamma rays. Table 3.13 shows that the calculated P/T ratios and the number of counts in the photopeak decrease compared with the case in which no add-back is applied. A comparison between Tables 3.12 and 3.13 show that the effect of adding multiplicity 4, 5, 6, and 7 cases as single gamma rays decreases the P/T ratios and increases the number of counts in the photopeak. The overall picture is that in both cases, the quality of the energy spectrum does not improve applying add-back.

The results on the P/T ratios and the statistics associated with the gamma rays of interest for the in-beam ^{212}Rn data set present similarities to those from the ^{152}Eu source data. The most obvious difference between the results for the ^{60}Co and the ^{152}Eu/^{212}Rn data is the higher crystal multiplicity in the latter case, where 33 crystals fire in an event, compared with the 8 crystals in an event for the ^{60}Co data. Another in-beam setting centred around ^{98}Zr, which has a low crystal multiplicity was used to further investigate this effect.

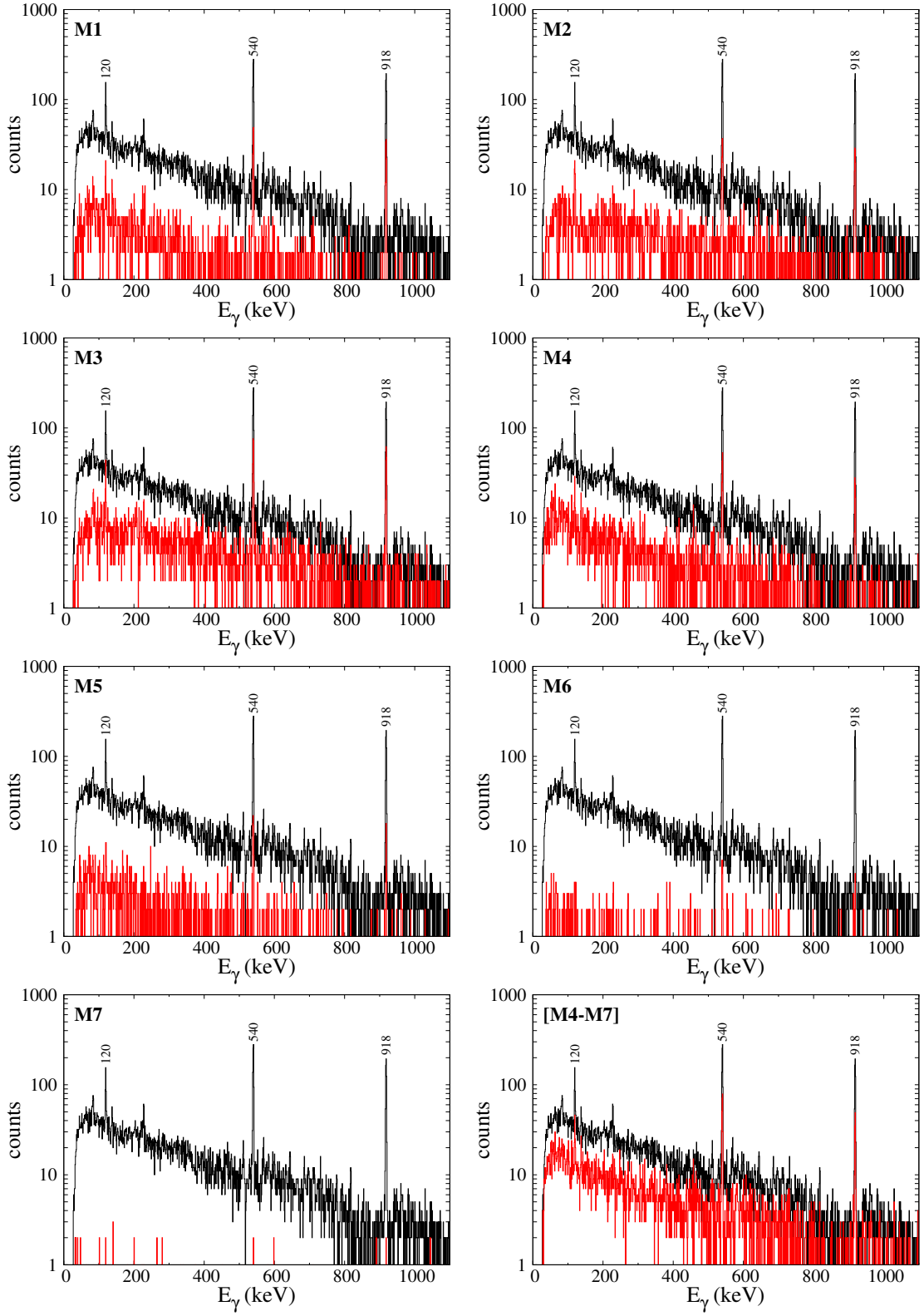

Figure 3.37: ^{211}*Rn energy spectrum when no add-back is applied (black), compared with the case in which add-back is applied for multiplicities 1, 2 and 3 separately, and not applied for multiplicity 4, 5, 6 and 7 cases (red). The labelled M4-M7 spectrum shows the effect of adding multiplicities 4 to 7 together as separate gamma rays.*

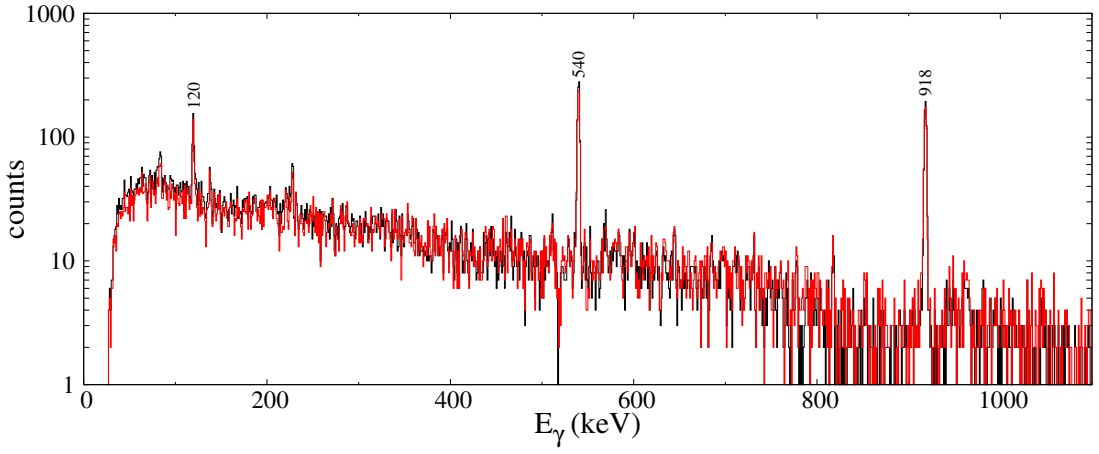

Figure 3.38: *^{211}Rn energy spectra when no add-back is applied (black), compared with the case in which add-back is applied to multiplicity 1, 2 and 3 cases and also including the energies from multiplicity cases higher than 4 as separate gamma rays (red).*

	No add-back		Add-back		
E (keV)	counts	P/T (%)	counts	P/T (%)	Improv. (%)
120	231	1.43	198	1.29	-9.8
540	765	4.73	697	4.55	-3.8
918	562	3.48	517	3.38	-2.9
total	16161		15317		

Table 3.13: *^{211}Rn peak-to-total ratios when no add-back is applied (***left***), compared with the case in which add-back is applied to multiplicities 1,2 and 3 and not applied for multiplicities 4, 5, 6 and 7; for events outside the prompt-flash (***right***). The last column shows the improvement in the P/T ratios.*

3.4.6.3 The effect of using add-back for multiplicity 1, 2 and 3 cases on transitions in ^{94}Y

Fig. 3.39 shows the cluster and crystal multiplicities, and the number of gamma rays in an event after applying add-back to multiplicity 1, 2 and 3 cases for the ^{98}Zr data set. Table 3.14 shows the cluster multiplicity probabilities, where 74.7% of the events are associated with multiplicity 1, 2 and 3 cases. An 1.35(2) μs isomeric decay in ^{94}Y which

Cluster multiplicity	1	2	3	4	5	6	7
^{98}Zr (%)	48.1	17.2	9.4	7.4	8.6	8.9	0.4

Table 3.14: *Cluster multiplicity probabilities for the ^{98}Zr setting.*

decays via three gamma rays with energies 432, 770 and 1202 keV, has been observed in this data set and used to test the add-back algorithms. The energy spectrum obtained as a result of applying add-back to multiplicity 1, 2 and 3 cases is compared to the case

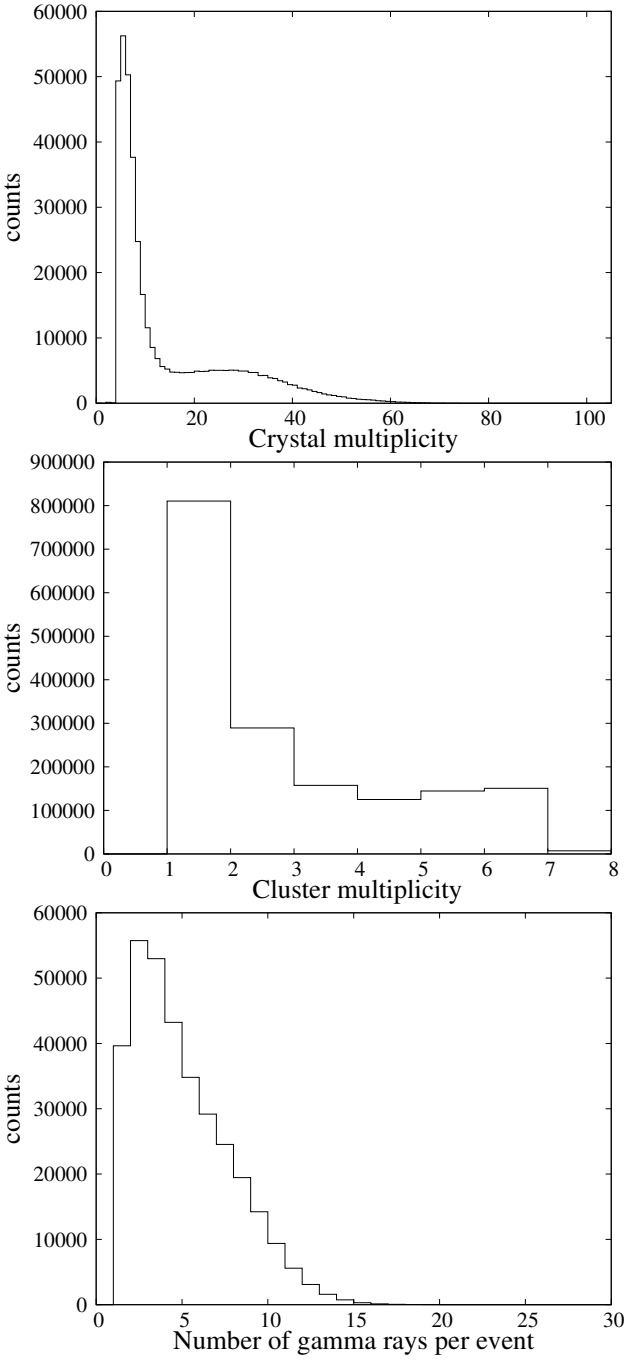

Figure 3.39: ***Upper:*** *crystal multiplicity* ***Middle:*** *cluster multiplicity* ***Lower:*** *number of gamma rays in each event after applying the add-back algorithms. The data corresponds to the* ^{98}Zr *data set. Note the different scales for the different plots.*

in which no add-back is applied in Fig. 3.40, and the calculated P/T ratios are shown Table 3.15.

The results show that the P/T ratio increases from 9.0 to 12.3% for the 432 keV transition, from 6.7 to 9.4 for the 770 keV and from 0.6 to 1.1 for the 1202 keV. In addition, the number of counts increases between 10 and 30%, in contrast with the results for the

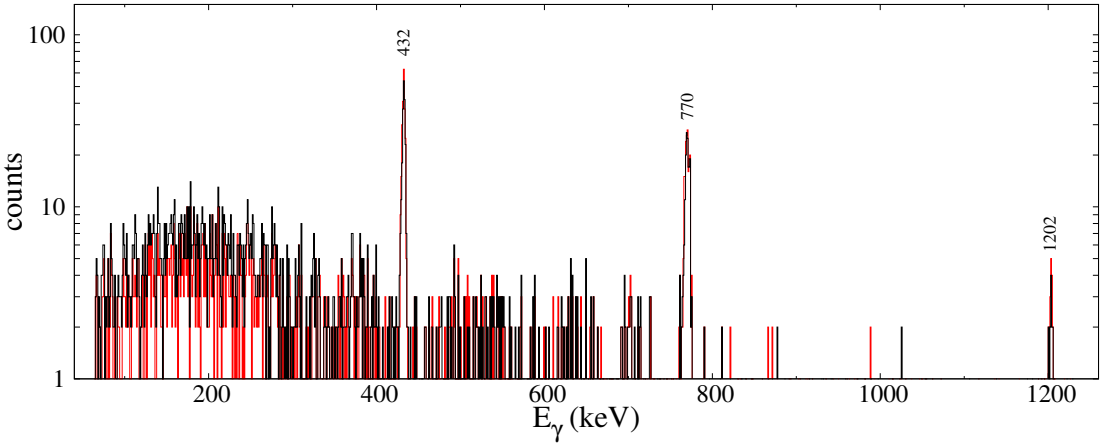

Figure 3.40: ^{94}*Y energy spectrum when add-back is not applied (black), compared with the case in which add-back is applied to multiplicity 1,2 and 3 cases (red).*

	No add-back		Add-back		
E (keV)	counts	P/T (%)	counts	P/T (%)	Improv. (%)
432	205	8.96	229	12.30	37
770	153	6.69	175	9.39	40
1202	15	0.65	21	1.12	72
total	2287		1863		

Table 3.15: ^{94}*Y P/T ratios when add-back is not applied (***left***, and when add-back is applied to multiplicity 1, 2 and 3 cases (***right***). The last column shows the improvement in the P/T ratio when add-back is applied.*

^{212}Rn data set. The P/T ratios obtained for the ^{212}Rn and ^{98}Zr data sets show that there is a correlation between the number of crystals that have fired in an event and the improvement in the P/T ratio and statistics in the spectrum. The add-back algorithm does not produce good results when the crystal multiplicity is larger, as in the case of the ^{212}Rn data set case. A possible solution would be to first analyse the data without using add-back, identify the gamma rays decaying from the nucleus of interest and then set up more restrictive energy conditions in the add-back algorithm. The data analysed in this thesis has crystal multiplicities of around 20 and therefore it has been decided that the add-back procedure would not have any benefit and thus has not been applied. All the energy signals detected in all the crystals are included in the energy spectra as separate gamma rays.

Chapter 4

Experimental results

The decay of high angular momentum states has been observed following ^{238}U projectile fragmentation. Previously reported isomeric states have been identified in ^{198,200,206,208}Po, ^{209,210,211,212}At, ^{210,211,212,213,214}Rn, ^{208,211,212,213,214}Fr, ^{210,211,212,214,215}Ra and ^{215}Ac. The results have been separated into two different sections, corresponding to the different stopper configurations. In Section 4.2 the results from the ^{212}Rn and ^{214}Th settings are presented, where the ions were stopped in the passive stopper. Section 4.1 contains information from the ^{213}Fr and ^{214}Ra settings, where the active stopper was present. In each section, the nuclei are discussed in order of increasing Z and increasing A.

The particle identification plots representing the position at the final plane S4 versus the A/Q ratio for each Z are presented for all settings. The delayed gamma-ray energy spectra are shown for each nucleus, and the time gate between implantation and gamma ray detection used in the analysis (typically of the order of six half-lives) is indicated. The gamma-ray transitions from the isomeric states are labelled as are the corresponding X-rays. The non-labelled energies correspond to background peaks from neighbouring nuclei. Where half-lives have been measured the data is shown together with the gamma-ray energy spectrum of the given isotope. The half-lives used for the calculations come from previously published information unless the measurement in this work has been obtained with a smaller error than the published data. The half-lives from the literature are taken from the evaluated nuclear data sheets [66].

For each isotope, the calculation of the isomeric ratios is dependent on the knowledge of the level scheme and the transition multipolarities. The quoted value is the weighted mean calculated for different transitions. When the isomeric ratio is calculated for a lower lying isomeric state, it is implicit unless otherwise mentioned, that the feeding from any higher-lying isomeric states has been subtracted.

The survival of isomers with half-lives shorter than the ∼300 ns flight time through the FRS depends on the suppression of electron conversion for highly stripped ions. When the isomeric state depopulates by a low energy transition, the electron conversion coefficient is large, making its effective half-life longer than that in the neutral atom. For fully stripped ions the total conversion coefficient is used to calculate the in-flight losses correction factor of the isomeric ratio. However, for H-like and He-like ions, the electron conversion process is not completely suppressed and in this case it has been assumed that the electron lies in the lowest energy orbital, the $1s$ K-shell. The electron conversion coefficient for the K-shell is therefore used for the not fully stripped ions. The details of the calculation of isomeric ratios was discussed in Section 1.3.

As shown in Eq: 1.12, the calculation of the isomeric ratios includes two correction factors. The correction factor F, defined in Eq: 1.14, accounts for the survival of the ions through the FRS and it depends on the transition directly depopulating the isomer. Therefore it is constant for all the gamma rays of the decay path for a given isomeric state. The correction factor G, defined in Eq: 1.15, accounts for the losses in the number of counts in the photo peak due to the time gate used in the delayed gamma-ray energy-time matrix. This value is gamma-ray energy dependent because of the different starting points in the time gate due to the prompt-flash.

4.1 Results from the settings using the active stopper data

Fig. 4.1 shows the isotopes of radon (Z=86), francium (Z=87) and radium (Z=88) identified in the ^{213}Fr data set (upper panels) and ^{214}Ra data set (lower panel). The ^{212}Fr isotope has been implanted in both settings and the isomeric ratios have been calculated independently for both sets of data. The other isotopes have been identified in only one of the data sets.

4.1.1 ^{210}Rn

Isomeric states in ^{210}Rn have been previously studied in [67, 68, 69, 70]. The measured delayed gamma-ray spectrum and partial level scheme are shown in Figs. 4.2 and 4.3 respectively. The observed isomers are a low spin 8^+ isomer at x + 1665 keV, with a half-life of 644(40) ns and gamma-ray de-excitation energies of 120, 203, 644, 818 and 901 keV; and a higher-lying isomer at 3812 + X keV with a half-life of 1.06(5) μs and spin and parity $(17)^-$. A third 76(7) ns isomeric state with spin and parity $(14)^+$ has been indicated in the level scheme. A 325 keV transition depopulates this isomer, with an internal conversion coefficient of 0.110(1). This transition is not highly converted and

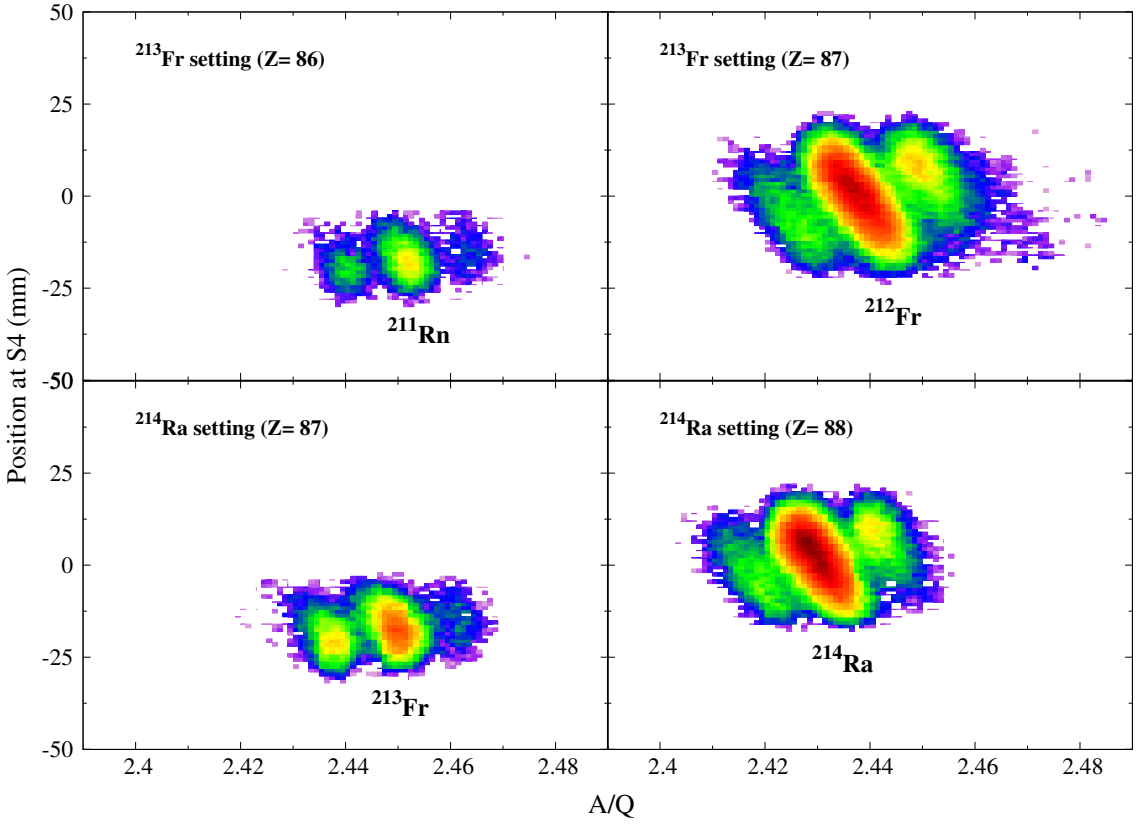

Figure 4.1: *Particle identification plots for the ^{213}Fr (upper panels) and ^{214}Ra (lower panels) settings. Each panel corresponds to the position versus A/Q ratio gated only on the indicated Z.*

therefore the isomer decays as it travel through the FRS, and it is not expected to be implanted in this state.

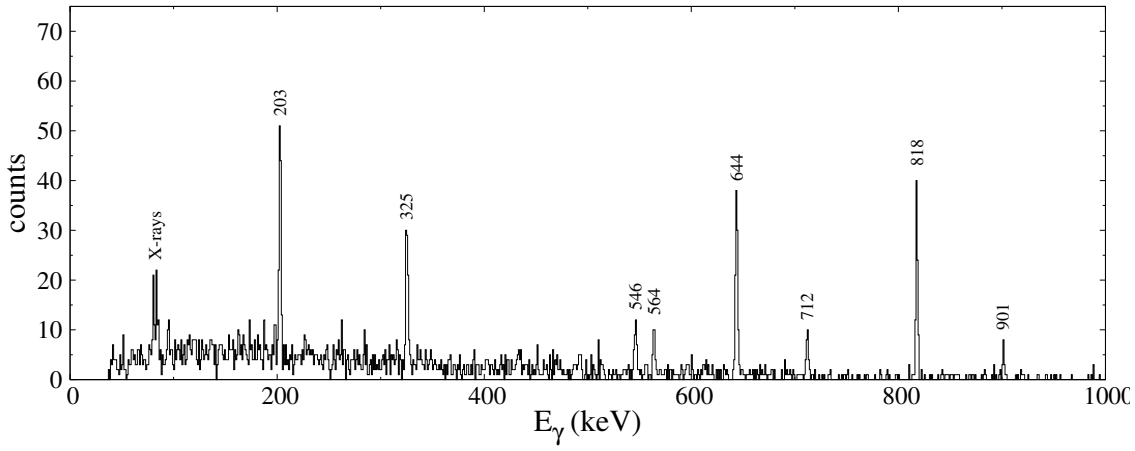

Figure 4.2: *The gamma-ray spectrum observed in coincidence with ^{210}Rn ions from the ^{213}Fr data set. A time gate of 6.7 µs has been used.*

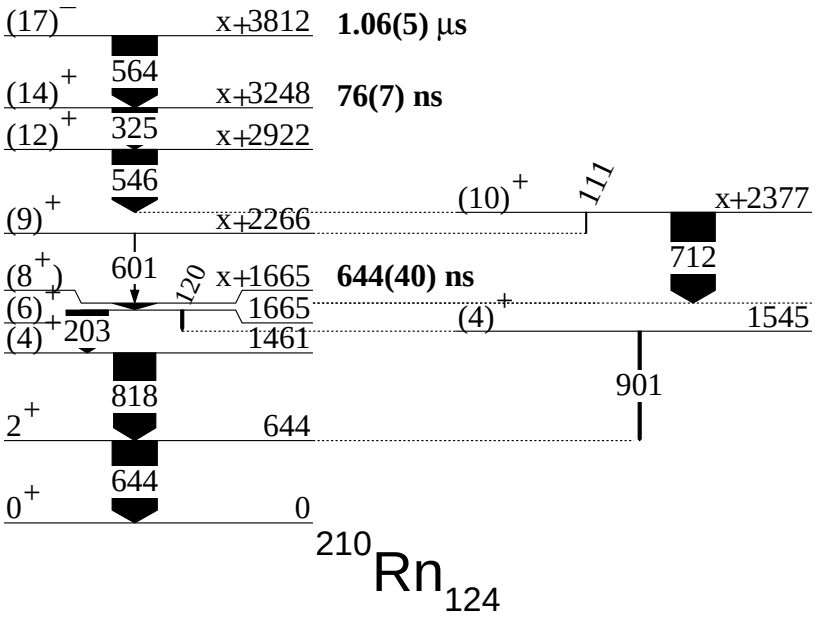

Figure 4.3: *A partial level scheme of ^{210}Rn. The width of the arrows is proportional to the total intensity of the different decay branches.*

Table 4.1 shows the relevant information for the calculation of the isomeric ratios, listing the energy of gamma-rays depopulating each isomer, its multipolarity, electron conversion coefficient, relative gamma-ray intensity, branching ratio, and the correction factor for in-flight decay losses (F) and finite gamma-ray detection time (G). The isomeric ratio of the $(17)^-$ isomeric state has been calculated for the 564, 325, 546 and 712 keV transitions. The isomeric ratio for the 325 keV transition is larger than that of the other transitions. The energy spectrum in Fig. 4.2 shows the larger gamma-ray intensity of the 325 keV transition compared with the 546 and 564 keV transitions which are part of the same cascade. This is thought to be due to background contamination from the 327 and 328 keV transitions in ^{211}Fr and ^{212}Fr respectively. Due to the low statistics, there is not enough evidence of the 111 keV transition to obtain information of the branching ratio of the level, therefore the relative gamma-ray intensities from [71] have been used. The isomeric ratio for the $(17)^-$ isomer is 11(2)%, calculated as the weighted mean isomeric ratio from the other three transitions (excluding the 325 keV transition). The (8^+) isomeric state depopulates via an unobserved low-energy transition, thought to be <50 keV [71]. A 49 keV transition has been assumed to obtain the conversion conversion coefficient and calculate the correction factor F. A weighted mean isomeric ratio of 29(3)% has been obtained for the (8^+) isomer, using the 203, 901, 818, and 644 keV transitions.

I^π	E_γ(keV)	M	α [72, 73]	I_γ	b	F	G	R_{exp}(%)
$(17)^-$	564	E3	0.0851(12)	164(41)	1.00	0.896(5)	0.94(2)	10(3)
	325	E2	0.11(1)	345(54)	1.00	0.895(5)	0.92(2)	22(4)
	546	E2	0.0287(4)	180(40)	1.00	0.895(5)	0.94(2)	11(2)
	712	E2	0.01602(23)	175(40)	0.81	0.895(5)	0.96(2)	12(3)
(8^+)	<50	(E2)	>245(4)		1.00			
	203	E2	0.495(7)	383(46)	0.81	0.999	0.80(2)	29(5)
	901	E2	0.00995(14)	140(38)	0.19	0.999	0.97(3)	26(10)
	818	E2	0.01208(17)	708(81)	0.81	0.999	0.97(3)	33(5)
	644	E2	0.0199(3)	722(85)	1.00	0.999	0.95(2)	26(5)

Table 4.1: *Relevant information for the calculation of the isomeric ratios of the $(17)^-$ and (8^+) isomeric states in ^{210}Rn. The number of implanted ions was 2077.*

4.1.2 ^{211}Rn

Isomeric states in ^{211}Rn have been previously studied in [74, 75]. The delayed gamma-ray spectrum and partial level scheme are shown in Figs. 4.4 and 4.5 respectively. An isomeric state at an excitation energy of x + 3926 keV and spin and parity $(35/2^+)$, and a half-life of 40.2(14) ns has been observed. Another isomer has been observed at an excitation energy of x + 1578 keV, with spin and parity $(17/2^-)$ and a half-life of 596(28) ns. A single unobserved low-energy transition, assumed in [74] to be an E2 transition with an energy lower than 50 keV, depopulates this isomeric state. In this case, the electron conversion coefficient is $\geq$245, and this is the value that has been used to obtain the in-flight decay constant for the correction factor. In addition to the the ^{211}Rn transitions, the energy

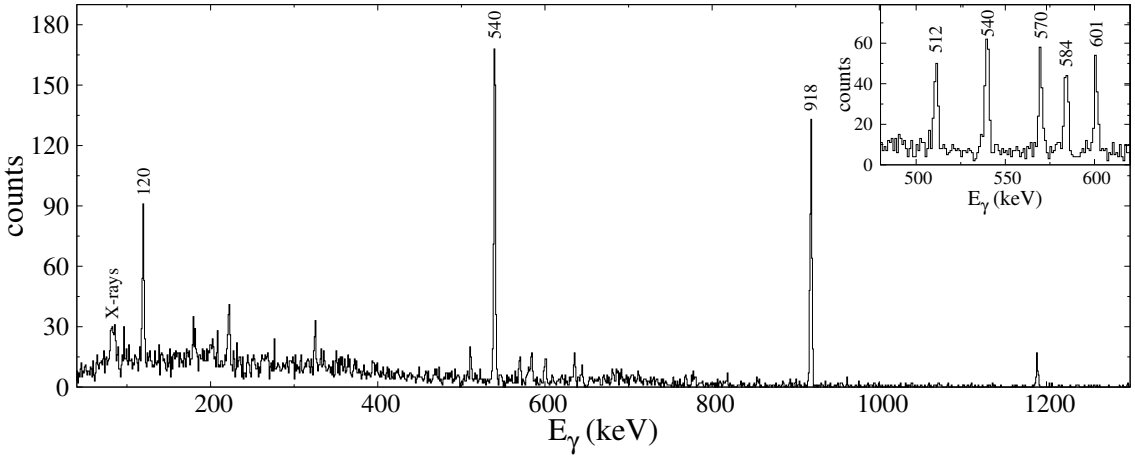

Figure 4.4: *The gamma-ray spectrum observed in coincidence with ^{211}Rn ions from the ^{213}Fr data set. Time gates of 7.6 μs and 450 ns have been used for the main and inset plots respectively.*

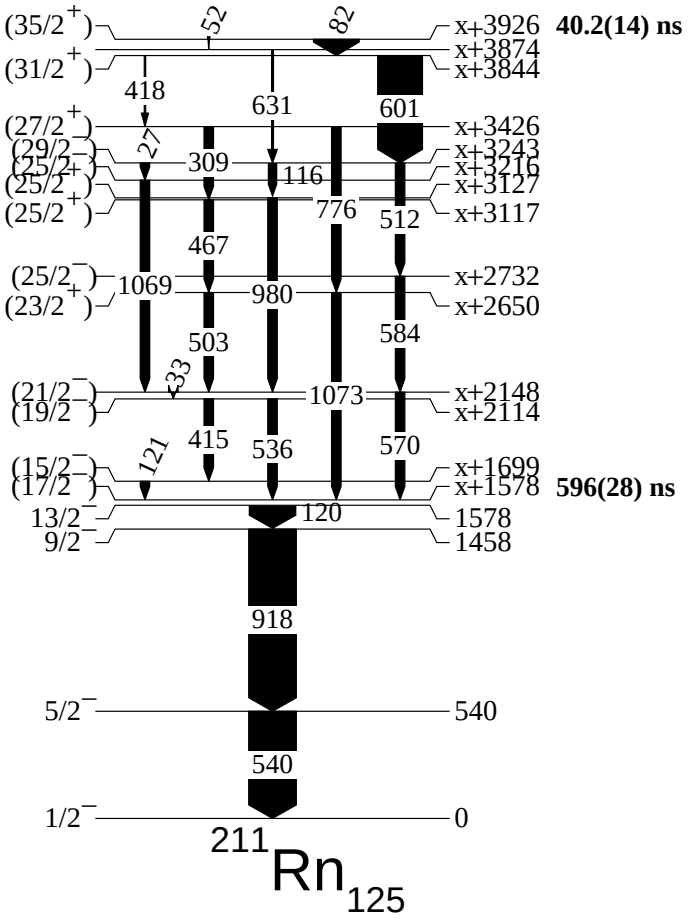

Figure 4.5: *A partial level scheme of* ^{211}*Rn. The width of the arrows is proportional to the total intensity of the different decay branches.*

spectrum in Fig. 4.4 shows peaks at 179, 222 and 1189 keV from the cascade of a low isomeric state in ^{213}Fr and also at 203, 818 and 644 keV from ^{210}Rn.

I^{π}	E_{γ}(keV)	M	α [72, 73]	I_{γ}	b	F	G	R_{exp} (%)
$(35/2^{+})$	(52)	(M1)	17.21(24)		0.04			
	82	(E2)	20.9(4)		0.96			
	601	E1	0.00761(11)	669(88)	0.94	0.865(2)	1.0(4)	13(6)
	512	E2	0.0333(5)	646(79)	0.91	0.865(2)	1.0(4)	14(6)
	584	E2	0.0246(4)	649(86)	0.91	0.865(2)	1.0(4)	14(6)
	570	E2	0.0260(4)	632(85)	0.82	0.865(2)	1.0(4)	15(7)
$(17/2^{-})$	(<50)	(E2)	>245		1.00			
	120	E2	3.88(6)	518(60)	1.00	0.999(2)	0.70(2)	43(8)
	540	E2	0.0294(5)	2697(173)	1.00	0.999(2)	0.92(3)	35(4)
	918	E2	0.00959(14)	3144(203)	1.00	0.999(2)	0.94(3)	40(5)

Table 4.2: *Relevant information for the calculation of the isomeric ratios of the* $(35/2^{+})$ *and* $(17/2^{-})$ *isomeric states in* ^{211}*Rn. The number of implanted ions was 6255.*

Table 4.2 shows the relevant information for the calculation of the isomeric ratios. From

the experimental results, an isomeric ratio of 14(3)% for the $I^{\pi} = (35/2^{+})$ isomer and a weighted mean isomeric ratio of 38(3)% from the 120, 540 and 918 keV transitions for the $I^{\pi} = (17/2^{-})$ isomer have been obtained.

4.1.3 ^{211}Fr

Isomeric states in ^{211}Fr have been previously studied in [76]. The delayed gamma-ray spectrum and partial level scheme are shown in Figs. 4.6 and 4.7 respectively. Two isomeric states at excitation energies of 4657 and 2423 keV have been observed in this experiment. The higher-lying isomer has a spin and parity of $(45/2^{-})$ and a half-life of 123(14) ns; and the lower-lying isomer has a spin and parity of $(29/2^{+})$ and a half-life of 146(14) ns. An attempt to measure the half-lives with the data from this experiment was made, but there is not sufficient statistics to obtain a value for the high spin isomer, and therefore the feeding to the lower spin isomer cannot be calculated. Nevertheless, the half-life of the lower spin isomer has been estimated and is confirmed as the same order of magnitude as the published value. The result is shown in the inner plot in Fig. 4.6. A half-life of 130(9) ns has been obtained for the lower isomer, compared to the 146(14) ns published value. The half-lives from the literature have been used for the calculation of the isomeric ratios since the measured value from this data has not taken into account the feeding from the isomer above.

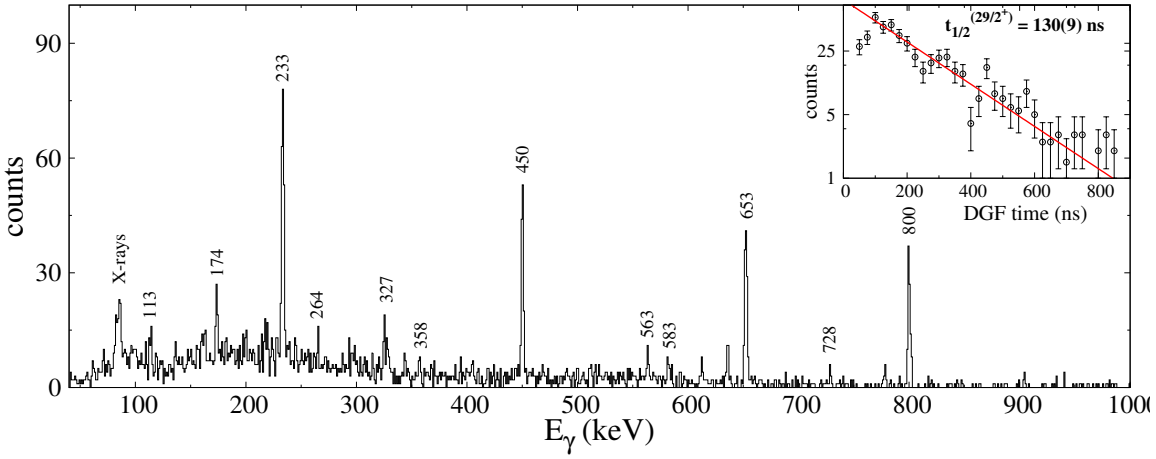

Figure 4.6: *The gamma-ray spectrum observed in coincidence with ^{211}Fr ions from the ^{213}Fr data set. A time gate of 1.8 μs has been used and the measured half-life of the $I^{\pi} = (29/2^{+})$ isomeric state is shown in the inner figure.*

Table 4.3 shows the relevant information for the calculation of the isomeric ratios. The branching ratios have been obtained from the relative gamma-ray intensities given in [76].

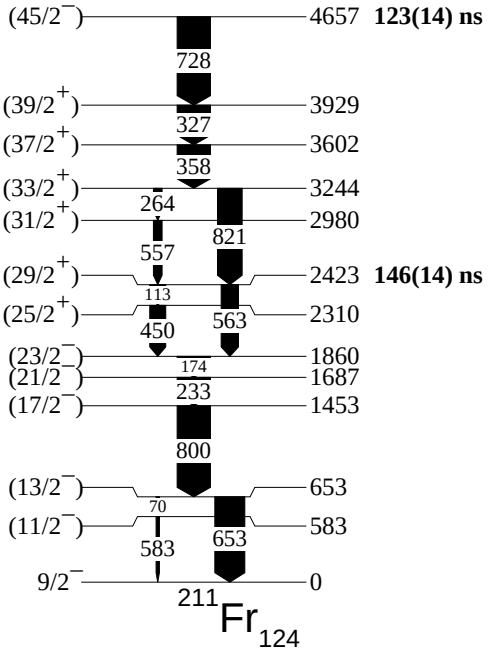

Figure 4.7: *A partial level scheme of ^{211}Fr. The width of the arrows is proportional to the total intensity of the different decay branches.*

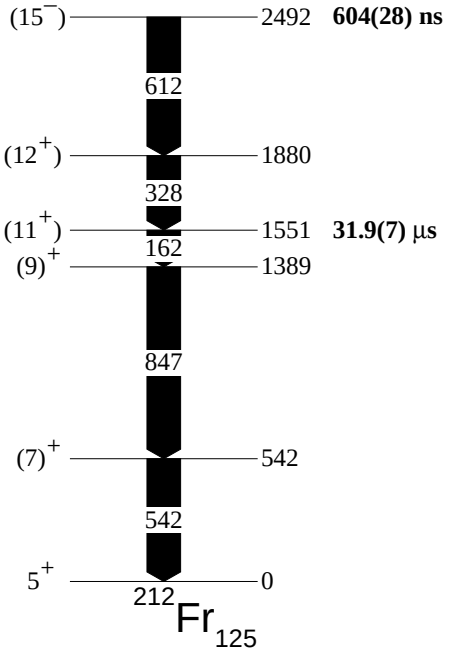

Figure 4.8: *A partial level scheme of ^{212}Fr. The width of the arrows is proportional to the total intensity of the different decay branches.*

Isomer I^π	E_γ(keV)	M	α [72, 73]	I_γ	b	F	G	R_{exp}
$(45/2^-)$	728	E3	0.0444(7)	66(33)	1.00	0.37(4)	0.75(11)	3.2(4)
	327	M1(+E2)	0.41(13)	78(29)	1.00	0.37(4)	0.66(10)	5.9(6)
	358	(E2)	0.0871(13)	41(26)	1.00	0.37(4)	0.66(10)	2.4(4)
	264	(M1+E2)	0.6(3)	30(26)	0.84	0.37(4)	0.66(10)	3.1(6)
$(29/2^+)$	113	(E2)	5.32(8)	103(39)	0.87	0.798(9)	0.79(9)	12(6)
	563	(E3)	0.0907(13)	104(42)	0.13	0.80(9)	0.79(10)	14(7)
	450	(E1)	0.01414(2)	747(81)	0.87	0.80(9)	0.79(10)	15(3)
	174	M1	2.98(5)	106(42)	1.00	0.80(9)	0.44(6)	12(7)
	233	E2	0.323(5)	747(76)	1.00	0.80(9)	0.62(8)	22(4)
	800	E2	0.01325(19)	831(91)	1.00	0.80(9)	0.79(10)	14(3)
	653	E2	0.0202(3)	862(88)	0.90	0.80(9)	0.79(10)	17(3)
	583	M1+E2	0.074(17)	78(35)	0.90	0.80(9)	0.79(10)	14(8)

Table 4.3: *Relevant information for the calculation of the isomeric ratios of the $(45/2^-)$ and $(29/2^+)$ isomeric states in ^{211}Fr. The number of implanted ions was 7700.*

The isomeric ratio calculated for the 327 keV transition is larger than those for the other gamma-ray decays for the high spin isomeric state. This is due to the contamination from the 325 keV transition in ^{210}Rn, as discussed in Section: 4.1.1. Thus, this transition has not been considered and the isomeric ratio for the $I^\pi = (45/2^-)$, calculated as the weighted mean from the 728, 358 and 264 keV transitions, was found to be 2.4(2)%. An isomeric ratio of 16(1)% for the $I^\pi = (29/2^+)$ isomer has been obtained, calculated as the weighted mean from the isomeric ratios of the 563, 450, 174, 233, 800, 653 and 583 keV

transitions.

4.1.4 ^{212}Fr

Isomeric states in ^{212}Fr have been previously studied in [76, 77, 78]. The partial level scheme and delayed gamma-ray spectrum are shown in Figs. 4.8 and 4.9 respectively. The gamma-ray spectra in Fig. 4.9 are the combination of data from the ^{213}Fr and ^{214}Ra data sets. Time gates of 5.1 μs and 97 μs have been used to produce the upper and lower spectra of Fig. 4.9 respectively, and for each case, the gamma-rays from the decay of the corresponding isomer are marked in black. Two isomeric states at excitation energies of 2492 and 1551 keV have been observed in this experiment. The higher-lying isomer has a spin and parity of (15^-) and a half-life of 604(28) ns; and the lower-lying isomer has a spin and parity of (11^+) and a half-life of 31.9(7) μs [78]. Half-lives of 577(19) ns and 26.1(9) μs have been measured in this experiment (see inner plots in Fig. 4.9). There is a difference in the intensities of the gamma rays observed in the two different settings, as shown in Fig. 4.10. This is thought to be due to the different implantation depths in the active stopper for the two settings, which would slightly modify the efficiencies of gamma-ray detection. Therefore the calculation of the isomeric ratio has been done for each case separately.

Tables 4.4 and 4.5 show the relevant information for the calculation of the isomeric ratios for the ^{213}Fr and ^{214}Ra settings respectively. The isomeric ratio of the $I^\pi = (15^-)$ isomer is 16(1)% for the ^{213}Fr data set, while it increases to 22(1)% for the ^{214}Ra setting, which agree within three standard deviations. Isomeric ratios of 23(3)% for the ^{213}Fr setting and 20(2)% for the ^{214}Ra setting have been found for the $I^\pi = (11^+)$ isomeric state.

I^π	E_γ(keV)	M	α [72, 73]	I_γ	b	F	G	R_{exp} (%)
(15^-)	612	E3	0.0711(1)	785(83)	1.00	0.815(5)	0.94(3)	15(2)
	328	(M1)	0.508(8)	574(60)	1.00	0.815(5)	0.90(3)	16(2)
(11^+)	162	(E2)	1.21(4)	1131(104)	1.00	0.998	0.874(1)	24(4)
	847	E2	0.01182(17)	2818(190)	1.00	0.998	0.878(1)	30(3)
	542	E2	0.0305(5)	2100(141)	1.00	0.998	0.878(1)	19(3)

Table 4.4: *Relevant information for the calculation of the isomeric ratios of the (15^-) and (11^+) isomeric states in ^{212}Fr from the ^{213}Fr setting. The number of implanted ions was 7158.*

4.1.5 ^{213}Fr

Isomeric states in ^{213}Fr have been previously studied in [76, 79]. The delayed gamma-ray spectrum and partial level scheme are shown in Figs. 4.11 and 4.12 respectively. A time

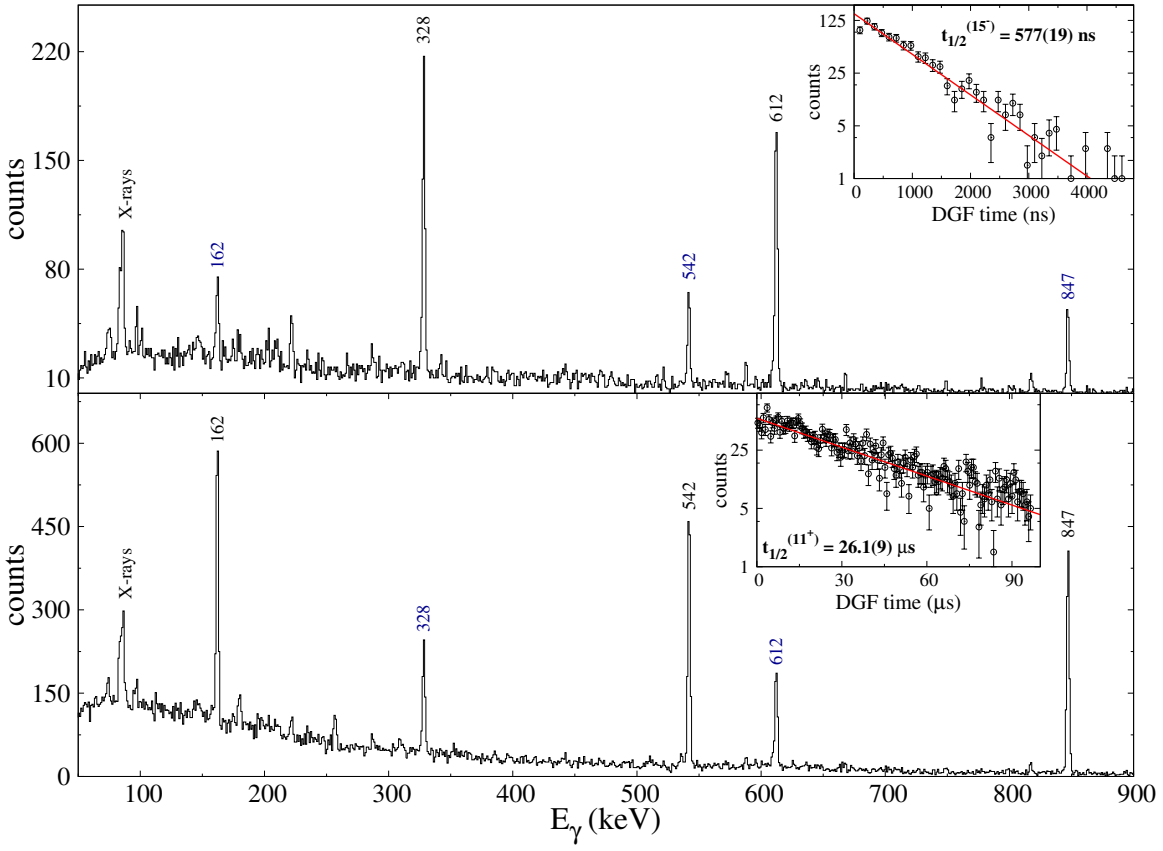

Figure 4.9: *The gamma-ray spectrum observed in coincidence with ^{212}Fr ions from the ^{213}Fr and ^{214}Ra data sets combined into a single spectrum.Time gates of 5.1 and 97 µs have been used to produce the upper and lower spectra of the figure respectively. The measured half-lives of the lower and higher-lying isomers are shown in the inner plots of the upper and lower panels respectively.*

I^π	E_γ(keV)	M	α [72, 73]	I_γ	b	F	G	R_{exp} (%)
(15^-)	612	E3	0.0711(1)	2640(166)	1.00	0.815(5)	0.94(3)	22(2)
	328	(M1)	0.508(8)	1768(124)	1.00	0.815(5)	0.90(3)	22(2)
(11^+)	162	(E2)	1.21(4)	2870(181)	1.00	0.998	0.874(1)	22(3)
	847	E2	0.01182(17)	6422(326)	1.00	0.998	0.878(1)	23(3)
	542	E2	0.0305(5)	5579(279)	1.00	0.998	0.878(1)	18(2)

Table 4.5: *Relevant information for the calculation of the isomeric ratios of the (15^-) and (11^+) isomeric states in ^{212}Fr from the ^{214}Ra setting. The number of implanted ions was 16410.*

gate of 4.6 μs has been used to produce the energy spectrum. Two isomeric states at excitation energies of 2538 and 1590 keV have been observed in this experiment. The higher-lying isomer has a spin and parity of $29/2^+$ and a half-life of 238(6) ns; and the lower-lying isomer has a spin and parity of $21/2^-$ and a half-life of 505(14) ns. Half-lives of 234(10) ns and 584(11) ns respectively have been measured in this experiment (see

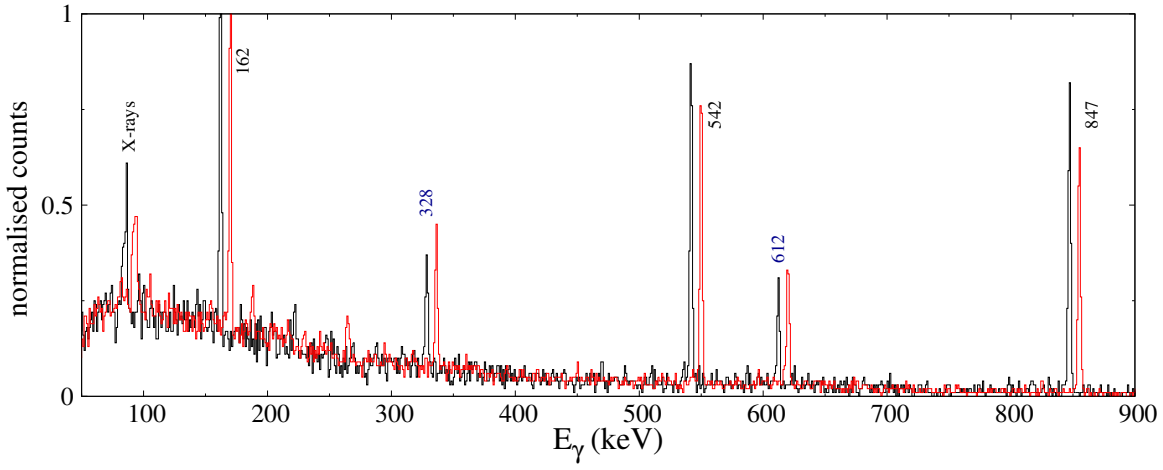

Figure 4.10: *The gamma-ray spectrum observed in coincidence with ^{212}Fr ions from the ^{213}Fr (black) and ^{214}Ra (red) data sets. A time gate of 97 µs has been used to produce the spectra. The red spectrum has been shifted by 10 keV with respect to the black spectrum in order to help the comparison of both spectra.*

inner figures in Fig. 4.11), in good agreement with the previous work.

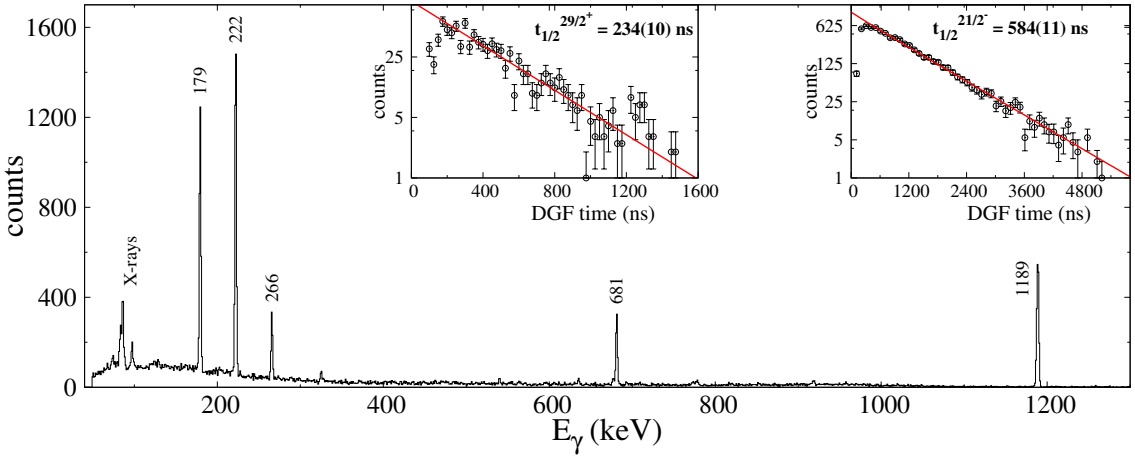

Figure 4.11: *The gamma-ray spectrum observed in coincidence with ^{213}Fr ions from the ^{213}Fr data set. A time gate of 4.6 µs has been used and the inner plots show the half-lives measured for both isomers.*

Table 4.6 shows the relevant information for the calculation of the isomeric ratios. An isomeric ratio of 23(2)% for the $I^\pi = 29/2^+$ level has been obtained from the weighted mean of the isomeric ratios from the 681 and 266 keV transitions. The isomeric ratio for the $I^\pi = 21/2^-$ isomeric state is 22(2)%, calculated as the weighted mean from the isomeric ratios of the 179, 222 and 1189 keV transitions.

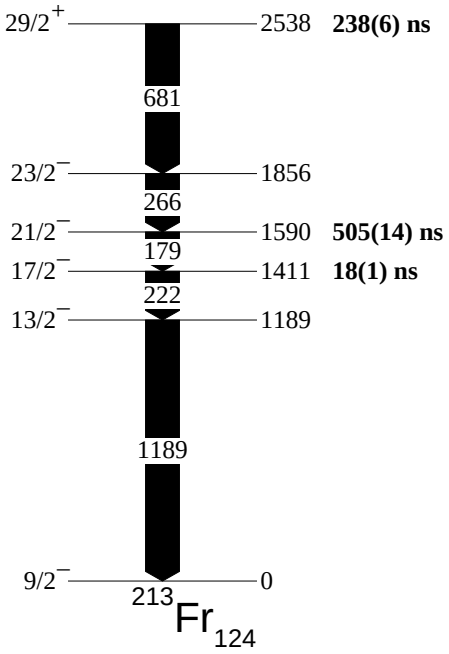

Figure 4.12: *A partial level scheme of ^{213}Fr. The width of the arrows is proportional to the total intensity of the different decay branches.*

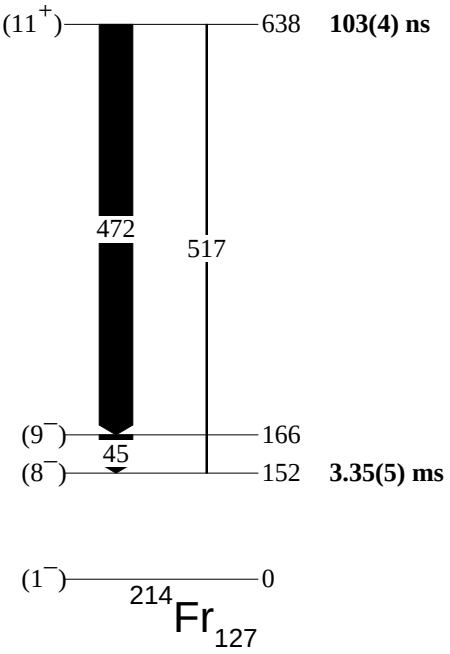

Figure 4.13: *A partial level scheme of ^{214}Fr. The width of the arrows is proportional to the total intensity of the different decay branches.*

I^π	E_γ(keV)	M	α [72, 73]	I_γ	b	F	G	R_{exp} (%)
$29/2^+$	681	E3	0.0529(8)	5360(362)	1.00	0.60(1)	0.80(6)	23(2)
	266	M1+E2	0.6(4)	2721(285)	1.00	0.60(1)	0.69(5)	21(6)
$21/2^-$	179	E2	0.823(12)	9103(429)	1.00	0.887(2)	0.77(2)	22(3)
	222	E2	0.382(6)	12644(467)	1.00	0.887(2)	0.812(2)	22(3)
	1189	E2	0.00616(9)	19139(757)	1.00	0.887(2)	0.92(3)	22(3)

Table 4.6: *Relevant information for the calculation of the isomeric ratios of the $29/2^+$ and $21/2^-$ isomeric states in ^{213}Fr. The number of implanted ions was 50526.*

4.1.6 ^{214}Fr

Isomeric states in ^{214}Fr have been previously studied in [80, 81]. The level scheme and delayed gamma-ray spectrum are shown in Figs. 4.13 and 4.14 respectively. A time gate of 1 μs has been used to produce the energy spectrum. An isomeric state at an excitation energy of 638 keV has been observed in this experiment, with spin and parity (11^+) and a half-life of 103(4) ns. A half-life of 96(14) ns has been measured in this experiment. A second isomer with a half-life of 3.35(5) ms has not been observed because it is too long lived for the time window of the data acquisition.

Table 4.7 shows the relevant information for the calculation of the isomeric ratio. An isomeric ratio of 70(14)% for the $I^\pi = (11^+)$ level has been obtained from the 472 keV transition.

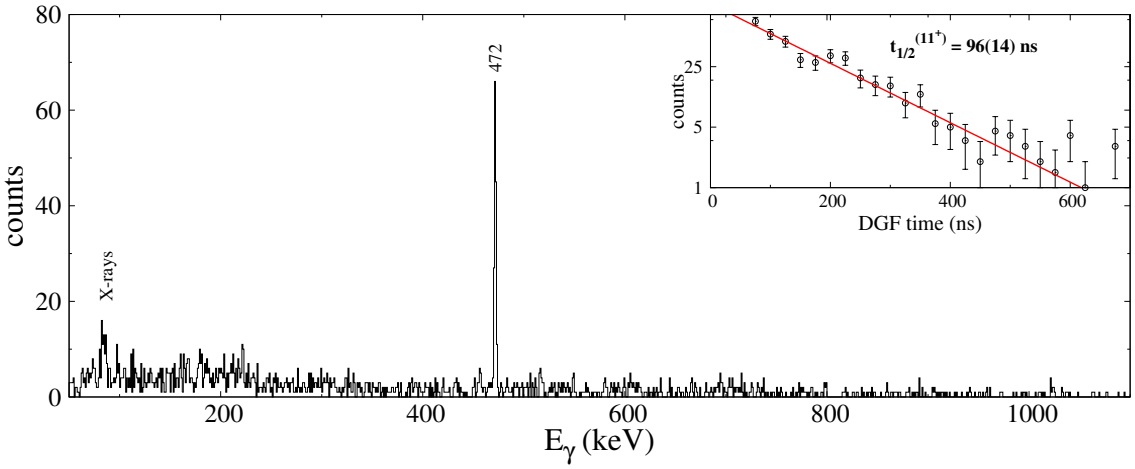

Figure 4.14: *The gamma-ray spectrum observed in coincidence with ^{214}Fr ions from the ^{214}Ra data set. A time gate of 1 μs has been used to produce the spectrum.*

I^π	E_γ(keV)	M	α [72, 73]	I_γ	b	F	G	R_{exp} (%)
(11^+)	472	M2	0.547(8)	1079(91)	0.98	0.35(1)	0.71(12)	70(14)

Table 4.7: *Relevant information for the calculation of the isomeric ratio of the (11^+) isomeric state in ^{214}Fr. The number of implanted ions was 9832.*

4.1.7 ^{214}Ra

Isomeric states in ^{214}Ra have been previously studied in [82, 83, 84, 85, 86]. The delayed gamma-ray spectrum and partial level scheme are shown in Figs. 4.15 and 4.16 respectively. Time gates of 3.6 μs and 95.8 μs have been used to produce the upper and lower spectra in Fig. 4.15 respectively. Four isomeric states at excitation energies of 4147, 3478, 2683 and 1865 keV have been observed in this experiment. The higher-lying isomer has a spin and parity of 17^- and a half-life of 225(4) ns; the following isomer has a spin and parity of 14^+ and half-life of 279(4) ns; the next one has a spin and parity of 11^- and a half-life of 295(7) ns; and the lower-lying isomer has a spin and parity of 8^+ and a half-life of 67.3(15) μs.

Table 4.8 shows the relevant information for the calculation of the isomeric ratios. Isomeric ratios of 13(1)%, 13(1)% and 64(2)% for the $I^\pi = 17^-$, 14^+ and 8^+ isomeric states respectively have been obtained. The time gate used to calculate the lower-lying isomeric ratio starts at 8.3 μs to avoid any feeding from the shorter isomers above. The isomeric ratio of the $I^\pi = 11^-$ state has not been calculated due to the difficulties in eliminating the feeding from two higher-lying isomers.

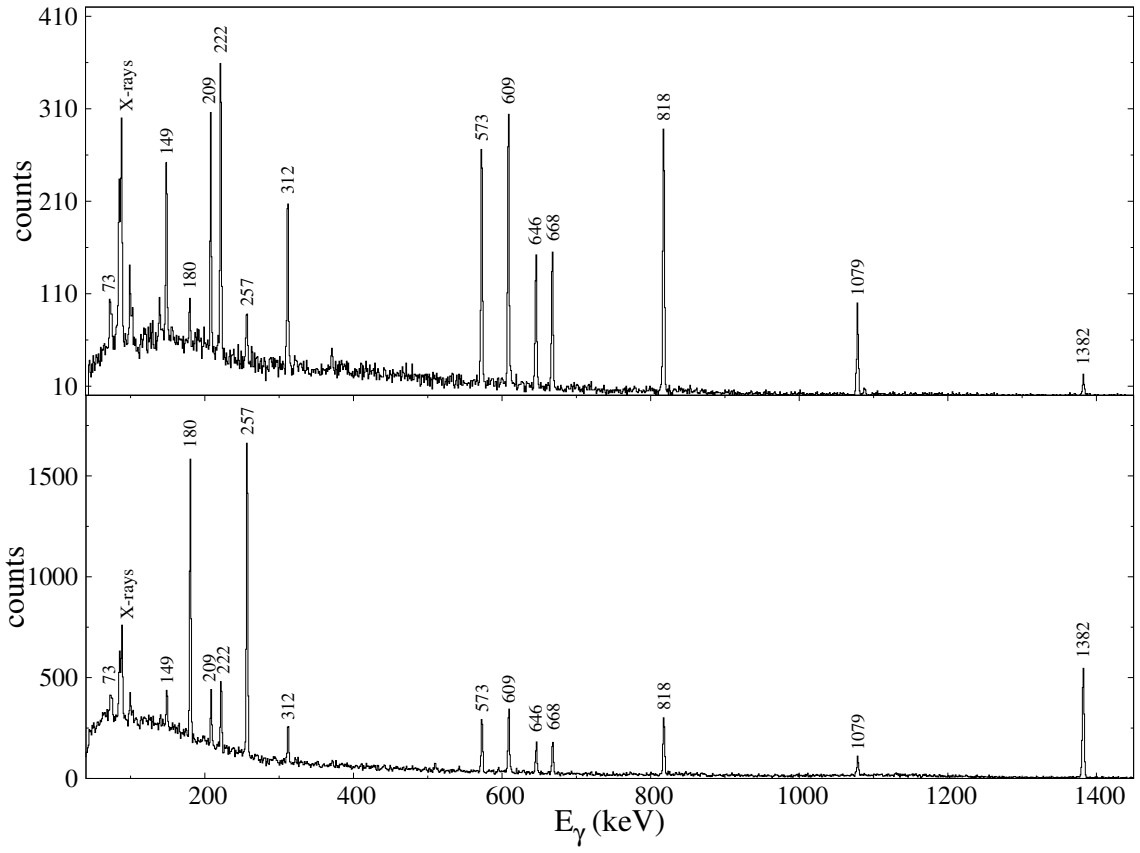

Figure 4.15: *The gamma-ray spectrum observed in coincidence with ^{214}Ra ions from the ^{214}Ra data set. Time gates of 3.6 μs and 95.8 μs have been used to produce the upper and lower spectra respectively.*

I^π	E_γ(keV)	M	α [72, 73]	I_γ	b	F	G	R_{exp} (%)
17^-	668	E3	0.0591(9)	2900(185)	0.89	0.606(5)	0.86(7)	13(1)
14^+	222	E2	0.382(6)	2863(156)	0.43	0.792(2)	0.69(4)	15(2)
	149	E2	1.69(24)	1499(177)	0.57	0.792(2)	0.54(3)	13(4)
	646	E1	0.00712(5)	2819(207)	0.26	0.792(2)	0.88(6)	14(3)
	312	E2	0.1348(3)	2198(170)	0.27	0.792(2)	0.73(5)	12(3)
	573	E1	0.00898(13)	4752(254)	0.47	0.792(2)	0.88(6)	12(2)
	1079	E2	0.00779(2)	2764(199)	0.27	0.792(2)	0.94(6)	11(2)
8^+	46	E2	414(8)		1.00			
	180	E2	0.863(22)	9441(406)	1.00	1	0.545(2)	63(3)
	257	E2	0.247(5)	14143(518)	1.00	1	0.545(2)	63(2)
	1382	E2	0.00493	18114(740)	1.00	1	0.545(2)	65(3)

Table 4.8: *Relevant information for the calculation of the isomeric ratios of the 17^-, 14^+ and 8^+ isomeric states in ^{214}Ra. The number of implanted ions was 51253.*

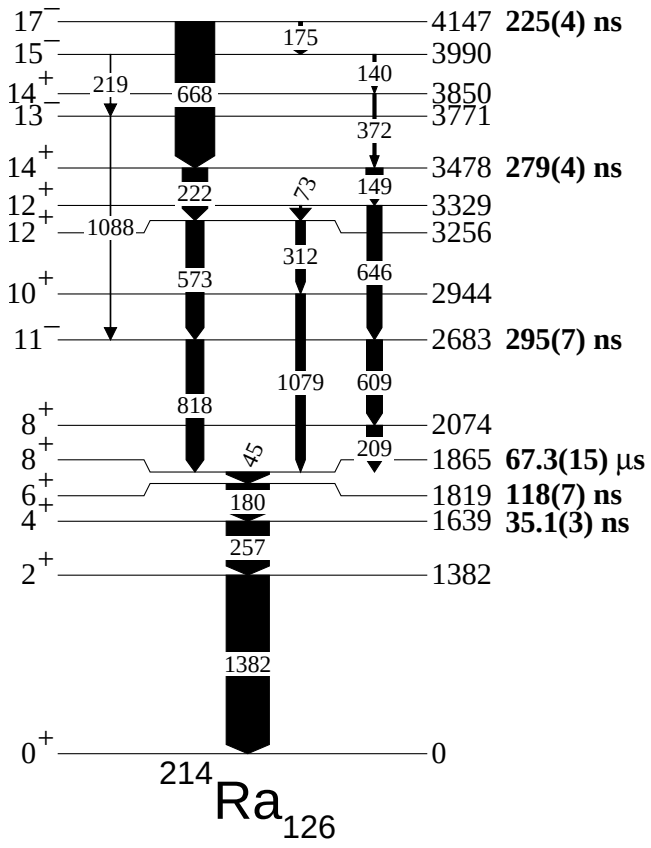

Figure 4.16: *A partial level scheme of ^{214}Ra. The width of the arrows is proportional to the total intensity of the different decay branches.*

4.1.8 ^{215}Ra

Isomeric states in ^{215}Ra have been previously studied in [87]. The delayed gamma-ray spectrum and partial level scheme are shown in Figs. 4.17 and 4.18 respectively. Time gates of 9.2 μs and 48.2 μs have been used to produce the upper and lower spectra in Fig. 4.17 respectively. Three isomeric states at excitation energies of x + 3757, x + 2247 and x + 1878 keV have been observed in this experiment, with spin and parities of $(43/2^-)$, $(31/2^-)$ and $(25/2^+)$, and half-lives of 555(10) ns, 1.39(7) μs and 7.1(2) μs respectively.

Table 4.9 shows the relevant information for the calculation of the isomeric ratios. The branching ratios for the 18 and 426 keV transitions have been obtained from the relative gamma-ray intensities of the 426, 407, 325, 323 and 152 keV transitions given in [87]. An isomeric ratio of 7.9(8)% has been obtained for the $I^\pi = (43/2^-)$ isomer. Isomeric ratios for the lower two isomers have not been calculated due to the difficulty in resolving the 193 and 196 keV, and 173 and 176 keV transitions.

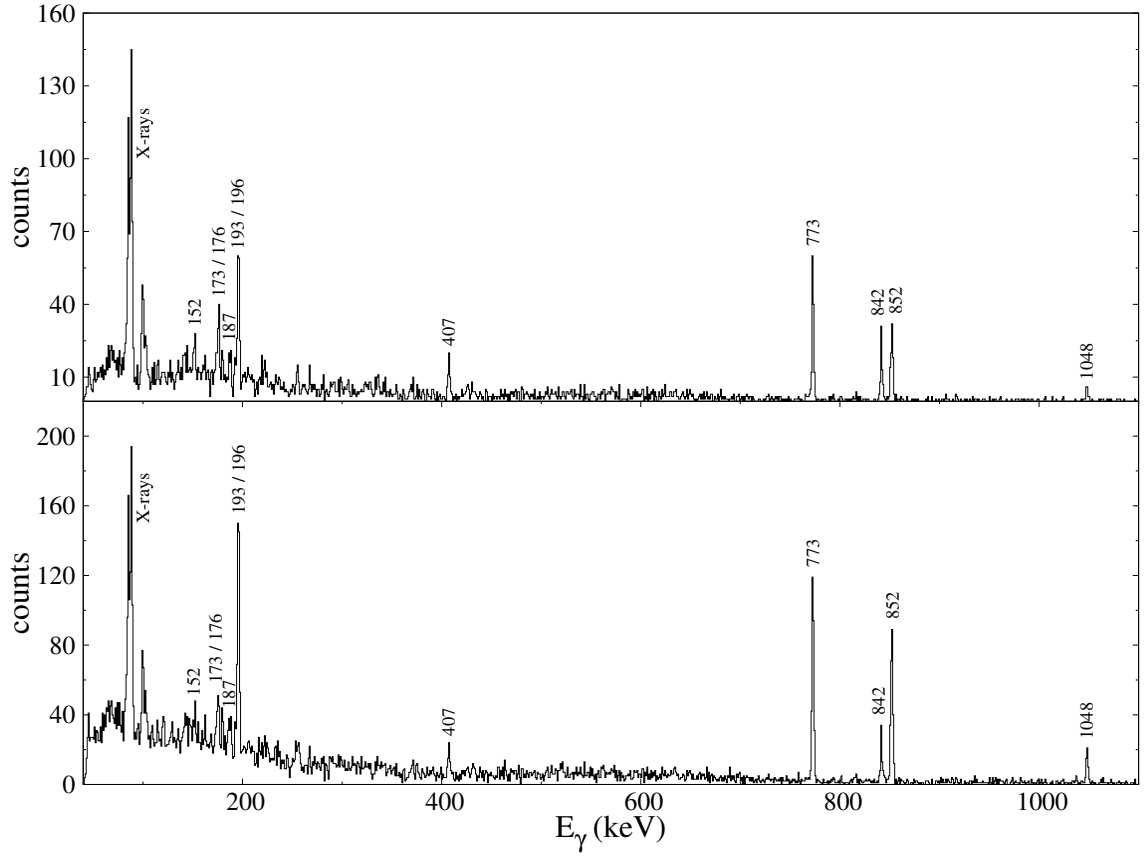

Figure 4.17: *The gamma-ray spectrum observed in coincidence with ^{215}Ra ions from the ^{214}Ra data set. Time windows of 9.2 and 48.2 μs have been used to produce the energy spectrum in the upper and lower panels respectively.*

I^π	E_γ(keV)	M	α [72, 73]	I_γ	b	F	G	R_{exp}
$(43/2^-)$	18	(E2)	24700(6)		0.82			
	426	E3	0.240(4)	86(35)	0.18	0.97(2)	0.94(3)	8(3)
	407	E1	0.0180(3)	224(40)	0.44	0.97(2)	0.94(3)	7(1)
	842	E1	0.00435(6)	588(66)	1.00	0.97(2)	0.97(3)	8.1(9)

Table 4.9: *Relevant information for the calculation of the isomeric ratio of the $(43/2^-)$ isomeric state in ^{215}Ra. The number of implanted ions was 7773.*

4.2 Results from the settings using the passive stopper data

Figs. 3.11 shows the isotopes of polonium (Z=84), astatine (Z=85), radon (Z=86) and francium (Z=87) identified in the ^{212}Rn data set, and Fig. 4.19 shows the identified isotopes of polonium (Z=84), radium(Z=88) and actinium (Z=89) in the ^{214}Th data set.

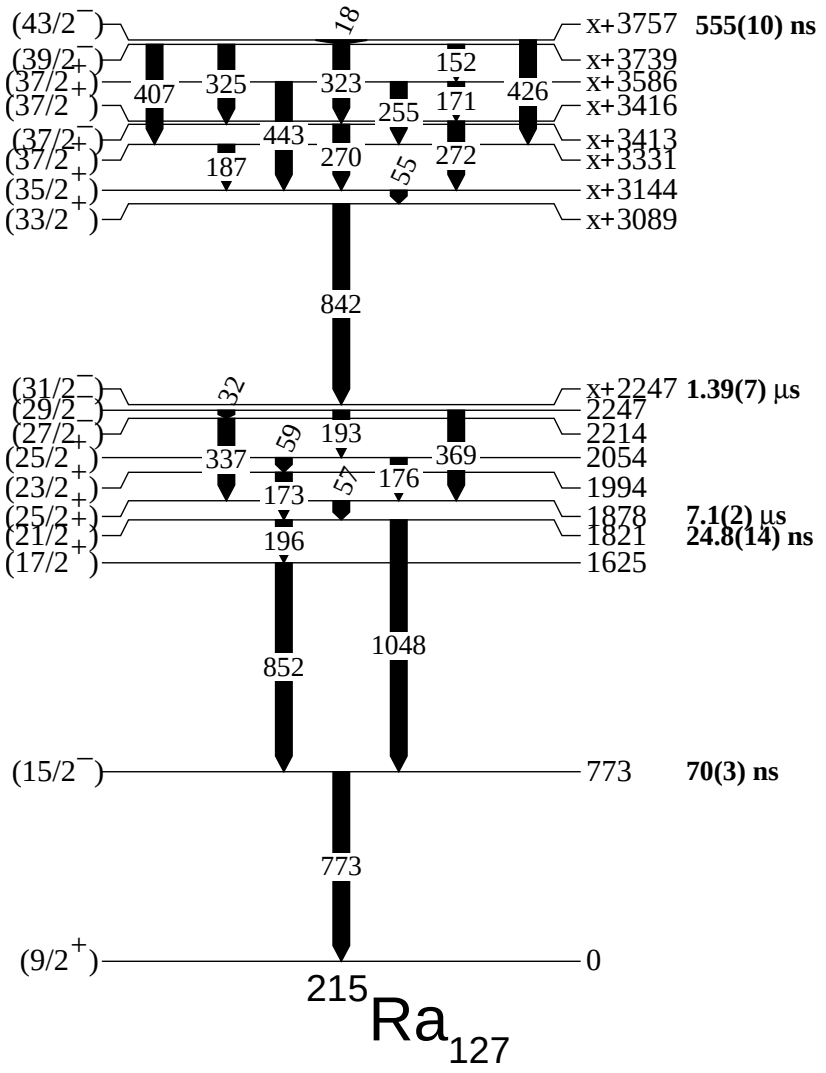

Figure 4.18: *A partial level scheme of* ^{215}*Ra. The width of the arrows is proportional to the total intensity of the different decay branches.*

4.2.1 ^{198}Po

Isomeric states in ^{198}Po have been previously studied in [88]. The delayed gamma-ray spectrum and partial level scheme are shown in Figs. 4.20 and 4.21 respectively. A time gate of 5.2 μs has been used to produce the energy spectrum. The two higher spin isomeric states at excitation energies of x + 2692 and 2566 keV have been observed in this experiment, with spin and parities of 12^+ and 11^-; and half-lives of 0.75(5) μs and 200(20) ns respectively. An attempt to measure the half-lives with the data from this experiment has been made, but due to the lack of statistics from the 126 keV transition decaying from the higher-lying isomer, experimental half-lives have been not obtained for this nucleus. The values from the literature, indicated in the level scheme, have been used for the calculation of the isomeric ratios.

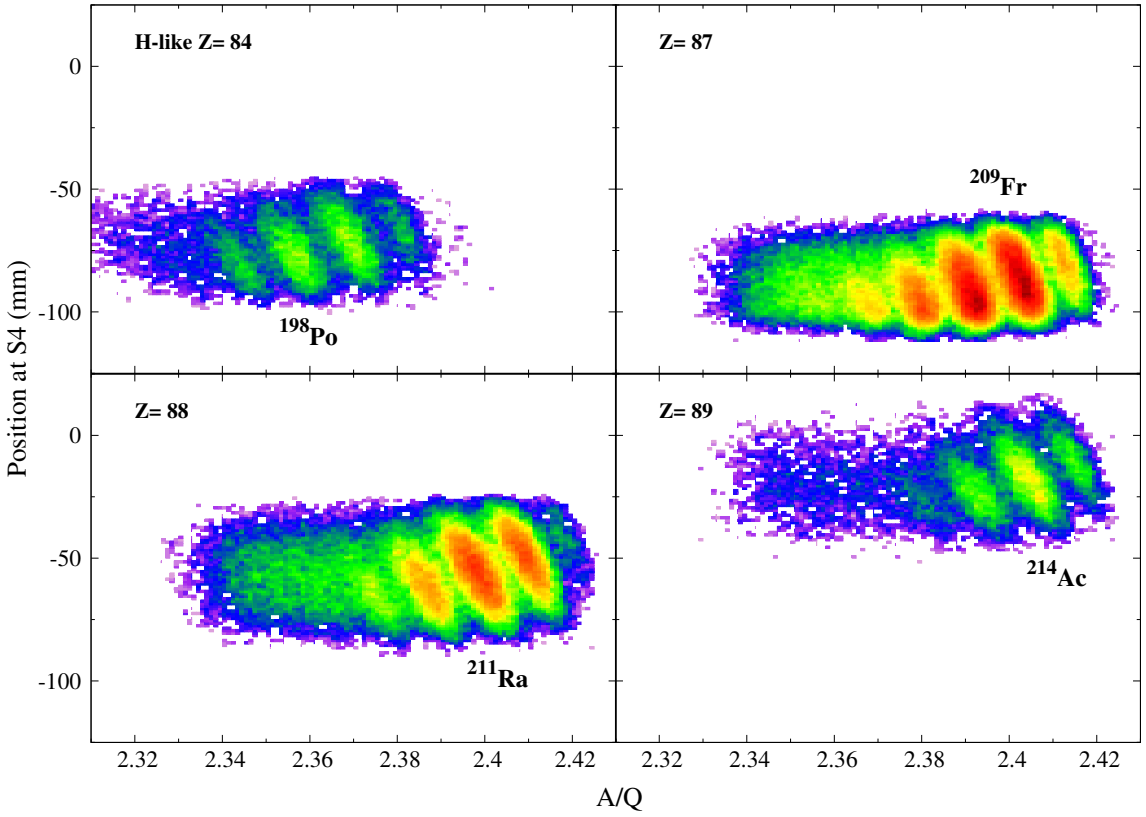

Figure 4.19: *Particle identification plots for the ^{214}Th data set. Each panel corresponds to the position versus A/Q ratio gated only on the indicated Z.*

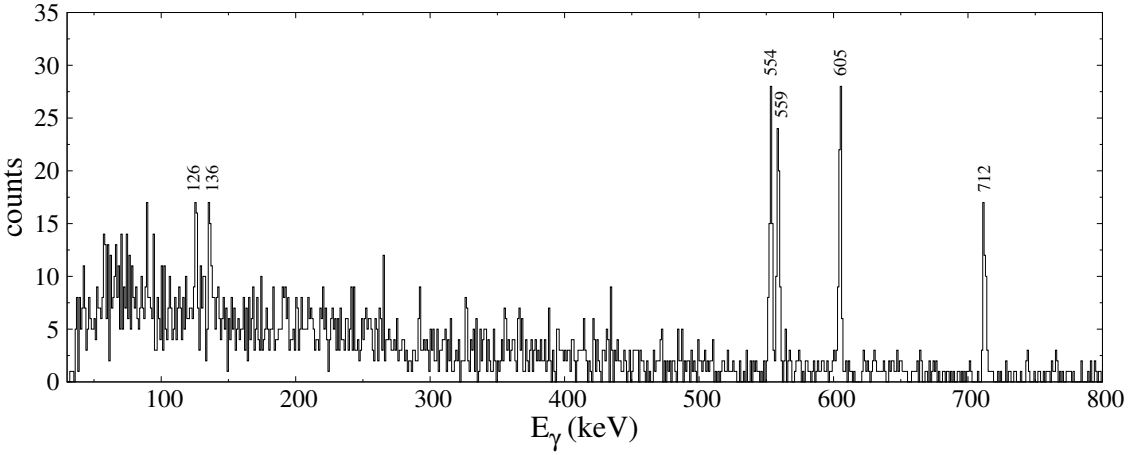

Figure 4.20: *The gamma-ray spectrum observed in coincidence with ^{198}Po ions from the H-like ΔQ=-1 ^{214}Th data set. A time gate of 5.2 μs has been used to produce the energy spectrum.*

Table 4.10 shows the relevant information for the calculation of the isomeric ratios. An

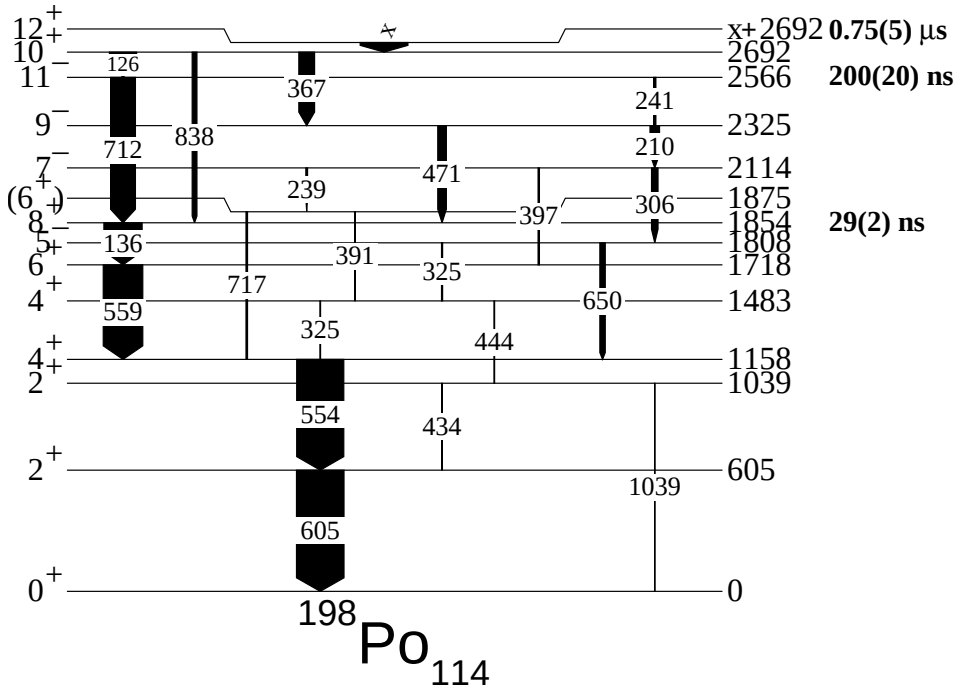

Figure 4.21: *A partial level scheme of ^{198}Po. The width of the arrows is proportional to the total intensity of the different decay branches.*

isomeric ratio of 4(2)% for the $I^{\pi} = 12^{+}$ level has been obtained from the 126 keV transition. The feeding from this isomer has been used to obtain a 20(9)% isomeric ratio for the $I^{\pi} = 11^{-}$ level. The isomeric ratio for the $I^{\pi} = 8^{+}$ levels has not been calculated due to the large uncertainties introduced when trying to subtract the feeding from two higher-lying isomers.

I^{π}	E_{γ}(keV)	M	α [72, 73]	I_{γ}	b	F	G	R_{exp} (%)
12^{+}	(50)	E2	140.1(2)		1.00			
	126	E1	0.256(4)	73(35)	0.57	0.999	0.73(3)	4(2)
11^{-}	712	E3	0.0396(6)	479(85)	0.92	0.54(3)	0.77(7)	20(9)

Table 4.10: *Relevant information for the calculation of the isomeric ratio of the 12^{+} and 11^{-} isomeric states in ^{198}Po. The number of implanted ions was 5570.*

4.2.2 ^{200}Po

Isomeric states in ^{200}Po have been previously studied in [88, 89]. The delayed gamma-ray spectrum and partial level scheme are shown in Figs. 4.22 and 4.23 respectively. A time gate of 2.2 μs has been used to produce the energy spectrum. Three isomeric states at excitation energies of 2804+X, 2596 and 1774 keV have been observed in this experiment, with spin and parities of 12^{+}, 11^{-} and 8^{+}; and half-lives of 268(3) ns, 100(10) and 61(3) ns

respectively. As for ^{198}Po, the half-lives have not been measured experimentally and the values from the literature, indicated in the level scheme, have been used for the calculation of the isomeric ratios.

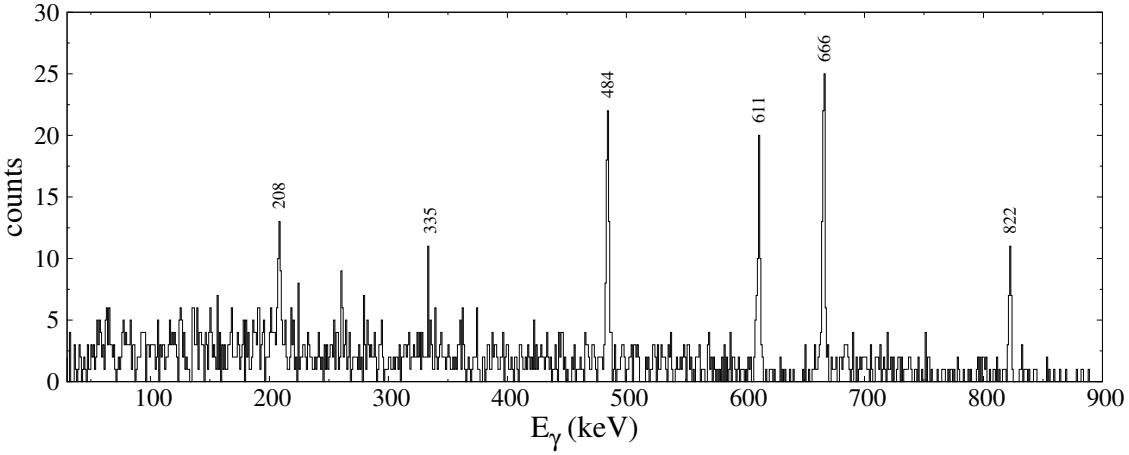

Figure 4.22: *The gamma-ray spectrum observed in coincidence with ^{200}Po ions from the H-like ΔQ=-1 ^{214}Th data set. A time gate of 2.2 μs has been used to produce the energy spectrum.*

Table 4.11 shows the relevant information for the calculation of the isomeric ratio. An isomeric ratio of 7(3) % for the $I^\pi = 12^+$ level has been obtained from the 208 keV transition. The feeding from this isomer has been used to obtain a 46(20) % isomeric ratio for the $I^\pi = 11^-$ level.

I^π	E_γ(keV)	M	α [72, 73]	I_γ	b	F	G	R_{exp} (%)
12^+	(50)	M1	12.16(17)		1.00			
	208	E1	0.0742(12)	113(40)	1.00	0.965	0.59(4)	7(3)
11^-	822	E3	0.0275(4)	339(76)	0.70	0.31(3)	0.7(1)	46(20)

Table 4.11: *Relevant information for the calculation of the isomeric ratio of the 12^+ and 11^- isomeric states in ^{200}Po. The number of implanted ions was 2954.*

4.2.3 ^{206}Po

Isomeric states in ^{206}Po have been previously studied in [90]. The delayed gamma-ray spectrum and partial level scheme are shown in Figs. 4.24 and 4.25 respectively. A time gate of 9.2 μs has been used to produce the energy spectrum. Two isomeric states with excitation energies at 2262 and 1586 keV have been observed in this experiment, with spin and parties of 9^- and 8^+, and half-lives of 1.05(6) μs and 232(4) ns respectively.

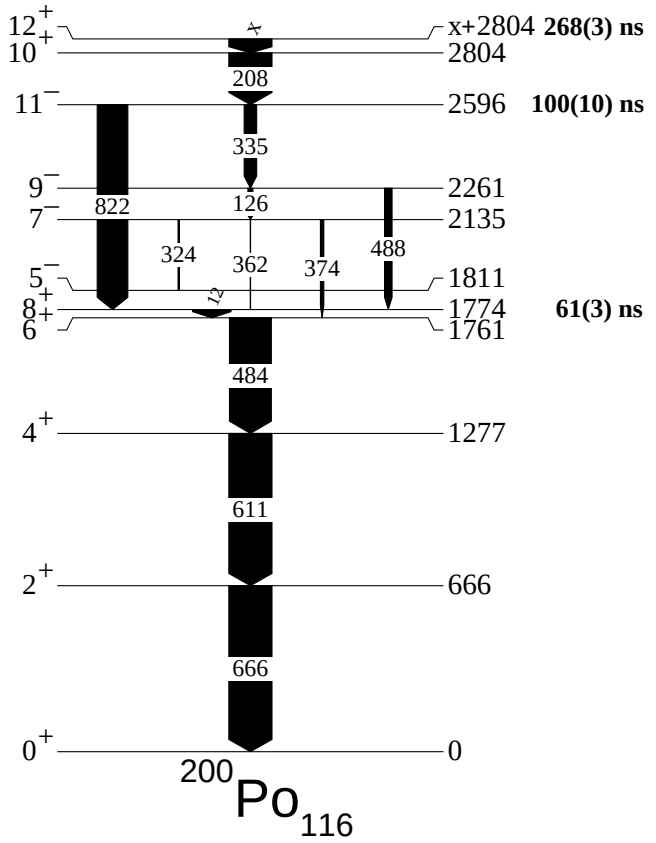

Figure 4.23: *A partial level scheme of ^{200}Po. The width of the arrows is proportional to the total intensity of the different decay branches.*

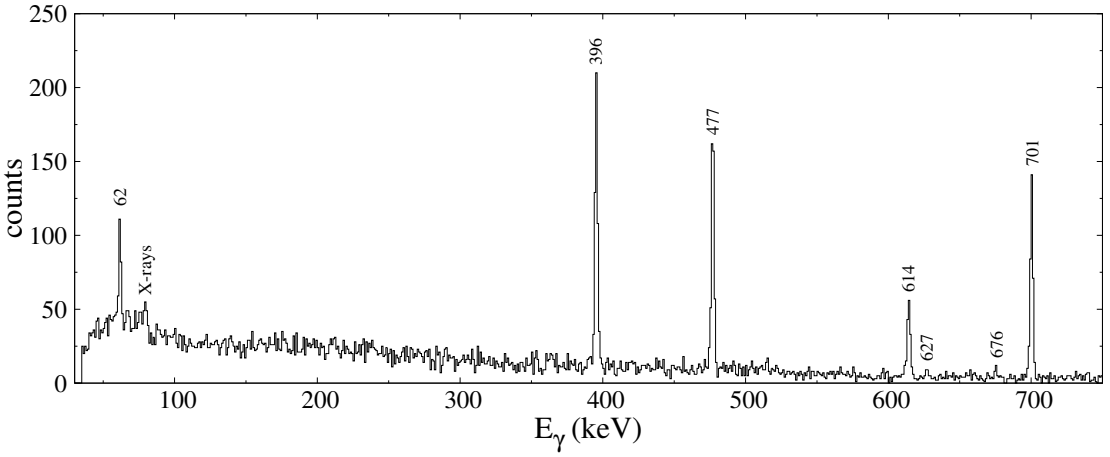

Figure 4.24: *The gamma-ray spectrum observed in coincidence with ^{206}Po ions from the ^{212}Rn data set. A time gate of 9.2 μs has been used to produce the energy spectrum.*

Table 4.12 shows the relevant information for the calculation of the isomeric ratio. An isomeric ratio of 15(2) % for the $I^{\pi} = 9^{-}$ level has been obtained from the 614 keV transition. The feeding from this isomer has been used to obtain a 12(2) % isomeric ratio

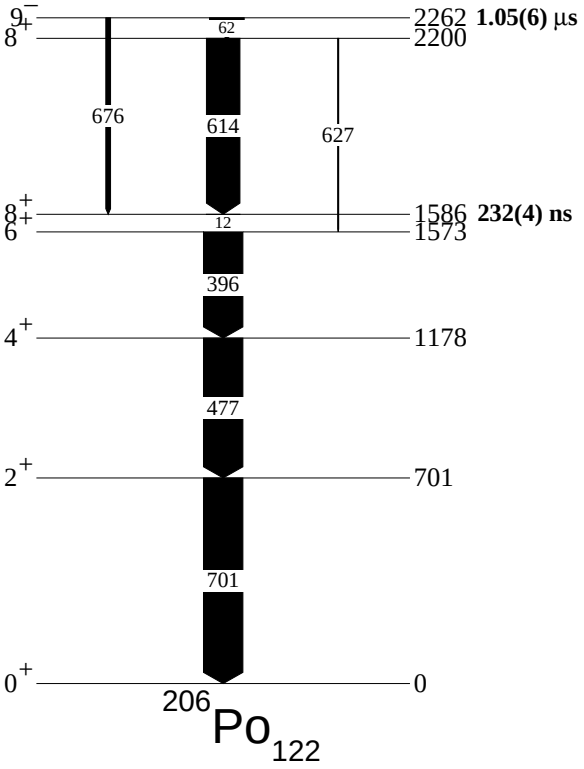

Figure 4.25: *A partial level scheme of ^{206}Po. The width of the arrows is proportional to the total intensity of the different decay branches.*

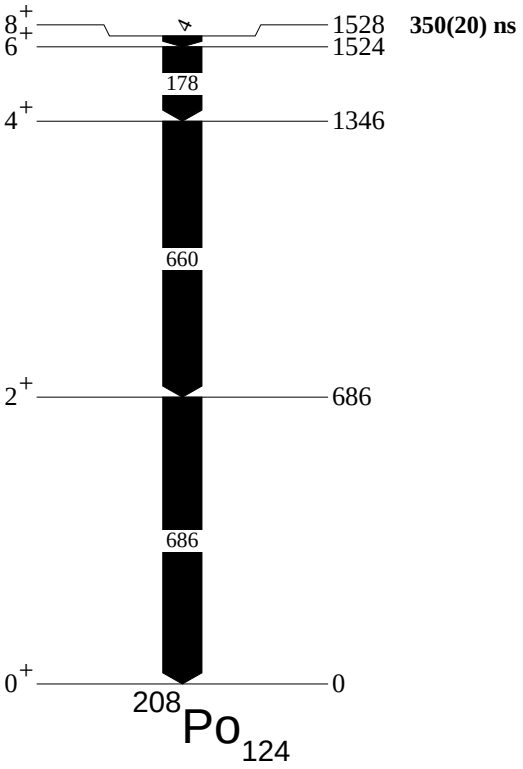

Figure 4.26: *A partial level scheme of ^{208}Po. The width of the arrows is proportional to the total intensity of the different decay branches.*

for the $I^{\pi} = 8^{+}$ level from the 396, 477 and 701 keV cascade transitions.

I^{π}	E_{γ}(keV)	M	α [72, 73]	I_{γ}	b	F	G	R_{exp} (%)
9^{-}	62	E1	0.355(6)		0.88			
	676	(E1)	0.00561(4)		0.12			
	614	M1	0.0739(4)	1413(173)	0.85	0.912	0.96(2)	15(2)
8^{+}	12	[E2]	45200(200)		1.00			
	396	E2	0.0579(5)	3341(290)	1.00	1.000	0.86(6)	13(3)
	477	E2	0.0359(4)	3300(295)	1.00	1.000	0.86(6)	12(3)
	701	E2	0.01507(21)	3377(313)	1.00	1.000	0.86(6)	12(3)

Table 4.12: *Relevant information for the calculation of the isomeric ratio of the 9^{-} and 8^{+} isomeric states in ^{206}Po. The number of implanted ions was 13724.*

4.2.4 ^{208}Po

Isomeric states in ^{208}Po have been previously studied in [91]. The partial level scheme and delayed gamma-ray spectrum and are shown in Figs. 4.26 and 4.27 respectively. A

time gate of 2.6 μs has been used to produce the energy spectrum. An isomeric state with spin and parity of 8^+ and a half-life of 350(20) ns has been observed.

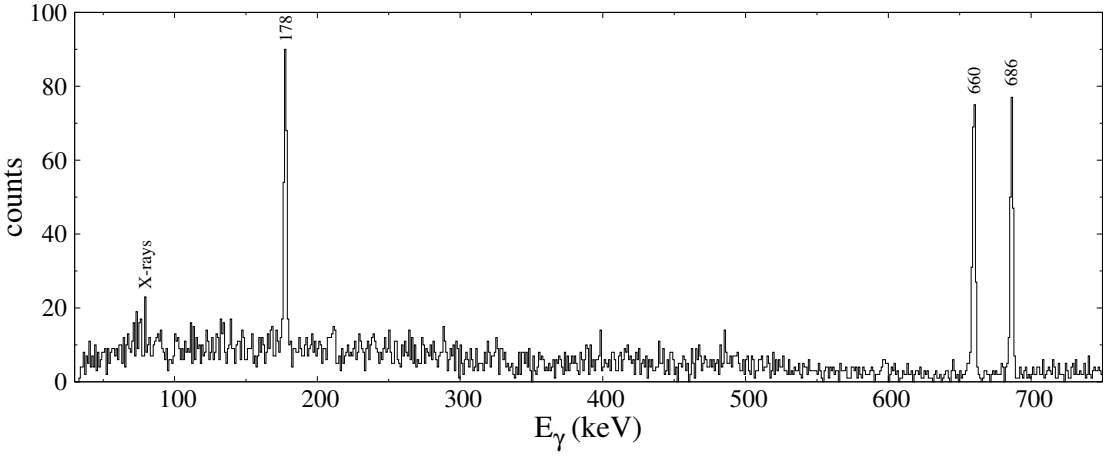

Figure 4.27: *The gamma-ray spectrum observed in coincidence with ^{208}Po ions from the ^{212}Rn data set. A time gate of 2.6 μs has been used.*

Table 4.13 shows the relevant information for the calculation of the isomeric ratio. An isomeric ratio of 27(2) % for the $I^\pi = 8^+$ level has been obtained from the 178, 660 and 686 keV cascade transitions.

I^π	E_γ(keV)	M	α [72, 73]	I_γ	b	F	G	R_{exp} (%)
8^+	4	E2	3250000(50000)		1.00			
	178	E2	0.202(24)	1031(152)	1.00	1.000	0.70(4)	30(5)
	660	E2	0.101(7)	2022(205)	1.00	1.000	0.90(4)	27(3)
	686	E2	0.099(7)	1888(201)	1.00	1.000	0.90(4)	25(3)

Table 4.13: *Relevant information for the calculation of the isomeric ratio of the 8^+ isomeric state in ^{208}Po. The number of implanted ions was 8454.*

4.2.5 ^{208}At

Isomeric states in ^{208}At have been previously studied in [92, 93]. The measured delayed gamma-ray spectrum and partial level scheme are shown in Figs. 4.28 and 4.29 respectively. Two isomeric states at excitation energies of 2276 and 1090 keV have been observed in this experiment, with spins and parities of 16^- and 10^-, and half-lives of 1.5(2) μs and 47.8(10) ns respectively. The energy spectrum includes some background contamination, mainly the 577 keV transition from ^{209}At.

Table 4.14 shows the relevant information for the calculation of the isomeric ratio. An isomeric ratio of 8.6(9)% for the $I^\pi = 16^-$ level has been obtained from the weighted mean

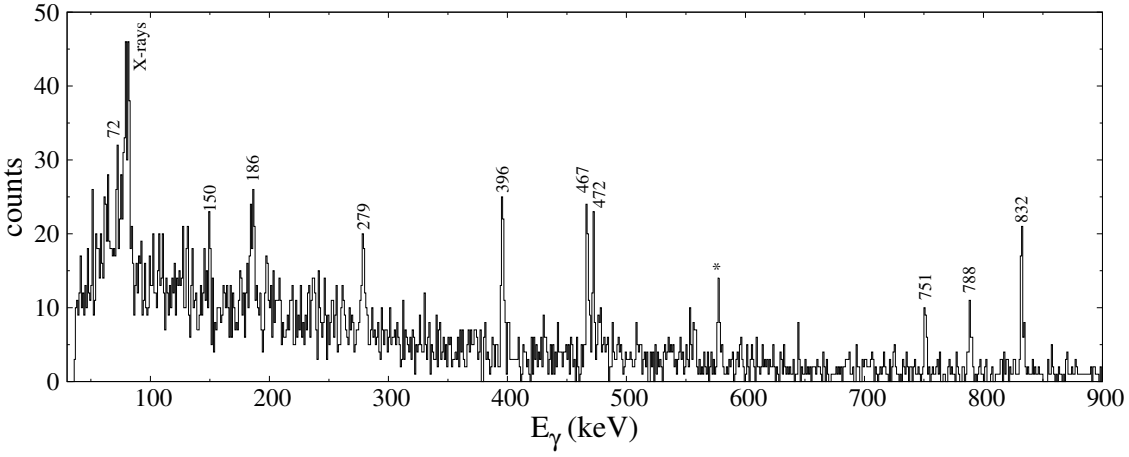

Figure 4.28: *The gamma-ray spectrum observed in coincidence with ^{208}At ions from the ^{212}Rn data set. A time gate of 6.8 μs has been used to produce the energy spectrum. The transition labelled as $*$ corresponds to the contamination from an isomer in ^{209}At.*

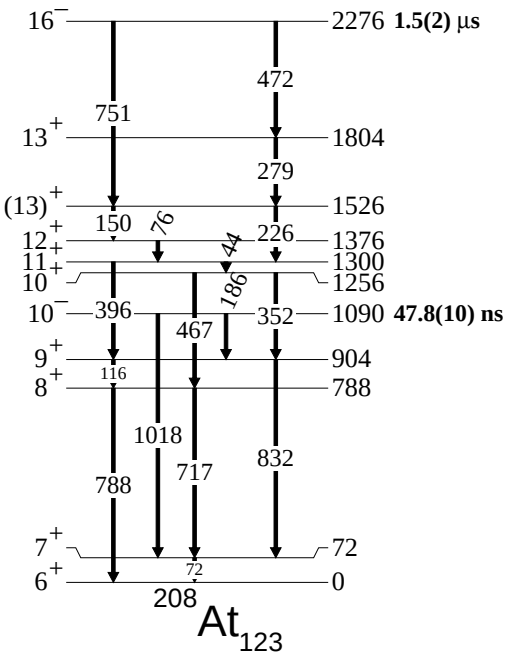

Figure 4.29: *A partial level scheme of ^{208}At. The width of the arrows is not proportional to the total intensity of the different decay branches.*

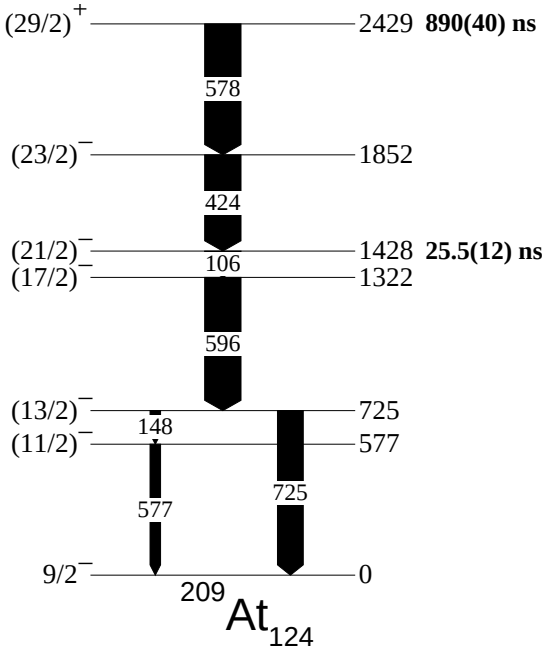

Figure 4.30: *A partial level scheme of ^{209}At. The width of the arrows is not proportional to the intensity of the different decay branches.*

of the isomeric ratios from the 472, 751, 279, 396 and 467 keV transitions. Due to the short half-life of the lower-lying isomer, the isomeric ratio for the 10^- level has not been calculated.

I^π	E_γ(keV)	M	α [72, 73]	I_γ	b	F	G	R_{exp} (%)
	472	E3	0.140(2)	271(59)	0.52	0.926(4)	0.92(1)	7.3(16)
	751	E3	0.0366(6)	277(67)	0.48	0.926(4)	0.94(1)	7.3(18)
16^-	279	M1	0.674(10)	254(79)	0.42	0.926(4)	0.90(1)	10(3)
	396	E2	0.0603(9)	371(69)	0.53	0.926(4)	0.92(1)	9.3(17)
	467	E2	0.0396(6)	379(76)	0.42	0.926(4)	0.92(1)	12(2)

Table 4.14: *Relevant information for the calculation of the isomeric ratio of the 16^- isomeric state in ^{208}At. The number of implanted ions was 9472.*

4.2.6 ^{209}At

Isomeric states in ^{209}At have been previously studied in [94, 95, 96, 97]. The partial level scheme and measured delayed gamma-ray spectrum are shown in Figs. 4.30 and 4.31 respectively. Two isomeric states at excitation energies of 2429 and 1428 keV have been observed in this experiment, with spins and parities $(29/2)^+$ and $(21/2)^-$, and half-lives of 0.89(4) μs and 25.5(12) ns respectively. The inset to Fig. 4.31 shows the decay from the higher-lying isomer, where a half-life of 0.81(18) μs has been obtained in agreement with the value from the literature, 0.89(4) μs. The half-lives from the literature have been adopted for the calculations.

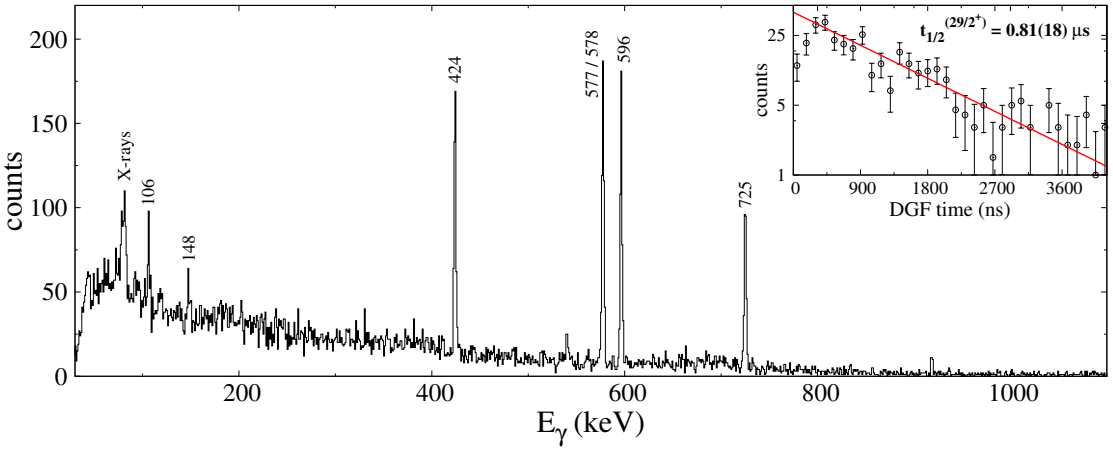

Figure 4.31: *The gamma-ray spectrum observed in coincidence with ^{209}At ions from the ^{212}Rn data set. A time gate of 8.8 μs has been used.*

Table 4.15 shows the relevant information for the calculation of the isomeric ratio. The 25.5(12) ns half-life of the lower isomer is too short to obtain an accurate isomeric ratio. Therefore a time gate starting at 800 ns was used to calculate the isomeric ratio of the transition below the 1428 keV level. The two transitions which are too close in energy to be resolved, 577 and 578 keV, have been omitted from the calculations. An isomeric

ratio of 17(1)% for the $I^{\pi} = (29/2)^{+}$ level has been obtained from the weighted mean of the isomeric ratios from the 424, 106, 596, 725 and 148 keV transitions.

I^{π}	E_{γ}(keV)	M	α [72, 73]	I_{γ}	b	F	G	R_{exp} (%)
	424	M1	0.215(3)	3697(344)	1.00	0.877(5)	0.93(2)	17(2)
	106	E2	6.03(9)	261(72)	1.00	0.877(5)	0.51(2)	15(4)
$(29/2)^{+}$	596	E2	0.0224(4)	1933(201)	1.00	0.877(5)	0.51(2)	16(2)
	148	M1	3.96(6)	141(82)	0.29	0.877(5)	0.51(2)	20(12)
	725	E2	0.01472(21)	1545(182)	0.71	0.877(5)	0.51(2)	18(2)

Table 4.15: *Relevant information for the calculation of the isomeric ratio of the $(29/2)^{+}$ isomeric state in ^{209}At. The number of implanted ions was 26936.*

4.2.7 ^{210}At

Isomeric states in ^{210}At have been previously studied in [97, 98, 99, 100]. The measured delayed gamma-ray spectrum and partial level scheme are shown in Figs. 4.32 and 4.33 respectively. Times gates of 33.4 μs and 3.9 μs have been used to produce the lower and upper panels of Fig. 4.32, revealing the different decay time characteristics of the two isomeric states observed in this experiment. The isomers lie at excitation energies of 4028 and 2550 keV, have spins and parities of 19^{+} and 15^{-}, and half-lives of 5.66(7) μs and 482(6) ns respectively. The inset plots of Fig. 4.32 show the half-lives measured in this work, 5.7(23) μs and 449(44) ns, which are in good agreement with the published values. The half-lives from the literature have been used for the calculations.

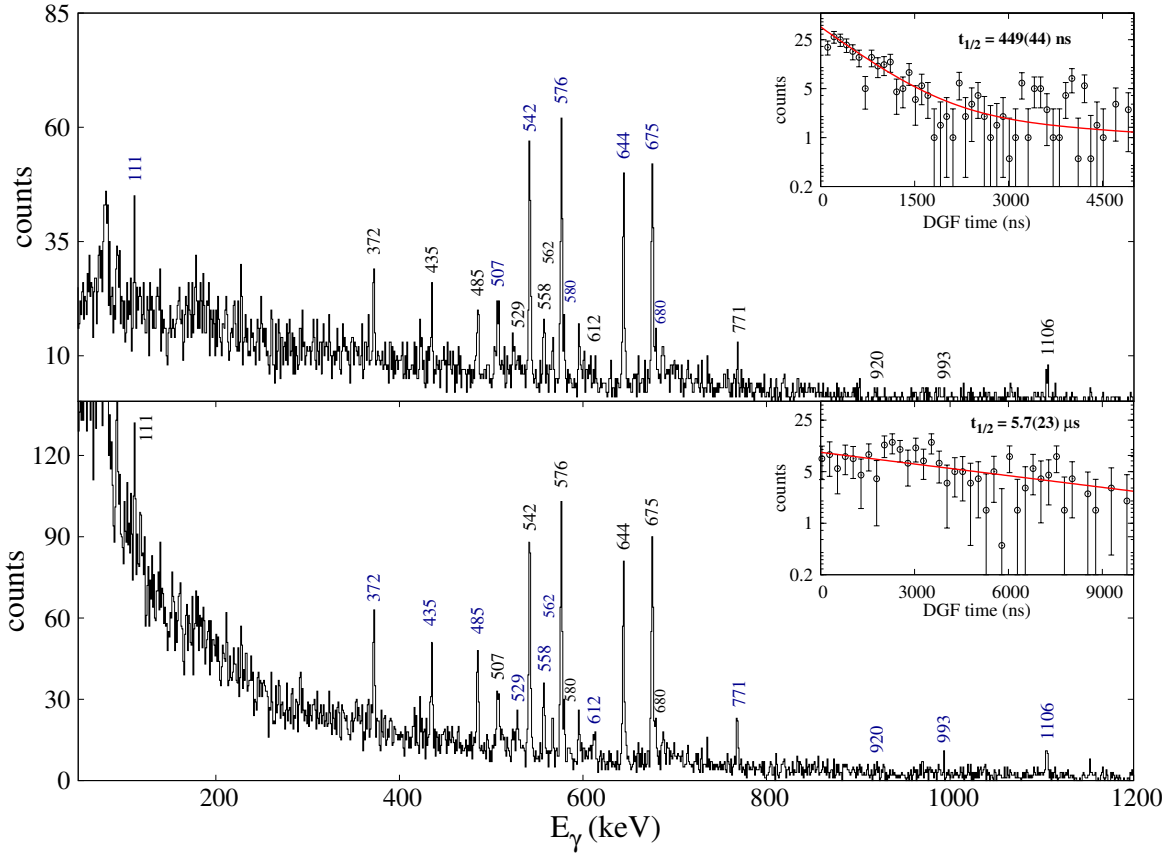

Figure 4.32: *The gamma-ray spectrum observed in coincidence with ^{210}At ions from the ^{212}Rn data set. Time gates of 33.4 µs and 3.9 µs have been used for the lower and upper panel respectively. The inset plots represent the half-lives of the two isomeric states measured in this work.*

Table 4.16 shows the relevant information for the calculation of the isomeric ratios. An isomeric ratio of 8.9(9)% for the $I^{\pi} = 19^{+}$ has been obtained from the weighted mean of the isomeric ratios from the 372, 485, 612 and 1106 keV transitions. An isomeric ratio of 5.2(7)% for the 15^{-} level has been obtained considering an 82% feeding from the isomer above.

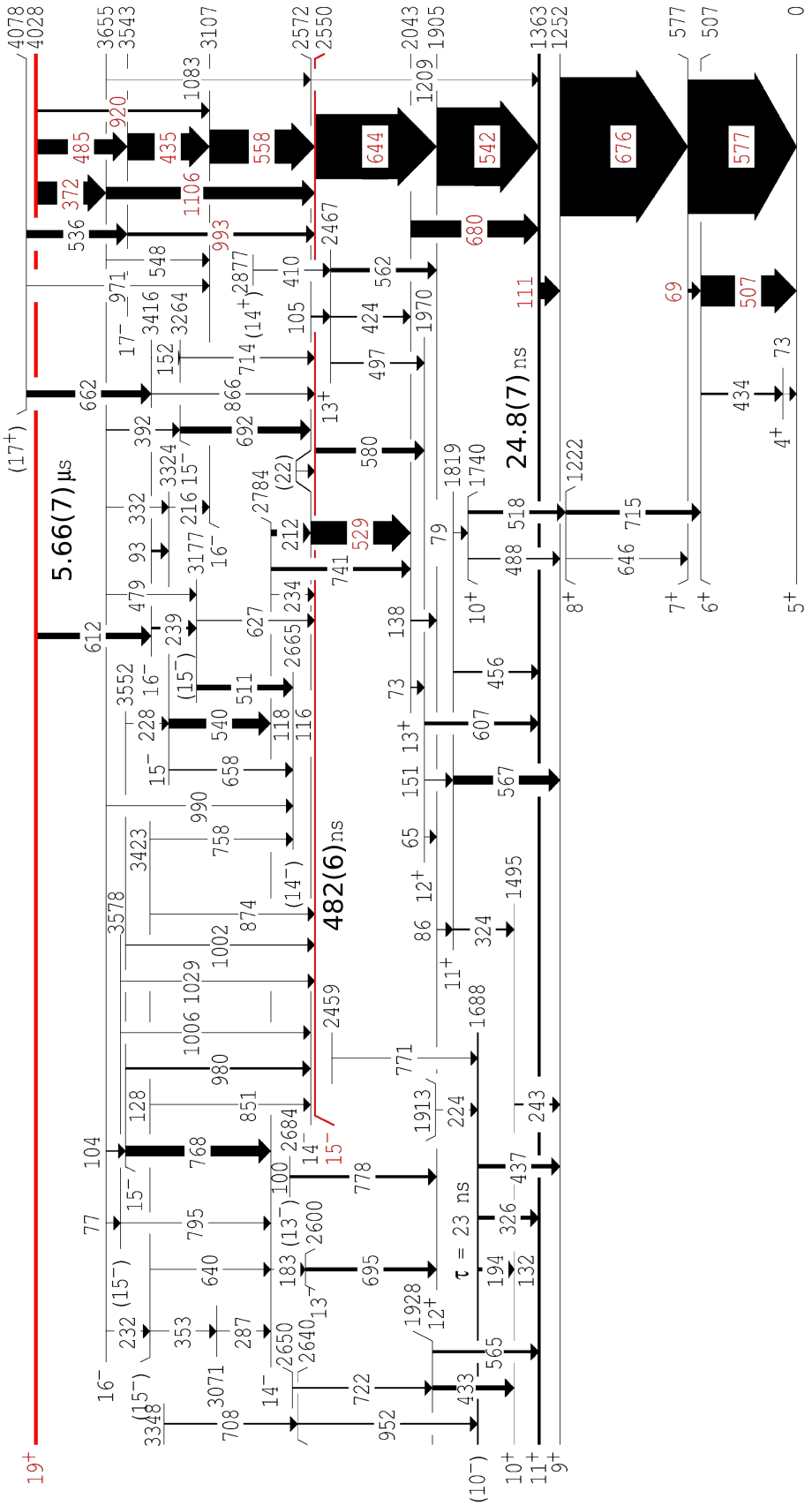

Figure 4.33: *A partial level scheme of* ^{210}*At taken and adapted from [100] with permission of the author. The width of the arrows is proportional to the gamma-ray intensity of the different decay branches.*

I^π	E_γ(keV)	M	α [72, 73]	I_γ	b	F	G	R_{exp} (%)
19^+	372	E3	0.330(2)	696(114)	0.42	0.984	0.970(3)	7.4(12)
	485	M2	0.453(2)	802(134)	0.36	0.984	0.974(3)	13(2)
	612	E3	0.0650(2)	188(86)	0.11	0.984	0.976(3)	7(3)
	1106	M1	0.0190(2)	483(97)	0.19	0.984	0.980(3)	10(2)
15^-	580	E3	0.0650(2)	358(217)	0.08	0.776	0.91(3)	4.9(46)
	644	E3	0.0230(2)	1809(213)	0.92	0.776	0.91(3)	4.9(14)
	542	M1	0.0190(2)	1771(179)	0.84	0.776	0.91(3)	5.4(14)

Table 4.16: *Relevant information for the calculation of the isomeric ratios of the 19^+ and 15^- isomeric states in ^{210}At. The number of implanted ions was 26698 and the feeding from the $I^\pi = 19^+$ to the 15^- isomeric levels is 82%.*

4.2.8 ^{211}At

Isomeric states in ^{211}At have been previously studied in [100, 101]. The measured delayed gamma-ray spectrum and partial level scheme are shown in Figs. 4.34 and 4.35 respectively. Three isomeric states at excitation energies of 4814, 2640 and 1416 keV have been observed in this experiment, with spins and parities of $39/2^-$, $29/2^+$ and $21/2^-$ and half-lives of 4.2(4) μs, 50.8(7) and 35.1(7) ns. The inset plot in Fig. 4.34 shows the half-live for the $39/2^-$ isomer as measured in this experiment. A value of 4.3(13) μs has been obtained, in good agreement with the 4.2(4) μs half-life from the literature adopted for the calculations.

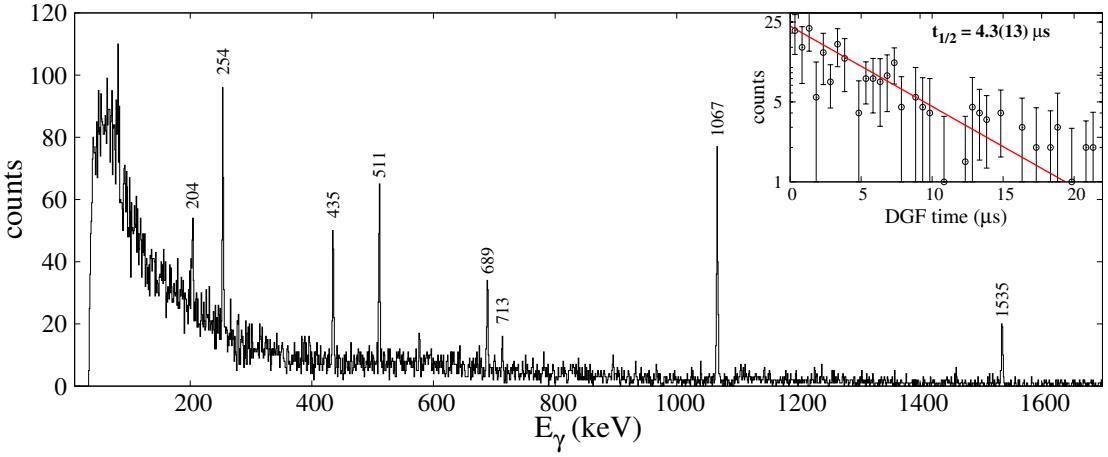

Figure 4.34: *The gamma-ray spectrum observed in coincidence with ^{211}At ions from the ^{212}Rn data set. A time gate of 27.9 μs has been used to produce the energy spectrum.*

Table 4.17 shows the relevant information for the calculation of the isomeric ratios. A time window starting at 612 ns has been used for the calculations of transitions below the 2640 keV level in order to avoid any contribution to the intensity from the $29/2^+$ and

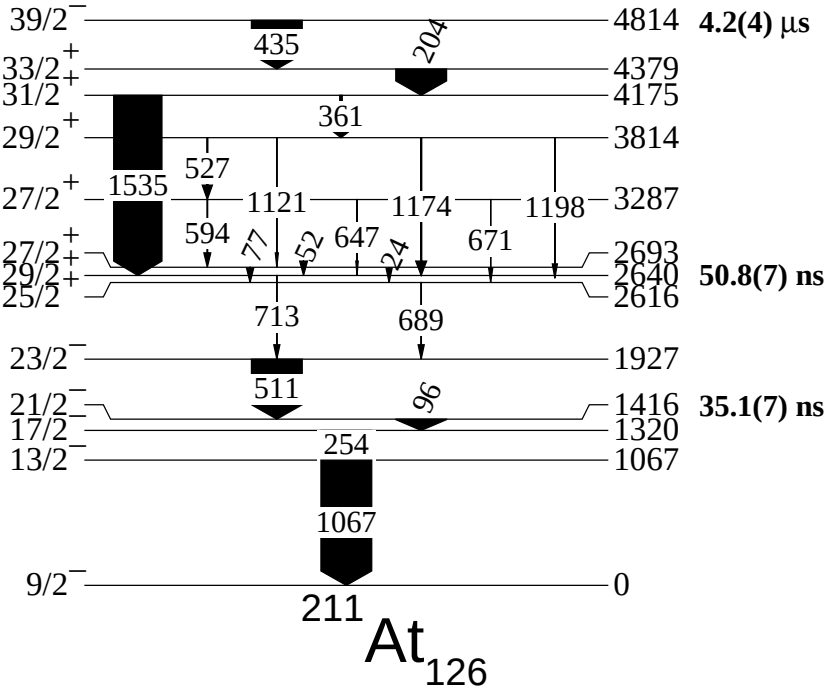

Figure 4.35: *A partial level scheme of ^{211}At. The width of the arrows is proportional to the gamma-ray intensity of the different decay branches.*

$21/2^-$ isomers. Branching ratios of 77% and 23% have been calculated for the 713 and 689 keV transitions. An isomeric ratio of 6.6(4)% for the $I^\pi = 39/2^-$ has been obtained from the weighted mean of the isomeric ratios obtained for the 435, 204, 1535, 713, 689 511, 254 and 1067 keV transitions.

I^π	E_γ(keV)	M	α [72, 73]	I_γ	b	F	G	R_{exp} (%)
$39/2^-$	435	E3	0.184(3)	862(115)	1.00	0.975	0.980(4)	7(1)
	204	M1	1.607(23)	353(92)	1.00	0.975	0.960(4)	6(2)
	1535	M1	0.0076(1)	982(146)	0.95	0.975	0.992(4)	7(1)
	713	E3	0.0424(6)	186(63)	0.23	0.975	0.894(4)	6(2)
	689	(E1,E2)	0.011(6)	577(100)	0.77	0.975	0.894(4)	5.3(9)
	511	M1	0.1306(19)	904(119)	1.00	0.975	0.894(4)	7.1(9)
	254	E2	0.283(4)	680(97)	1.00	0.975	0.894(4)	6.1(9)
	1067	(E2)	0.0048(1)	1257(156)	1.00	0.975	0.894(4)	9(1)

Table 4.17: *Relevant information for the calculation of the isomeric ratio of the $39/2^-$ isomeric state in ^{211}At. The number of implanted ions was 16446.*

4.2.9 ^{210}Rn

Isomeric states in ^{210}Rn have been previously studied in [67, 68, 69, 70], as discussed in Section 4.1.1. The partial level scheme and measured delayed gamma-ray spectrum are shown in Figs. 4.3 and 4.36 respectively. Two isomers have been observed with excitation

energies of x + 3812 and x +1665 keV, spins and parities of $(17)^-$ and (8^+), and half-lives of 1.06(5) μs and 644(40) ns respectively.

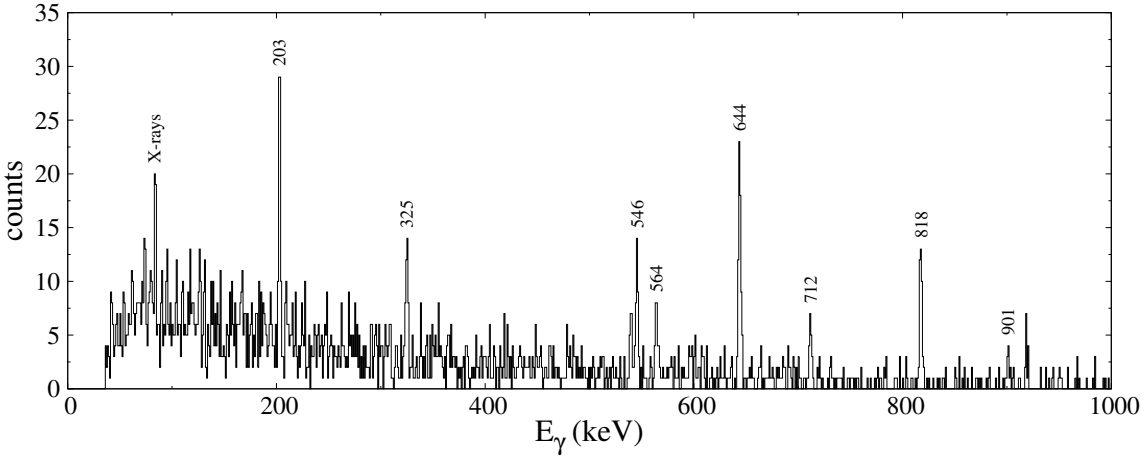

Figure 4.36: *The gamma-ray spectrum observed in coincidence with ^{210}Rn ions from the ^{212}Rn data set. A time gate of 6.7 μs has been used to produce the energy spectrum.*

Table 4.18 shows the relevant information for the calculation of the isomeric ratios. The isomeric ratio of the $I^\pi = (17)^-$ isomeric state has been calculated using the 564, 325, 546 and 712 keV transitions. Due to the low statistics, it has not been possible to measure the branching ratio for 111 keV transition, therefore the relative gamma-ray intensities from [71] have been used to calculate the branching ratio for the 712 keV transition. The isomeric ratio for the $(17)^-$ isomer is 10(1)%, calculated as the weighted mean isomeric ratio from the other three transitions. A weighted mean isomeric ratio of 14(2)% has been obtained for the $I^\pi = (8^+)$ isomer, using the 203, 901, 818, and 644 keV transitions.

I^π	E_γ(keV)	M	α [72, 73]	I_γ	b	F	G	R_{exp}(%)
$(17)^-$	564	E3	0.0851(12)	179(46)	1.00	0.897(5)	0.94(2)	10(2)
	325	E2	0.11(1)	185(53)	1.00	0.897(5)	0.92(2)	10(3)
	546	E2	0.0287(4)	236(55)	1.00	0.897(5)	0.94(2)	12(3)
	712	E2	0.01602(23)	124(42)	0.80	0.897(5)	0.96(2)	3(8)
(8^+)	<50	(E2)	>245(4)		1.00			
	203	E2	0.495(7)	275(50)	0.81	0.999	0.80(2)	15(5)
	901	E2	0.00995(14)	106(36)	0.19	0.999	0.97(3)	15(9)
	818	E2	0.01208(17)	391(72)	0.81	0.999	0.97(3)	11(4)
	644	E2	0.0199(3)	544(86)	1.00	0.999	0.95(3)	15(4)

Table 4.18: *Relevant information for the calculation of the isomeric ratios of the $(17)^-$ and (8^+) isomeric states in ^{210}Rn. The number of implanted ions was 2363.*

4.2.10 ^{211}Rn

Isomeric states in ^{211}Rn have been previously studied in [74, 75], as discussed in Section 4.1.2. The partial level scheme and delayed gamma-ray spectrum are shown in Figs. 4.5 and 4.37 respectively.

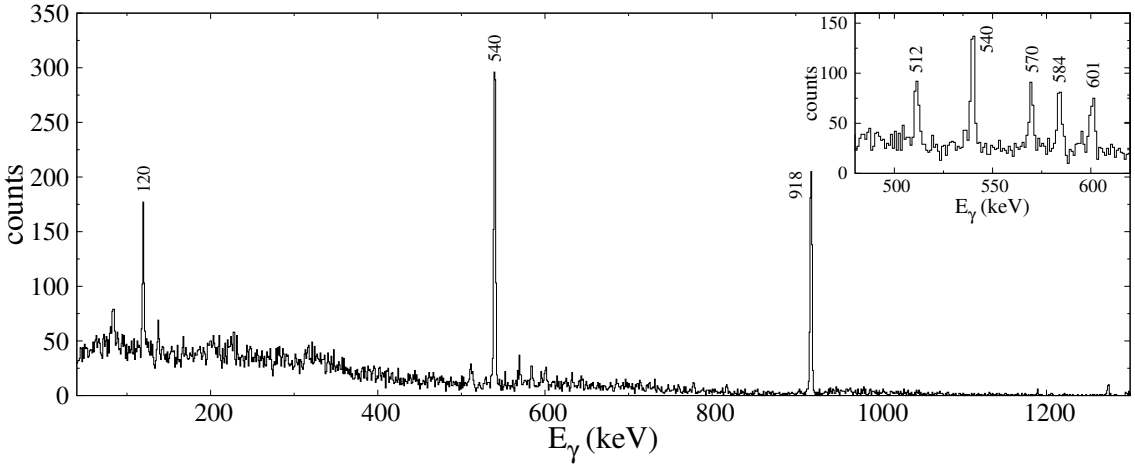

Figure 4.37: *The gamma-ray spectrum observed in coincidence with ^{211}Rn ions from the ^{212}Rn data set. Time gates of 7.6 μs and 450 ns have been used for the main and inset plots respectively.*

Table 4.19 shows the relevant information for the calculations. Isomeric ratios of 10(2)% using the 601, 512, 584, 570 keV transitions, and 26(2)% using the 120, 540 and 918 keV transitions have been obtained for the $I^\pi = (35/2^+)$ and $(17/2^-)$ states respectively.

I^π	E_γ(keV)	M	α [72, 73]	I_γ	b	F	G	R_{exp} (%)
$(35/2^+)$	(52)	(M1)	17.21(24)		0.03			
	82	(E2)	20.9(4)		0.97			
	601	E1	0.00761(11)	1897(230)	0.94	0.866(2)	1.0(4)	10(4)
	512	E2	0.0333(5)	1408(180)	0.91	0.866(2)	1.0(4)	10(4)
	584	E2	0.0246(4)	1478(186)	0.91	0.866(2)	1.0(4)	10(4)
	570	E2	0.0260(4)	1267(177)	0.82	0.866(2)	1.0(4)	9(4)
$(17/2^-)$	(<50)	(E2)	>245		1			
	120	E2	3.88(6)	1002(155)	1.00	0.999(2)	0.70(2)	25(6)
	540	E2	0.0294(5)	6491(550)	1.00	0.999(2)	0.94(3)	25(4)
	918	E2	0.00959(14)	6418(528)	1.00	0.999(2)	0.92(3)	26(4)

Table 4.19: *Relevant information for the calculation of the isomeric ratios of the $(35/2^+)$ and $(17/2^-)$ isomeric states in ^{211}Rn. The number of implanted ions was 19543.*

4.2.11 ^{212}Rn

Isomeric states in ^{212}Rn have been previously studied in [102, 103, 104]. The measured delayed gamma-ray spectrum and partial level scheme are shown in Figs. 4.38 and 4.39 respectively. Isomeric states at excitation energies of 6174, 4066, 1694 and 1640 keV have been observed in this experiment, with spins and parities 22^+, 17^-, 8^+ and 6^+, and half-lives of 109(5), 28.9(14), 910(30) and 118(14) ns respectively. Two other isomers with spins and parities of 27^- and 30^+ has not been observed in this experiment.

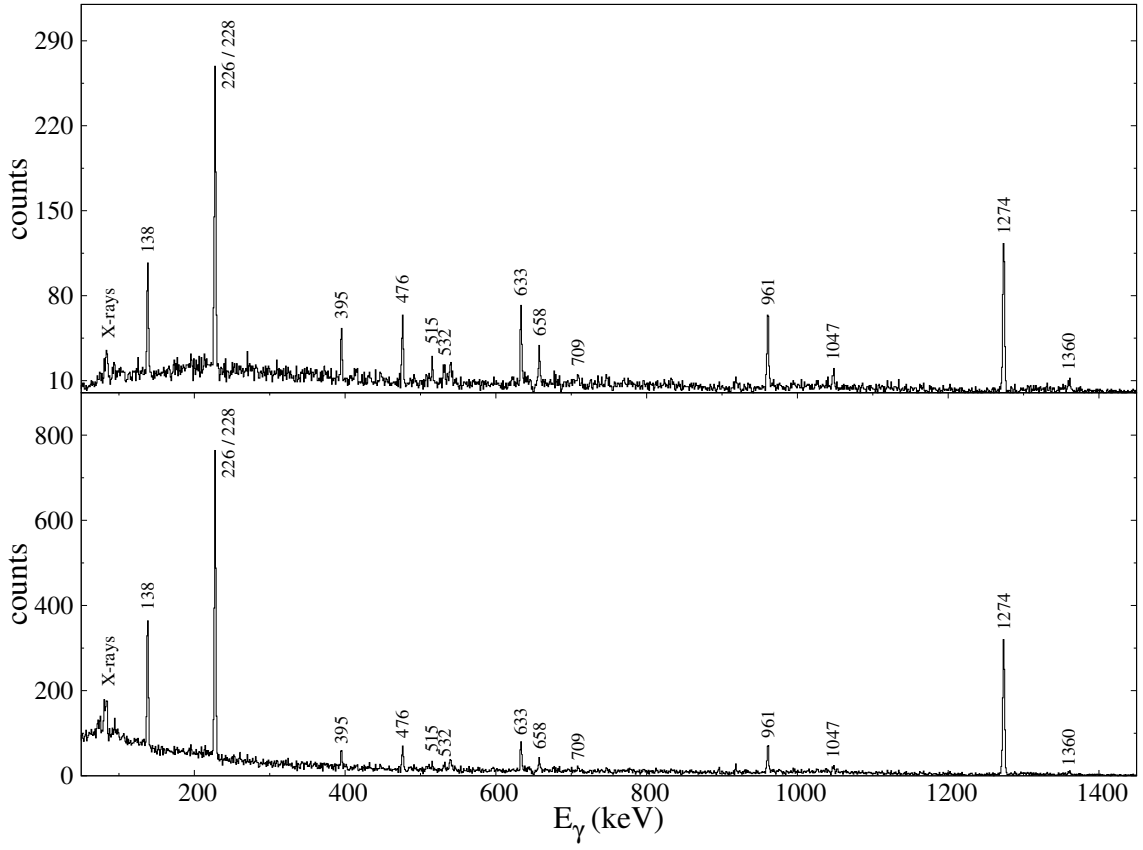

Figure 4.38: *The gamma-ray spectrum observed in coincidence with ^{212}Rn ions in the ^{212}Rn data set. Time gates of 700 ns and 11 μs and have been used to produce the top and bottom spectra respectively.*

Table 4.20 shows the relevant information for the calculation of the isomeric ratios. Relative intensities of the gamma rays directly depopulating the isomer have been taken from [102] to obtain the total branching ratios. An isomeric ratio of 3.4(5)% for the $I^\pi = 22^+$ level has been obtained from the weighted mean of the isomeric ratios from the 395, 658, 532 and 1047 keV transitions. Also a delayed time window has been applied to remove the decay of the short isomers, leaving only the decay from the $I^\pi = 8^+$ level, for which an isomeric ratio of 34(2) % has been obtained.

I^π	E_γ(keV)	M	α [72, 73]	I_γ	b	F	G	R_{exp} (%)
	747	E2	0.01450(21)		0.11			
	7.6	E2	635000		0.86			
	402	E3	0.258(4)		0.02			
22^+	395	E1	0.0181(3)	677(124)	0.78	0.855(3)	0.65(11)	3.7(9)
	658	M1	0.0726(11)	590(134)	0.74	0.855(3)	0.77(13)	3.0(9)
	532	M1	0.1273(18)	344(114)	0.45	0.855(3)	0.71(12)	3.3(12)
	1047	E2+M1	0.0122(11)	279(116)	0.26	0.861(5)	0.84(14)	3.6(16)
	54	E2	153.3(4)		1			
8^+	138	E2	2.18(2)	1802(381)	1	0.999	0.41(1)	33(7)
	228	E2	0.339(3)	4398(359)	1	0.999	0.41(1)	34(3)
	1274	E2	0.00520(4)	5939(519)	1	0.999	0.41(1)	34(3)

Table 4.20: *Relevant information for the calculation of the isomeric ratio of the 22^+ and 8^+ isomeric states in ^{212}Rn. The number of implanted ions was 42650.*

4.2.12 ^{213}Rn

Isomeric states in ^{213}Rn have been previously studied in [105]. The measured delayed gamma-ray spectrum and partial level scheme are shown in Figs. 4.40 and 4.41 respectively. Isomeric states at excitation energies of 6029, 3545, 3079, 2237 and 1714 keV have been observed in this experiment, with spins and parities $(55/2^+)$, $(43/2^-)$, $(37/2^+)$, $(31/2^-)$ and $(25/2^+)$, and half-lives of 164(11) ns, 28(1) ns, 26(1) ns, 1.36(7) μs and 1.00(21) μs respectively. Table 4.21 shows the relevant information for the calculation of the isomeric ratios. An isomeric ratio of 1.0(3)% for the $I^\pi = (55/2^+)$ has been obtained from the 1010 keV transition. An 8(4)% isomeric ratio has been obtained for the $I^\pi = (43/2^-)$ level subtracting the feeding from the isomer above. To obtain isomeric ratios for the long lived isomers a time gate starting at 1.3 μs was used to remove any feeding from the higher-lying short isomers. Isomeric ratios of 17(2)% and 6(3)% have been obtained for the 1.36 and 1.00 μs isomeric states.

4.2.13 ^{214}Rn

Isomeric states in ^{214}Rn have been previously studied in [106, 107]. The measured delayed gamma-ray spectrum and partial level scheme are shown in Figs. 4.42 and 4.43 respectively. Two isomeric states with excitation energies of 3490 and 4525 keV have been observed in this experiment, spins and parities of 18^+ and (22^+), and half-lives of 44(3) and 245(30) ns respectively.

Table 4.22 shows the relevant information for the calculation of the isomeric ratios. It has not been possible to use the transitions depopulating the $I^\pi=18^+$ isomer in the calculations because delaying the time gate so that its decay is not seen, reduces the statistics such

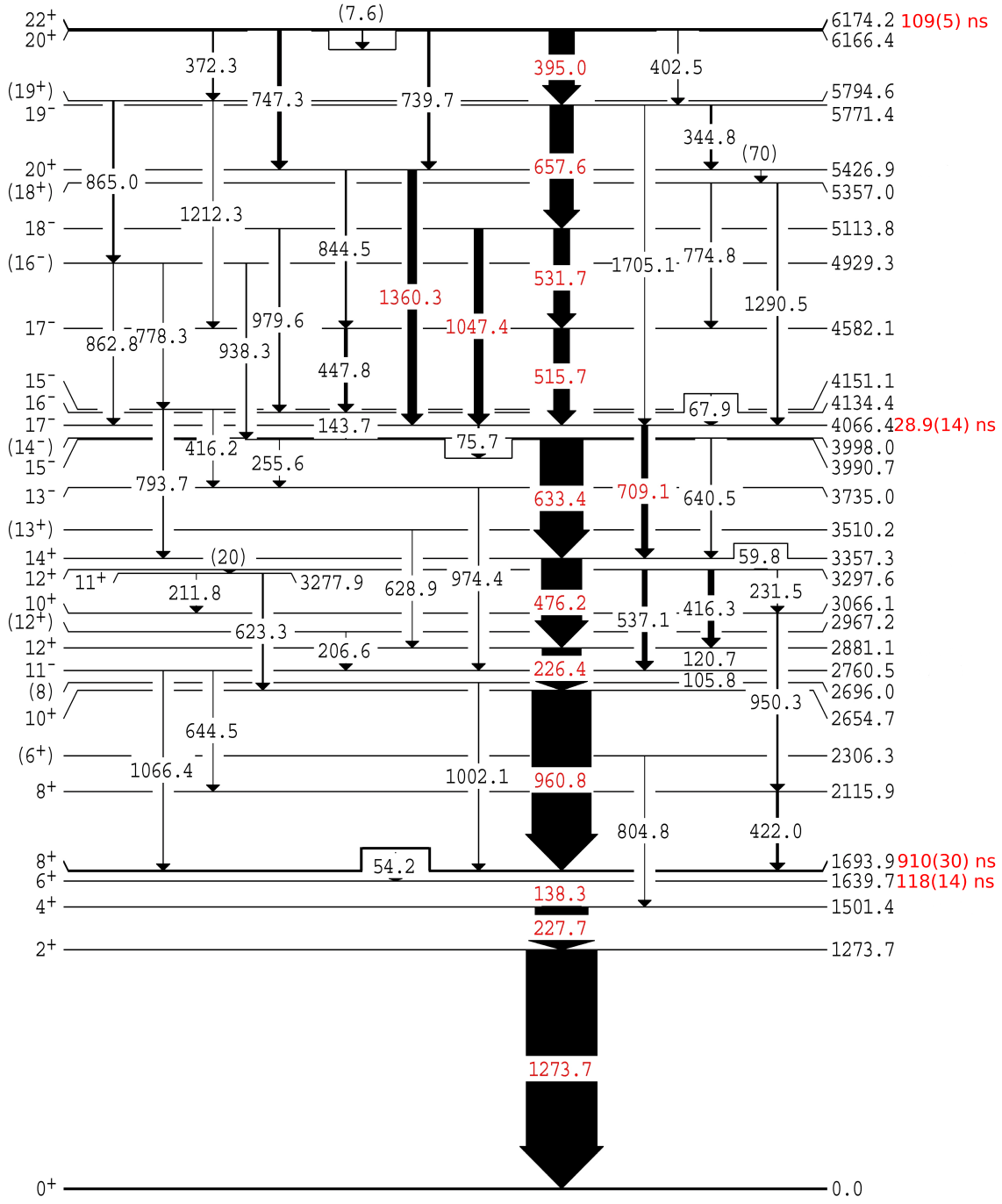

Figure 4.39: *A partial level scheme of* ^{212}*Rn taken from [102] with permission of the author. The width of the arrows is proportional to the gamma-ray intensity of the different decay branches.*

as accurate intensities for the above 245 ns cannot be observed. Therefore, an isomeric ratio of 4.8(9)% for the $I^{\pi} = (22^{+})$ level has been obtained only from the 768 and 256 keV transitions.

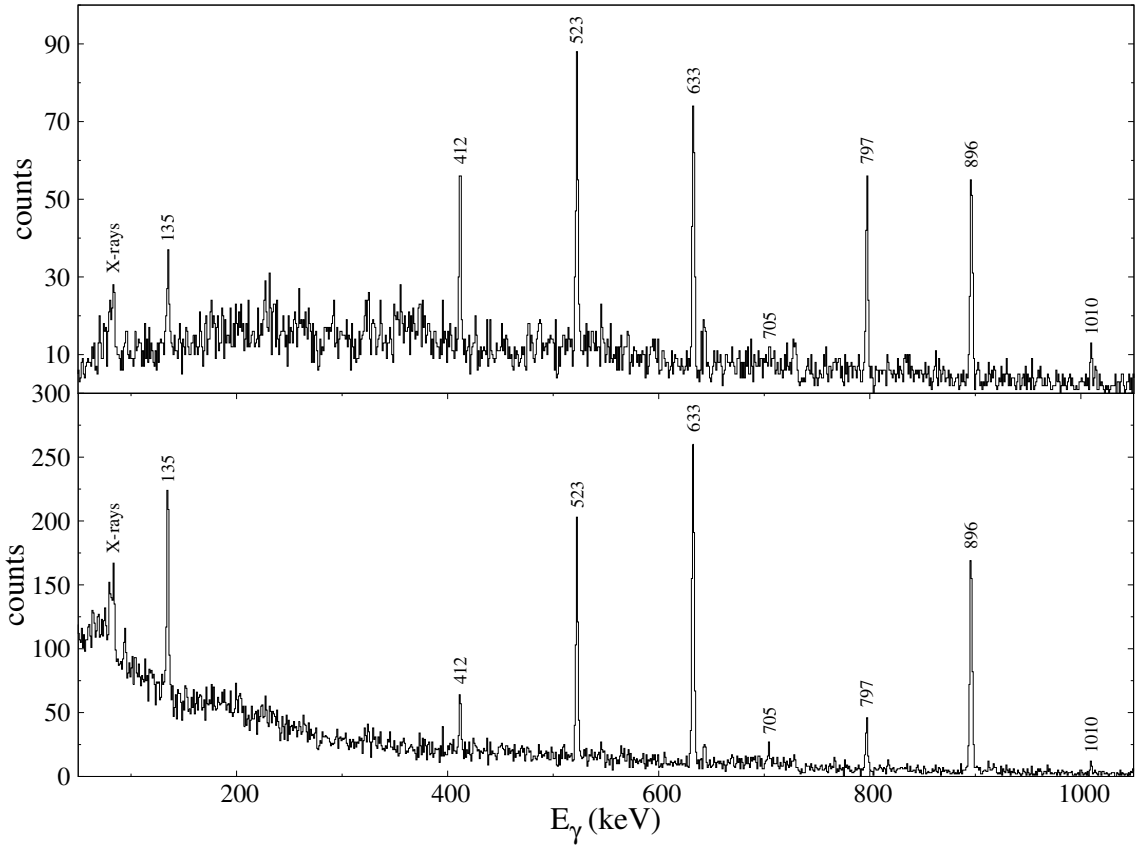

Figure 4.40: *The gamma-ray spectrum observed in coincidence with ^{213}Rn ions in the ^{212}Rn data set. Time gates of 1.4 and 12.7 μs have been used to produce the top and bottom spectra respectively.*

I^π	E_γ(keV)	M	α [72, 73]	I_γ	b	F	G	R_{exp} (%)
$(55/2^+)$	165	M1	3.15(5)		0.73			
	1053	[E3]	0.01719(24)		0.13			
	1423	[E3]	0.00896(13)		0.13			
	1010	E3	0.0189(13)	200(64)	0.93	0.797(9)	0.91(7)	1.0(3)
$(43/2^-)$	54	E2	149(4)		1			
	412	E1	0.01652(24)	614(118)	0.98	0.978(1)	0.18(8)	8(4)
$(31/2^-)$	523	E3	0.1073(15)	2013(208)	0.92	0.926(4)	0.50(2)	17(2)
$(25/2^+)$	<50		>245		1.00			
	135	E2	2.35(4)	1489(220)	0.99	0.964(8)	0.38(8)	9(7)
	633	E1	0.0069(1)	4611(397)	0.97	0.964(8)	0.38(8)	7(4)
	896	E3	0.025(4)	4214(377s)	0.94	0.964(8)	0.38(8)	5(4)

Table 4.21: *Relevant information for the calculation of the isomeric ratios of the $(55/2^+)$, $(43/2^-)$, $(31/2^-)$ and $(25/2^+)$ isomeric states in ^{213}Rn. The number of implanted ions was 30792.*

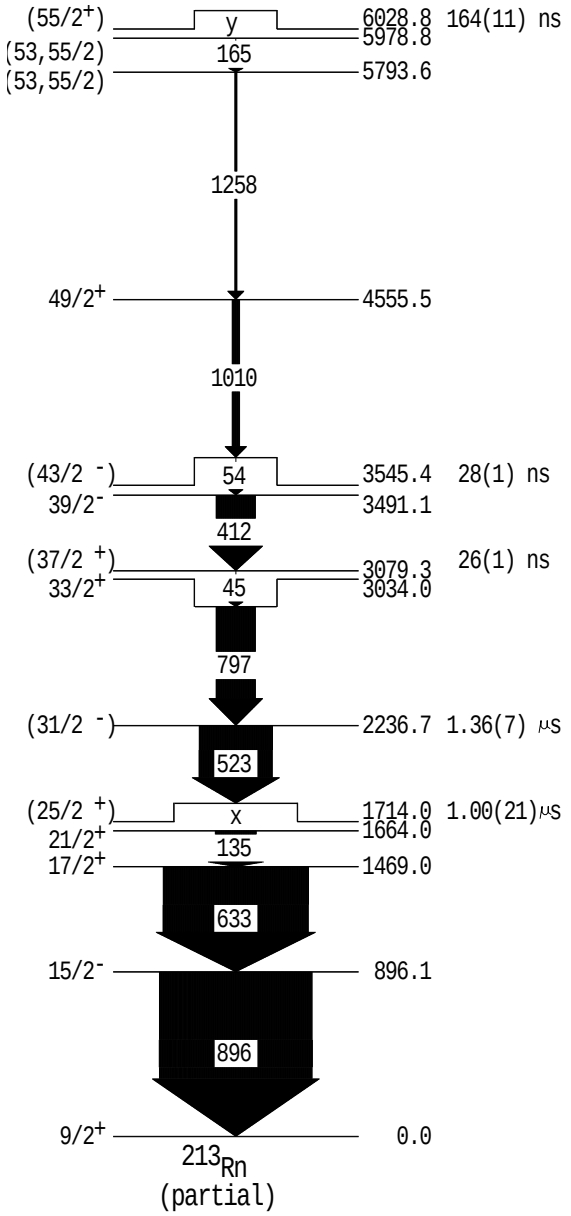

Figure 4.41: *A partial level scheme of ^{213}Rn, courtesy of Prof. G. Dracoulis. The width of the arrows is proportional to the gamma-ray intensity. Only the strongest decay branch is shown.*

I^{π}	E_{γ}(keV)	M	α [72, 73]	I_{γ}	b	F	G	R_{exp} (%)
(22^{+})	768	(M2)	0.1209(17)	259(57)	1.00	0.63(4)	0.86(6)	4.7(11)
	256	E1	0.048(7)	199(59)	0.83	0.63(4)	0.69(6)	5.0(16)

Table 4.22: *Relevant information for the calculation of the isomeric ratio of the (22^{+}), isomeric state in ^{214}Rn. The number of implanted ions was 11444.*

4.2.14 ^{208}Fr

Isomeric states in ^{208}Fr have been previously studied in [8, 108, 109]. The delayed gamma-ray spectrum and partial level scheme are shown in Figs. 4.44 and 4.45 respectively. A

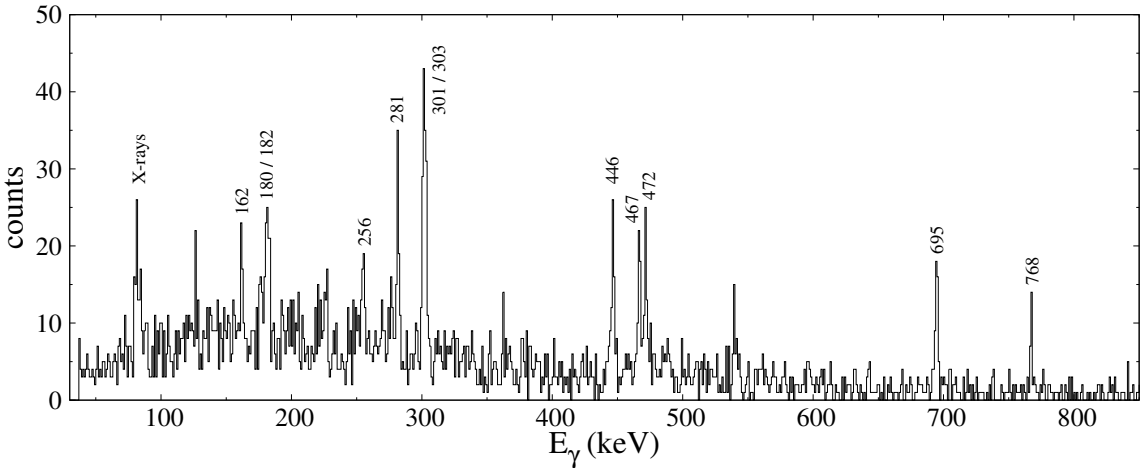

Figure 4.42: *The gamma-ray spectrum observed in coincidence with ^{214}Rn ions in the ^{212}Rn data set. A time gate of 1.6 μs has been used to produce the energy spectrum.*

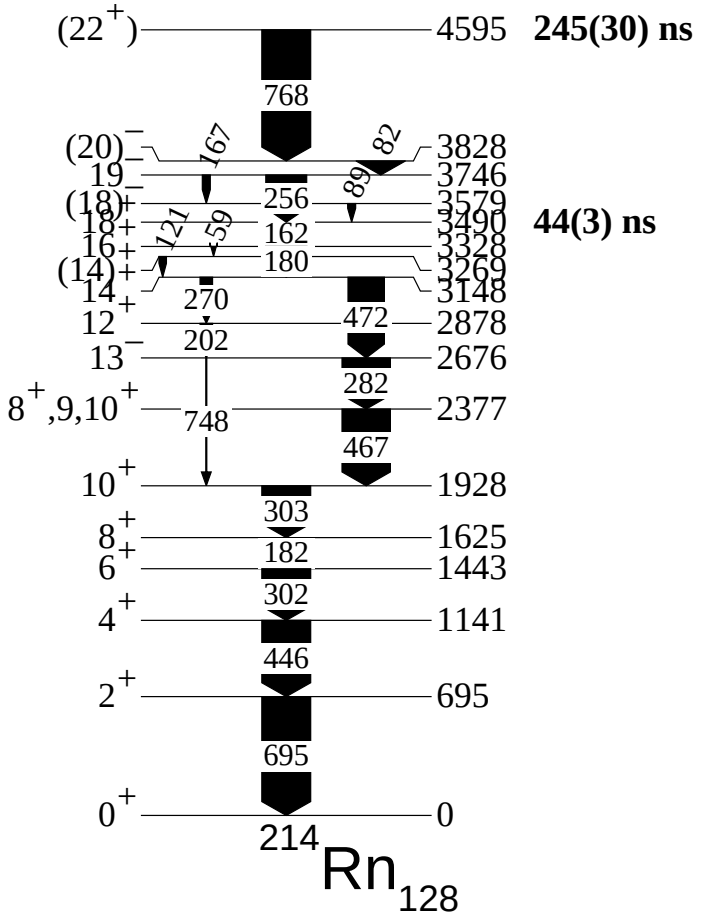

Figure 4.43: *A partial level scheme of ^{214}Rn. The width of the arrows is proportional to the total intensity of the different decay branches.*

time gate of 3.4 μs has been used to produce the energy spectrum. An isomer has been

observed at an excitation energy of 826 keV. The spin and half-life have proposed to be (10^-) and ∼200 ns in analogy with ^{206}At in [8], 10^- and 432(11) ns in [108] and 9^- and 233(18) ns in [109]. Due to conflicts with the spin and parity assignments in the latter case, the measurements from the second case have been used. The half-life measured in this experiment is 379(21) ns, in good agreement with the 432(11) ns measured in [108].

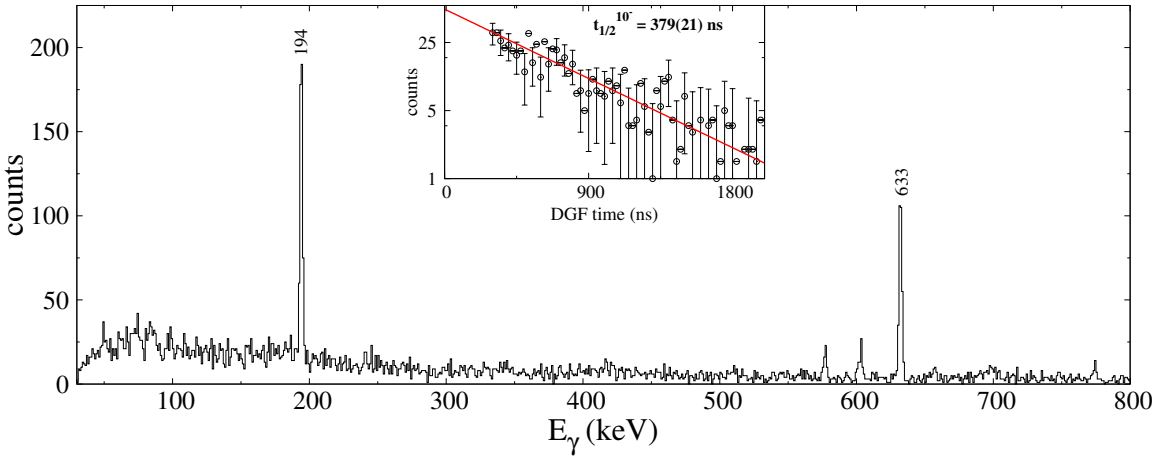

Figure 4.44: *The gamma-ray spectrum observed in coincidence with ^{208}Fr ions from the ^{214}Th data set. A time gate of 3.4 µs has been used.*

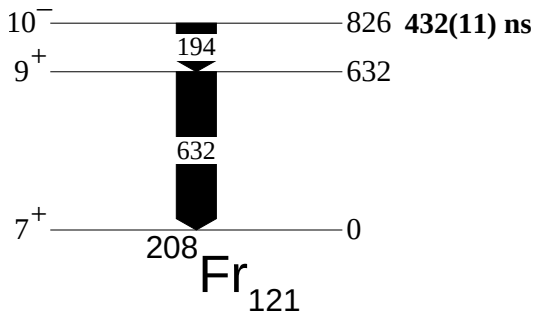

Figure 4.45: *A partial level scheme of ^{208}Fr. The width of the arrows is proportional to the gamma-ray intensity of the different decay branches.*

Table 4.23 shows the relevant information for the calculation of the isomeric ratios. An isomeric ratio of 16(1)% for the $I^\pi = 10^-$ level has been obtained only from the 194 and 632 keV transitions.

4.2.15 ^{213}Fr

Isomeric states in ^{213}Fr have been discussed in Section 4.1.5. The partial level scheme and delayed gamma-ray spectrum are shown in Figs. 4.12 and 4.46 respectively. A time

I^π	E_γ(keV)	M	α [72, 73]	I_γ	b	F	G	R_{exp} (%)
10^-	194	E1	0.0947(14)	2417(334)	1.00	0.766(5)	0.66(3)	17(2)
	632	E2	0.0217(3)	3191(291)	1.00	0.766(5)	0.92(4)	15(2)

Table 4.23: *Relevant information for the calculation of the isomeric ratio of the 10^-, isomeric state in ^{208}Fr. The number of implanted ions was 30906.*

gate of 4.6 μs has been used to produce the energy spectrum. Table 4.24 shows the relevant information for the calculation of the isomeric ratios. Isomeric ratios of 14(3)% and 16(3)% have been obtained for the $I^\pi = 29/2^+$ and $21/2^-$ levels respectively.

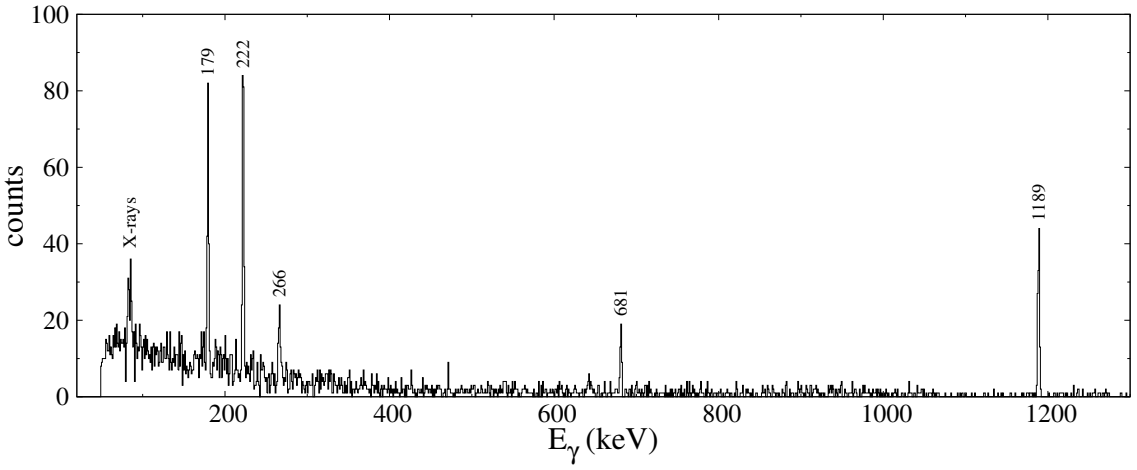

Figure 4.46: *The gamma-ray spectrum observed in coincidence with ^{213}Fr ions from the ^{212}Rn data set. A time gate of 4.6 μs has been used.*

I^π	E_γ(keV)	M	α [72, 73]	I_γ	b	F	G	R_{exp} (%)
$29/2^+$	681	E3	0.0529(8)	412(76)	1	0.601(8)	0.80(6)	14(3)
	265	M1+E2	0.6(4)	237(88)	1	0.601(8)	0.70(5)	14(7)
$21/2^-$	179	E2	0.823(12)	740(113)	1	0.871(3)	0.73(3)	15(6)
	222	E2	0.382(6)	1035(112)	1	0.871(3)	0.78(3)	15(4)
	1189	E2	0.00616(9)	1616(187)	1	0.871(3)	0.90(3)	16(5)

Table 4.24: *Relevant information for the calculation of the isomeric ratios of the $29/2^+$ and $21/2^-$ isomeric states in ^{213}Fr. The number of implanted ions was 6311.*

4.2.16 ^{214}Fr

Isomeric states in ^{214}Fr have been discussed in Section 4.1.6. The partial level scheme and delayed gamma-ray spectrum are shown in Figs. 4.13 and 4.47 respectively. A time gate of 1 μs has been used to produce the energy spectrum. Table 4.25 shows the relevant

information for the calculation of the isomeric ratios. An isomeric ratio of 69(13)% for the $I^{\pi} = 11^{+}$ level has been obtained.

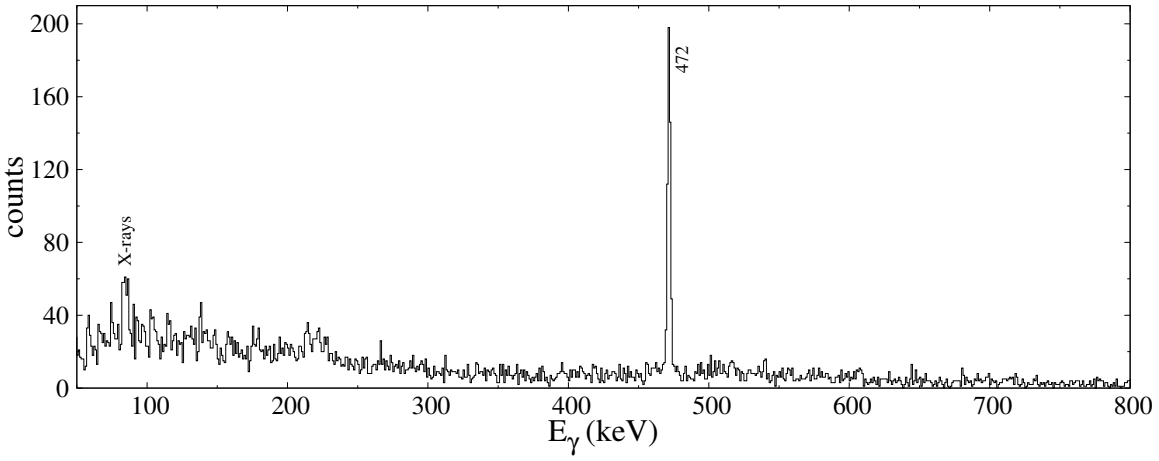

Figure 4.47: *The gamma-ray spectrum observed in coincidence with ^{214}Fr ions from the ^{212}Rn data set. A time gate of 1 μs has been used to produce the energy spectrum.*

I^{π}	E_{γ}(keV)	M	α [72, 73]	I_{γ}	b	F	G	R_{exp} (%)
11^{+}	472	M2	0.547(8)	3952(336)	0.97	0.35(4)	0.71(12)	69(13)

Table 4.25: *Relevant information for the calculation of the isomeric ratio of the 11^{+} isomeric state in ^{214}Fr. The number of implanted ions was 36334.*

4.2.17 ^{210}Ra

Isomeric states in ^{210}Ra have been previously studied in [110, 111]. The delayed gamma-ray spectrum and partial level scheme are shown in Figs. 4.48 and 4.49 respectively. A time gate of 15.3 μs has been used to produce the energy spectrum. An isomeric state at an excitation energy of 2050 keV has been observed in this experiment, with spin and parity 8^{+} and a measured half-life of 2.1(1) μs respectively, in good agreement with the previously published value of 2.4(1) μs [111]. The half-life measured in this work has been used for the calculations due to its better accuracy, as compared to previous measurements.

Table 4.26 shows the relevant information for the calculation of the isomeric ratios. An isomeric ratio of 31(2)% for the $I^{\pi} = 8^{+}$ level has been obtained.

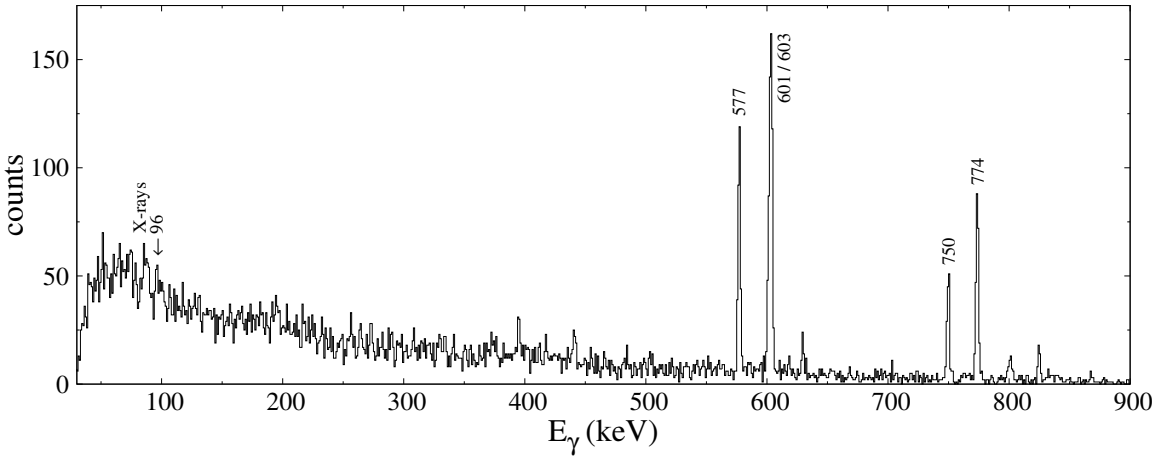

Figure 4.48: *The gamma-ray spectrum observed in coincidence with ^{210}Ra ions from the ^{214}Th data set. A time gate of 15.3 µs has been used.*

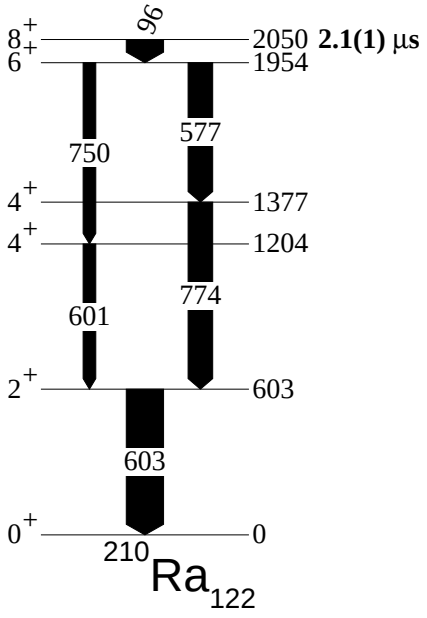

Figure 4.49: *A partial level scheme of ^{210}Ra. The width of the arrows is proportional to the total intensity of the different decay branches.*

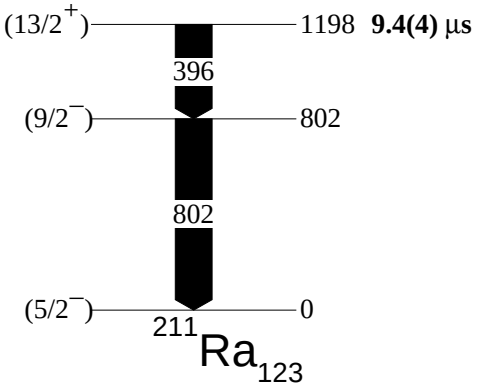

Figure 4.50: *A partial level scheme of ^{211}Ra. The width of the arrows is proportional to the total intensity of the different decay branches.*

I$^\pi$	E$_\gamma$(keV)	M	α [72, 73]	I$_\gamma$	b	F	G	R$_{exp}$ (%)
	750	E2	0.01590(23)	1482(182)	0.34	0.995	0.997(8)	31(4)
8$^+$	577	E2	0.0278(4)	2785(269)	0.66	0.995	0.997(8)	31(3)
	774	E2	0.01492(21)	2797(279)	0.66	0.995	0.997(8)	31(3)

Table 4.26: *Relevant information for the calculation of the isomeric ratio of the 8$^+$ isomeric state in ^{210}Ra. The number of implanted ions was 14360.*

4.2.18 ^{211}Ra

Isomeric states in ^{211}Ra have been previously studied in [8, 111, 112]. The partial level scheme and delayed gamma-ray spectrum are shown in Figs. 4.50 and 4.51 respectively. A time gate of 47.8 μs has been used to produce the energy spectrum. An isomeric state at an excitation energy of 1198 keV has been observed in this experiment with spin and parity $(13/2^+)$. Two values for the half-lives of this isomer have been suggested, 4.0(5) μs from [112] and 9.7(6) μs from [8]. A half-life of 9.4(4) μs has been observed from this data, in good agreement with the literature, as shown in the inset plot of Fig. 4.51, and this value has been used for the calculations.

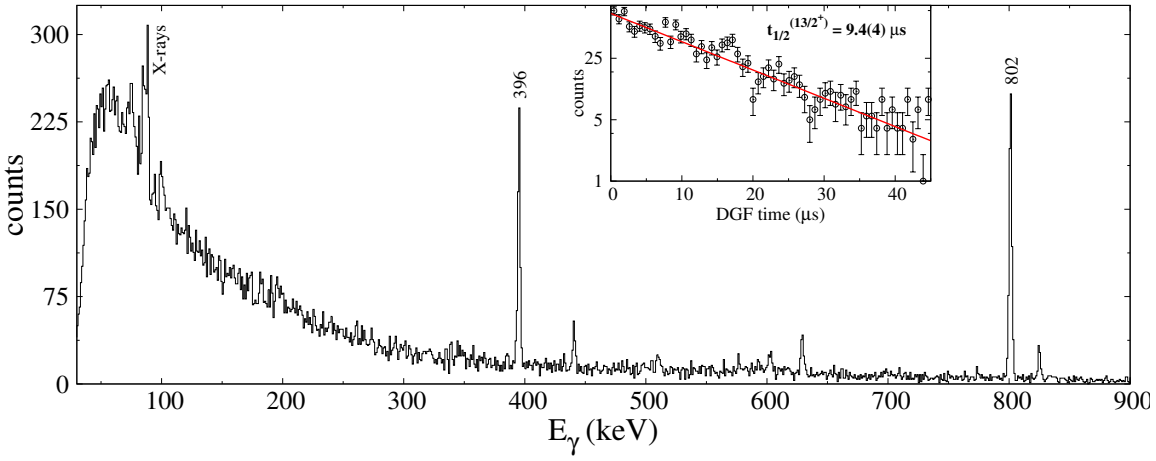

Figure 4.51: *The gamma-ray spectrum observed in coincidence with ^{211}Ra ions from the ^{214}Th data set. A time gate of 47.8 μs has been used.*

Table 4.27 shows the relevant information for the calculation of the isomeric ratios. An isomeric ratio of 35(2)% for the $I^\pi = (13/2^+)$ level has been obtained.

I^π	E_γ(keV)	M	α [72, 73]	I_γ	b	F	G	R_{exp} (%)
$(13/2^+)$	396	M2	1.015(15)	4238(371)	1.00	0.993(1)	0.963(2)	35(3)
	802	M2	0.01387(20)	8298(676)	1.00	0.993(1)	0.967(2)	34(3)

Table 4.27: *Relevant information for the calculation of the isomeric ratio of the $(13/2^+)$ isomeric state in ^{211}Ra. The number of implanted ions was 25426.*

4.2.19 ^{212}Ra

Isomeric states in ^{212}Ra have been previously studied in [111, 113]. The delayed gamma-ray spectrum and partial level scheme are shown in Figs. 4.52 and 4.54 respectively. Time

gates of 3 and 47.8 μs have been used to produce the upper and lower energy spectra in Fig. 4.52. Two isomeric states at excitation energies of 2613 and 1958 keV have been observed in this experiment. Half-lives of 0.85(13) and 10.9(4) μs have been proposed in [113] for the $(11)^-$ and $(8)^+$ isomeric states respectively. The half-lives measured from this experiment, and used for the calculation of the isomeric ratios, are 480(40) ns and 7.1(2) μs in disagreement with the published values in [113], but in agreement with those from [111]. The time spectra of both decays are shown in Fig. 4.53 along with the associated fit.

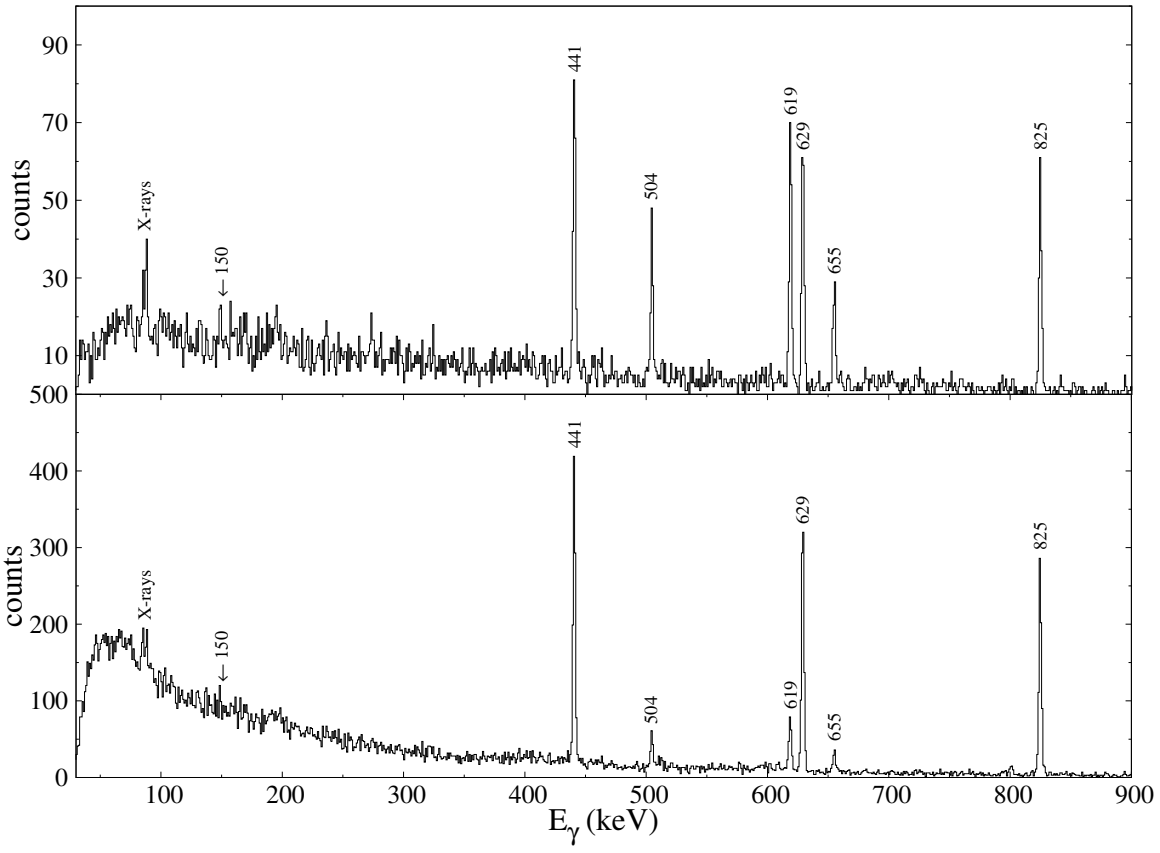

Figure 4.52: *The gamma-ray spectra observed in coincidence with ^{212}Ra ions from the ^{214}Th data set. Time gates of 3 and 47.8 μs has been used.*

Table 4.28 shows the relevant information for the calculation of the isomeric ratios. Isomeric ratios of 25(2)% and 18(2)% for the $I^\pi = (11)^-$ and $(8)^+$ levels have been obtained.

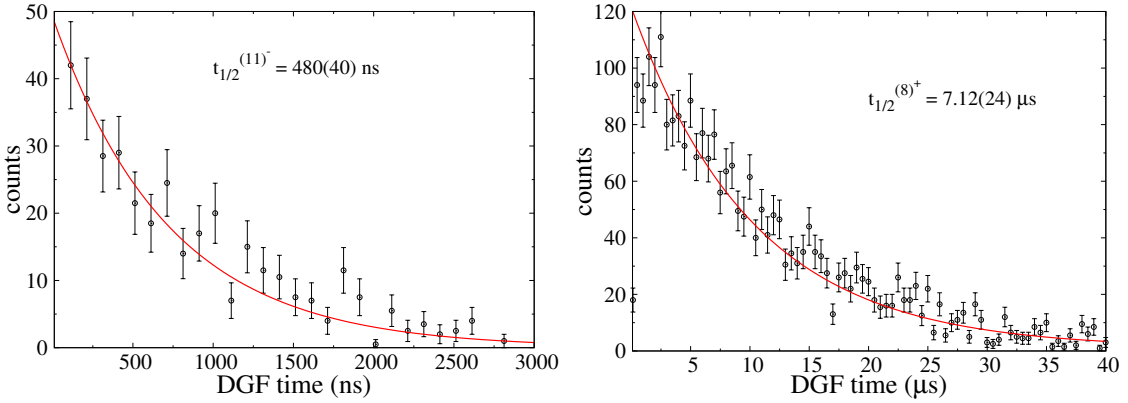

Figure 4.53: *Half-lives for the $(11)^-$ and $(8)^+$ isomeric states measured in this experiment.*

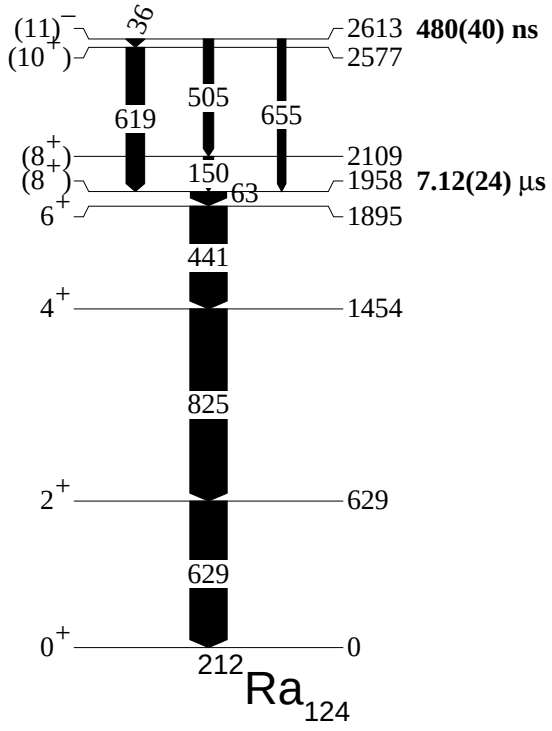

Figure 4.54: *A partial level scheme of ^{212}Ra. The width of the arrows is proportional to the total intensity of the different decay branches.*

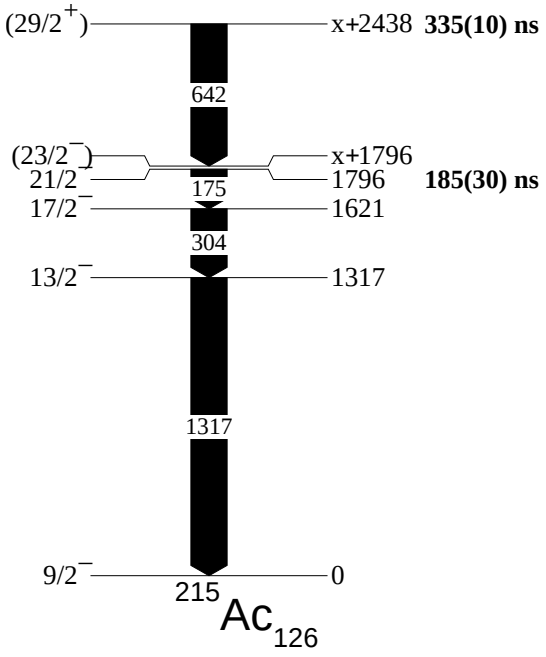

Figure 4.55: *A partial level scheme of ^{215}Ac. The width of the arrows is proportional to the total intensity of the different decay branches.*

4.2.20 ^{215}Ac

Isomeric states in ^{215}Ac have been previously studied in [114]. The partial level scheme and delayed gamma-ray spectrum are shown in Figs. 4.55 and 4.56 respectively. A time gate of 2.5 μs has been used to produce the energy spectrum. Two isomeric states at excitation energies of x + 2438 and 1796 keV have been observed in this experiment, with

I^π	E_γ(keV)	M	α [72, 73]	I_γ	b	F	G	R_{exp} (%)
$(11)^-$	36	[E1]	1.680(24)		0.50			
	505	(E3)	0.1353(19)	878(124)	0.28	0.840(4)	0.88(3)	26(4)
	655	(E3)	0.0625(9)	773(119)	0.23	0.840(4)	0.92(3)	25(4)
	619	(E2)	0.0238(4)	1748(181)	0.50	0.840(4)	0.92(3)	25(3)
$(8)^+$	63	[E2]	83.6(12)		1.00			
	441	E2	0.0526(8)	7295(590)	1.00	1.000	0.981(2)	16(4)
	825	E2	0.01311(19)	8889(715)	1.00	1.000	0.986(2)	23(4)
	629	E2	0.0230(4)	7623(612)	1.00	1.000	0.986(2)	17(4)

Table 4.28: *Relevant information for the calculation of the isomeric ratios of the $(11)^-$ and $(8)^+$ isomeric states in ^{212}Ra. The number of implanted ions was 19019.*

spins and parities of $(29/2^+)$ and $21/2^-$, and half-lives of 335(10) and 185(30) respectively.

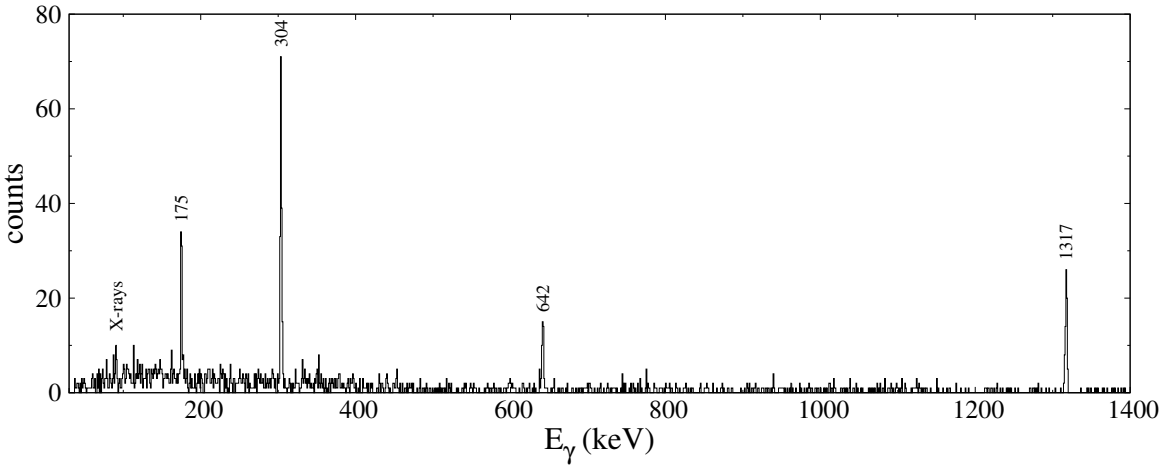

Figure 4.56: *The gamma-ray spectrum observed in coincidence with ^{215}Ac ions in the ^{214}Th data set. A time gate of 2.5 μs has been used.*

Table 4.29 shows the relevant information for the calculation of the isomeric ratios. Isomeric ratios of 20(4)% and 20(5)% have been obtained for the $I^\pi = (29/2^+)$ and $21/2^-$ levels respectively.

I^π	E_γ(keV)	M	α [72, 73]	I_γ	b	F	G	R_{exp} (%)
$(29/2^+)$	642	E3	0.0702(10)	481(81)	1.00	0.699(7)	0.90(5)	20(4)
$21/2^-$	1132(122)	E2	0.150(11)	170(14)	1.00	0.71(4)	0.76(8)	27(8)
	1317	E2	0.064(4)	1153(162)	1.00	0.71(4)	0.91(9)	15(7)

Table 4.29: *Relevant information for the calculation of the isomeric ratios of the $(29/2^+)$ and $21/2^-$ isomeric states in ^{215}Ac. The number of implanted ions was 4157.*

4.3 Summary of the values of the isomeric ratios

Table 4.30 summarises the isomeric ratios measured in this work. If results have been obtained from different data sets, the corresponding setting is indicated. The final column lists experimental isomeric ratios from literature for comparison. Results from this thesis have been obtained from projectile fragmentation of a 1 GeV/A ^{238}U beam on a ^{9}Be target, and results from [32] and [7] have been obtained from the same reaction with beam energies of 750 and 900 MeV/A respectively.

Concerning the isomeric ratios measured for the same nucleus in different data sets, the values measured in this work show varying levels of agreement, as follows:

- Data on ^{210}Rn show consistent results for the $(17)^{-}$ level, with isomeric ratios of 11(2)% and 10(1)%, while for the low spin state the isomeric ratio decreases from 29(3) to 14(2)% in the ^{213}Fr and ^{212}Rn data sets respectively. The ratio between the high and low spin isomeric ratios is different for the different data sets and the reason for this is unknown. This can be easily seen in the different relative intensities of the 644 and 564 keV transitions in Figs. 4.2 and 4.36.
- Data on ^{211}Rn show that the ratios between the $(35/2^{+})$ and $(17/2^{-})$ isomeric ratios are in agreement but the different absolute numbers could be due to different levels of contamination of implanted ions in the two ^{213}Fr and ^{212}Rn data sets.
- Data on ^{212}Fr show consistent isomeric ratios for the ^{213}Fr and ^{214}Ra data sets in the active stopper runs, with values of 16(1)% and 22(1)% for the (15^{-}) level (within three standard deviations) and 23(3)% and 20(2)% for the (11^{+}) level respectively.
- Data on ^{213}Fr show consistent isomeric ratios for the ^{212}Rn and ^{213}Fr data sets, with values of 14(3)% and 16(3)% for the $29/2^{+}$ level and 23(2)% and 22(2)% for the $21/2^{-}$ level respectively.
- Data on ^{214}Fr show consistent isomeric ratios for the ^{212}Rn and ^{213}Fr data sets, with values of 69(13)% and 70(14)% for the (11^{+}) level respectively.

Nucleus[Data set]	$\mathbf{I}^{\pi}$(%)	$\mathbf{E}_{lev}$ **(keV)**	$\mathbf{t}_{1/2}$ **(μs)**	$\mathbf{R}_{exp}$ **(%)**	$\mathbf{R}_{exp}^{previous}$ **(%)**
^{198}Po	12^{+}	x+2692	0.75(5)	4(2)	8.9(12) [32]
	11^{-}	2566	0.20(2)	20(9)	
^{200}Po	12^{+}	x+2804	0.268(3)	7(3)	6.7(12) [32]
	11^{-}	2596	0.10(1)	46(20)	39.3(41) [32]

Continued on the next page

Table 4.30 –continued from previous page

Nucleus [Data set]	$\mathbf{I}^{\pi}(\%)$	$\mathbf{E}_{lev}$ **(keV)**	$\mathbf{t}_{1/2}$ **(μs)**	$\mathbf{R}_{exp}$ **(%)**	$\mathbf{R}_{exp}^{previous}$ **(%)**
^{206}Po	9^-	2262	1.05(6)	15(2)	
	8^+	1586	0.232(4)	12(2)	
^{208}Po	8^+	1528	0.35(2)	27(2)	
^{208}At	16^-	2276	1.5(2)	8.6(9)	
^{209}At	$(29/2)^+$	2429	0.89(4)	17(1)	
^{210}At	19^+	4028	5.66(7)	8.9(9)	
	15^-	2550	0.482(6)	5.2(7)	
^{211}At	$39/2^-$	4814	4.2(4)	6.6(4)	
^{210}Rn [^{212}Rn]	$(17)^-$	x+3812	1.06(5)	10(1)	
	(8^+)	x+1665	0.644(40)	14(2)	
^{210}Rn [^{213}Fr]	$(17)^-$	x+3812	0.106(5)	11(2)	
	(8^+)	x+1665	0.644(40)	29(3)	
^{211}Rn [^{212}Rn]	$(35/2^+)$	x+3926	0.0402(14)	10(2)	
	$(17/2^-)$	x+1578	0.596(28)	26(2)	
^{211}Rn [^{213}Fr]	$(35/2^+)$	x+3926	0.0402(14)	14(3)	
	$(17/2^-)$	x+1578	0.596(28)	38(3)	
^{212}Rn	22^+	6174	0.109(5)	3.4(5)	
	8^+	1694	0.910(30)	34(2)	
^{213}Rn	$(55/2^+)$	y+5929	0.164(11)	1.0(3)	
	$(43/2^-)$	x+3495	0.028(1)	8(4)	
	$(31/2^-)$	x+2187	1.36(7)	17(2)	
	$(25/2^+)$	x+1664	1.00(21)	6(3)	
^{214}Rn	(22^+)	4525	0.245(30)	4.8(9)	
^{208}Fr	10^-	826	0.432(11)	16(1)	
^{211}Fr	$(45/2^-)$	4657	0.123(14)	2.4(2)	
	$(29/2^+)$	2423	0.146(14)	16(1)	5.7(19) [7]
^{212}Fr [^{213}Fr]	(15^-)	2492	0.577(19)	16(1)	7.5(18) [7]
	(11^+)	1551	31.9(7)	23(3)	
^{212}Fr [^{214}Ra]	(15^-)	2492	0.577(19)	22(1)	7.5(18) [7]
	(11^+)	1551	31.9(7)	20(2)	

Continued on the next page

Table 4.30 –continued from previous page

Nucleus [Data set]	$\mathbf{I}^{\pi}(\%)$	$\mathbf{E}_{lev}$ **(keV)**	$\mathbf{t}_{1/2}$ **(μs)**	$\mathbf{R}_{exp}$ **(%)**	$\mathbf{R}_{exp}^{previous}$ **(%)**
^{213}Fr [^{213}Fr]	$29/2^{+}$	2538	0.238(6)	23(2)	12(8)[7]
	$21/2^{-}$	1590	0.504(14)	22(2)	
^{213}Fr [^{212}Rn]	$29/2^{+}$	2538	0.238(6)	14(3)	12(8)[7]
	$21/2^{-}$	1590	0.504(14)	16(3)	
^{214}Fr [^{213}Fr]	(11^{+})	638	0.103(4)	70(14)	
^{214}Fr [^{212}Rn]	(11^{+})	638	0.103(4)	69(13)	
^{210}Ra	8^{+}	2050	2.1(1)	31(2)	
^{211}Ra	$(13/2^{+})$	1198	9.4(4)	35(2)	
^{212}Ra	$(11)^{-}$	2613	0.48(4)	25(2)	
	$(8)^{+}$	1958	7.12(24)	18(2)	
^{214}Ra	17^{-}	4147	0.225(4)	13(1)	6.8(23) [7]
	14^{+}	3478	0.279(4)	13(1)	
	8^{+}	1865	67.3(15)	64(2)	
^{215}Ra	$(43/2^{-})$	x+3757	0.555(10)	7.9(8)	3.1(6) [7]
^{215}Ac	$(29/2^{+})$	x+2438	0.335(10)	20(4)	4.8(12) [7]
	$21/2^{-}$	1796	0.185(30)	20(5)	

Table 4.30: *Summary of calculated isomeric ratios ordered by increasing mass and nuclear charge. If the calculation has been done for the same nucleus in more than one data set, the setting is indicated in the brackets. Isomeric ratios from the literature are also included, and the corresponding reference is given.*

Fig. 4.57 shows the experimental isomeric ratios calculated in this thesis compared with previously published values for ^{198}Po, ^{200}Po, ^{211}Fr, ^{212}Fr, ^{213}Fr, ^{214}Ra, ^{215}Ra and ^{215}Ac [7, 32]. It can be seen that:

- Only the isomeric ratio for the higher-lying level in ^{198}Po has been given in [32], with a value of 8.9(12)%, which agrees within two standard deviations with the 4(2)% isomeric ratio measured in this work.
- The results from [32] on ^{200}Po are in agreement with those of this work, giving isomeric ratios of 6.7(12)% and 39.3(41)% for the 12^{+} and 11^{-} levels compared to 7.2(26)% and 46(22)% respectively.

- Larger discrepancies have been found with the data from [7], where isomeric ratios of 5.7(19)%, 7.5(18)%, 12(8)%, 6.8(23)%, 3.1(6)% and 4.8(12)% have been given compared to the isomeric ratios measured in this work, 16(1)%, 21(2)%, 20(2)%, 13(1)%, 7.9(8)% and 20(4)% for ^{211}Fr, ^{212}Fr, ^{213}Fr, ^{214}Ra, ^{215}Ra and ^{215}Ac respectively.

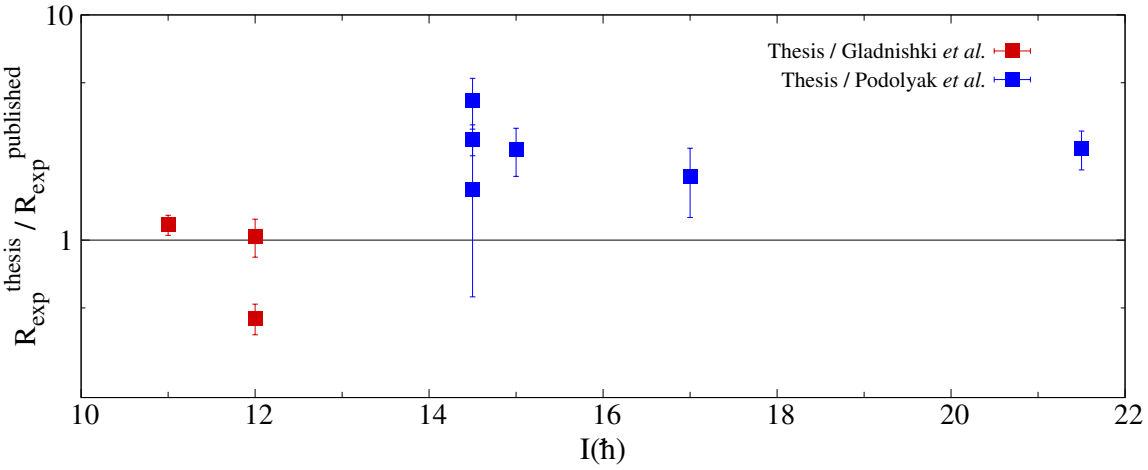

Figure 4.57: *Ratio between the experimental isomeric ratios calculated in this thesis and previously published values as a function of the spin of the isomer states for ^{198}Po, ^{200}Po, ^{211}Fr, ^{212}Fr, ^{213}Fr, ^{214}Ra, ^{215}Ra and ^{215}Ac. The blue and red points correspond to the comparison with results from [7] and [32] respectively.*

Figs. 4.58 and 4.59 show the experimental isomeric ratios plotted as a function of the energy and spin of the isomeric states respectively, where it is shown that the population probability decreases as the energy and spin of the isomeric state increases. When more than one isomeric ratio has been calculated for the same level, a weighted average of the values has been used, and when the energy of the level is unknown, x and y have been set to zero.

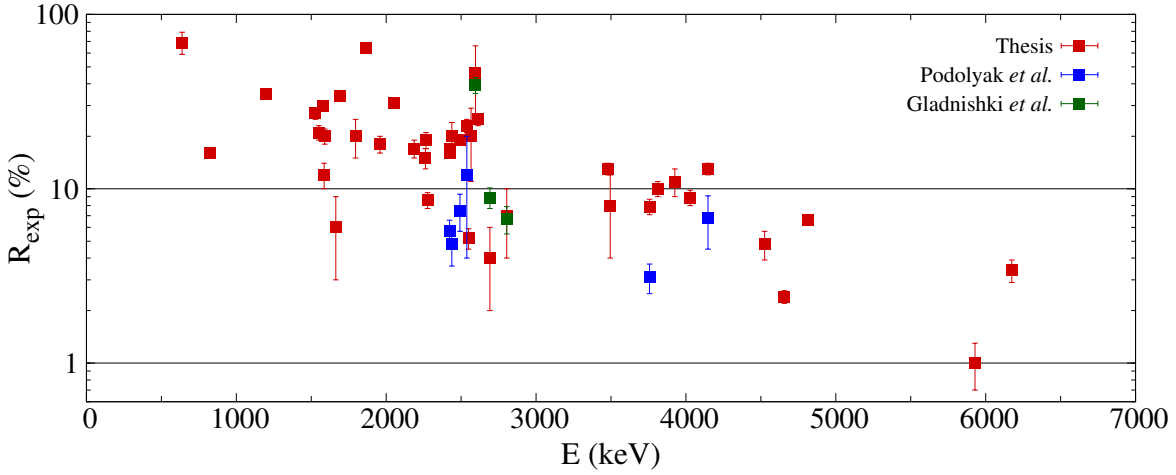

Figure 4.58: *Experimental isomeric ratios as a function of the energy of the level of the isomeric states. The red points correspond to the data obtained in this work, and the blue and green points correspond to results from the literature [7, 32] respectively.*

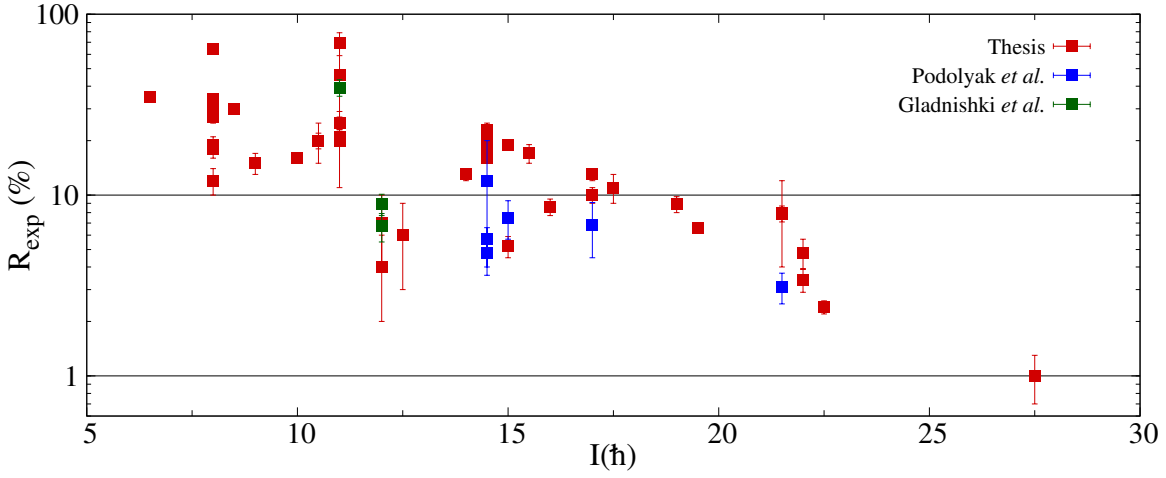

Figure 4.59: *Experimental isomeric ratios as a function of the spin of the isomer states. The red points correspond to the data obtained in this work, and the blue and green points correspond to results from the literature [7, 32] respectively.*

Chapter 5

Interpretation and conclusions

The experimentally calculated isomeric ratios have been compared with the theoretical values calculated using Eqs. 1.11 and 1.18 for the spin cut-off parameter and theoretical isomeric ratios respectively. Tables 5.1 and 5.2 show the experimental and theoretical isomeric ratios and the ratio between the two, in order of increasing spin for the isomeric states presented in this thesis, and from the literature, respectively. Also the mass of the fragment and the calculated cut-off parameter are indicated.

$\mathbf{I}(\hbar)$	$\mathbf{A}_f$	σ_f^2	ρ_{theo} (%)	$\mathbf{R}_{exp}$ (%)	$\mathbf{R}_{exp}/\rho_{theo}$
6.5	211	55	64.40	35(2)	0.54(3)
8	206	64	71.92	12(2)	0.17(3)
8	208	60	54.83	27(2)	0.49(4)
8	210	56	52.80	19(2)	0.36(4)
8	212	52	49.77	34(2)	0.68(4)
8	210	57	53.39	31(2)	0.58(4)
8	212	53	50.57	18(2)	0.36(4)
8	214	48	46.87	64(2)	1.37(4)
8.5	211	54	47.21	30(2)	0.64(4)
9	206	64	49.34	15(2)	0.30(4)
10	208	63	41.55	16(1)	0.39(2)
10.5	213	49	29.47	20(2)	0.7(1)
10.5	215	46	26.79	20(5)	0.7(2)
11	198	78	42.80	20(9)	0.5(2)
11	200	74	40.81	46(20)	1.1(5)
11	212	52	28.02	21(2)	0.7(1)
11	214	47	24.70	69(10)	2.8(4)

Continued on the next page

Table 5.1 –continued from previous page

$\mathbf{I}(\hbar)$	$\mathbf{A}_f$	σ_f^2	ρ_{theo} (%)	$\mathbf{R}_{exp}$ (%)	$\mathbf{R}_{exp}/\rho_{theo}$
11	212	53	28.65	25(2)	0.9(1)
12	198	78	36.68	4(2)	0.1(1)
12	200	74	34.68	7(3)	0.2(1)
12.5	213	50	18.67	6(3)	0.3(2)
14	214	48	10.97	13(1)	1.2(1)
14.5	209	59	14.71	17(1)	1.2(1)
14.5	211	55	12.84	16(1)	1.2(1)
14.5	213	49	10.29	20(2)	1.9(2)
14.5	215	46	8.62	20(4)	2.3(5)
15	210	56	11.76	5.2(7)	0.4(1)
15	212	52	9.89	19(1)	1.9(1)
15.5	213	50	7.86	17(2)	2.2(3)
16	208	61	10.73	8.6(9)	0.8(1)
17	210	56	6.62	10(1)	1.5(2)
17	214	48	3.99	13(1)	3.3(3)
17.5	211	54	4.93	11(2)	2.2(4)
19	210	56	3.38	8.9(9)	2.6(3)
19.5	211	53	2.34	6.6(4)	2.8(2)
21.5	213	50	0.81	8(4)	9.8(9)
21.5	215	46	0.54	7.9(8)	14(2)
22	212	52	0.74	3.4(5)	4.6(7)
22	214	48	0.49	4.8(9)	10(2)
22.5	211	55	0.80	2.4(2)	3.0(3)
27.5	213	50	0.04	1.0(3)	24(7)

Table 5.1: *Summary of the experimental and theoretical isomeric ratios ordered by increasing spin. The theoretical isomeric ratios have been calculated using the analytical approximation of the abrasion-ablation code (Eqs.1.11 and 1.18).*

Table 5.2 shows the ratios between experimental and theoretical isomeric ratios with the theoretical values calculated using the ABRABLA code ($\rho_{theo}^{ABRABLA}$) and the analytical formula (ρ_{theo}), showing how the difference between the values calculated using the Monte Carlo calculations vary between 6 and 61% with respect to the results of the analytical formula.

$\mathbf{I}(\hbar)$	$\mathbf{A}_f$	$\rho_{theo}^{ABRABLA}$ (%)	ρ_{theo} (%)	$\mathbf{R}_{exp}$ (%)	$\mathbf{R}_{exp}/\rho_{theo}^{ABRABLA}$	$\mathbf{R}_{exp}/\rho_{theo}$
11	200	27.5	40.81	39.3(41)	1.4(1)	1.0(1)
12	198	20.0	36.70	8.9(12)	0.45(3)	0.24(3)
12	200	22.2	34.90	6.7(12)	0.30(3)	0.19(3)
14.5	211	9.4	12.84	5.7(9)	0.6(1)	0.44(7)
14.5	213	11.1	10.29	12(8)	1.1(8)	1.2(8)
14.5	215	3.8	8.62	4.8(12)	1.3(1)	0.6(1)
15	212	8.5	9.89	7.5(18)	0.9(2)	0.8(2)
17	214	2.4	3.99	6.8(23)	2.8(6)	1.7(6)
21.5	215	0.21	0.54	3.1(6)	15(1)	6(1)

Table 5.2: *Summary of the experimental and theoretical isomeric ratios ordered by increasing spin from the previously published data [7, 32]. The theoretical isomeric ratios have been calculated using the ABRABLA Monte Carlo code ($\rho_{theo}^{ABRABLA}$) and also using the analytical formula (ρ_{exp}) have been included.*

Figs. 5.1 and 5.2 show the ratios between the experimental and the theoretical isomeric ratios plotted as a function of the energy and spin of the isomeric states, respectively. The theoretical isomeric ratios calculated using the sharp cut-off approximation, represent an upper limit and therefore the ratio between experimental and theoretical values is expected to be equal or less than one. This approximation is justified for isomers lying close to the yrast line [13]. Due to the assumption that all the states above the isomer of interest decay into this isomer, the high-spin states are better probe to test the theory. Also, when more than one isomer are populated in a nucleus, the experimental isomeric ratio might not be directly comparable with the theoretical calculation if there are transition which do not decay into the lower spin isomer. Therefore, the same figures are shown in Figs. 5.3 and 5.4, including only the highest spin state (when more than one isomer are populated) in each nuclei.

The data shows that the ratio between the experimental and theoretical isomeric ratio is larger than one for spins greater than $17\hbar$, and increases with spin, suggesting that the abrasion-ablation model underestimates the population of high-spin states produced in projectile fragmentation reaction. This increasing ratio was previously seen in [7], where ratios of 2.8(1.0) and 15(3)% for isomeric states with $I^{\pi}=17^{-}$ and $43/2^{-}$ were measured. Fig. 5.5 show that the larger ratios are obtained for isomer with half-lives ranging from 100 to 600 ns. It also shown A comparison between Figs. 1.4 and 5.2/5.4, show that this work has extended the available data for spins higher than $17\hbar$ from two to ten data points.

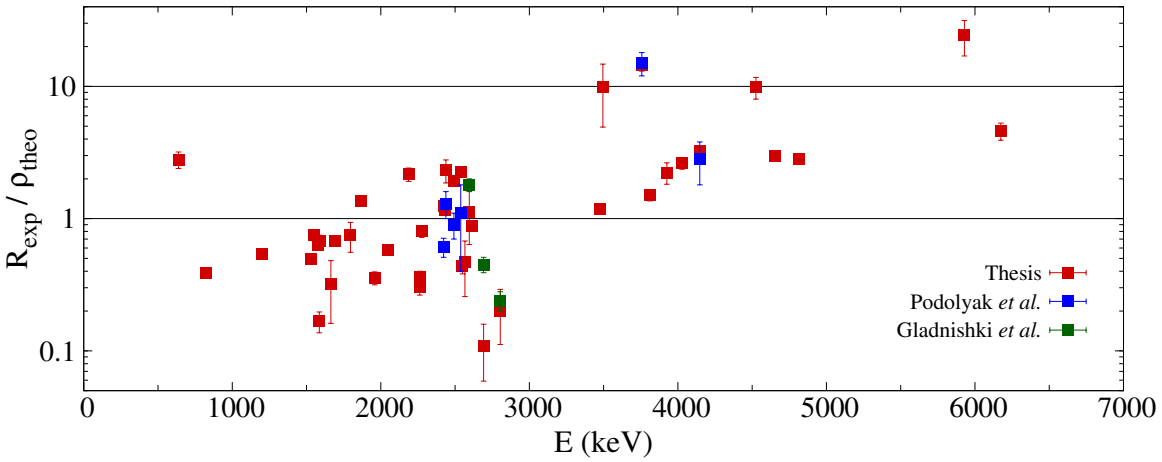

Figure 5.1: *Ratios between experimental and calculated isomeric ratios as a function of the excitation energy of the isomeric state. The red points correspond to the data obtained in this work, where the theoretical isomeric ratios have been calculated using Eqs.1.11 and 1.18. The blue and green points correspond to results from the literature [7, 32] respectively, where the ABRABLA code has been used for the theoretical calculations.*

All the experimental isomeric ratios obtained in this work have been compared with the results of applying the analytical formula, but as seen in Table 5.2, this simple calculation can be between 8 and 61% different from that calculated using ABRABLA code. Therefore more calculations using the Monte Carlo code should be done in the future to test the validity of the approximation.

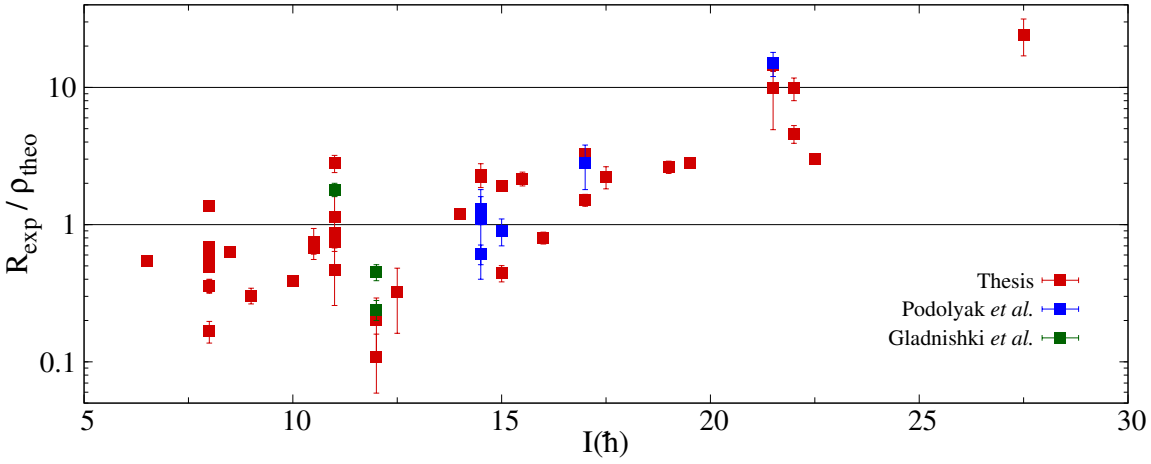

Figure 5.2: *Ratios between experimental and calculated isomeric ratios as a function of the spin of the isomeric state. The red points correspond to the data obtained in this work, where the theoretical isomeric ratios have been calculated using Eqs.1.11 and 1.18. The blue and green points correspond to results from the literature [7, 32] respectively, where the ABRABLA code has been used for the theoretical calculations.*

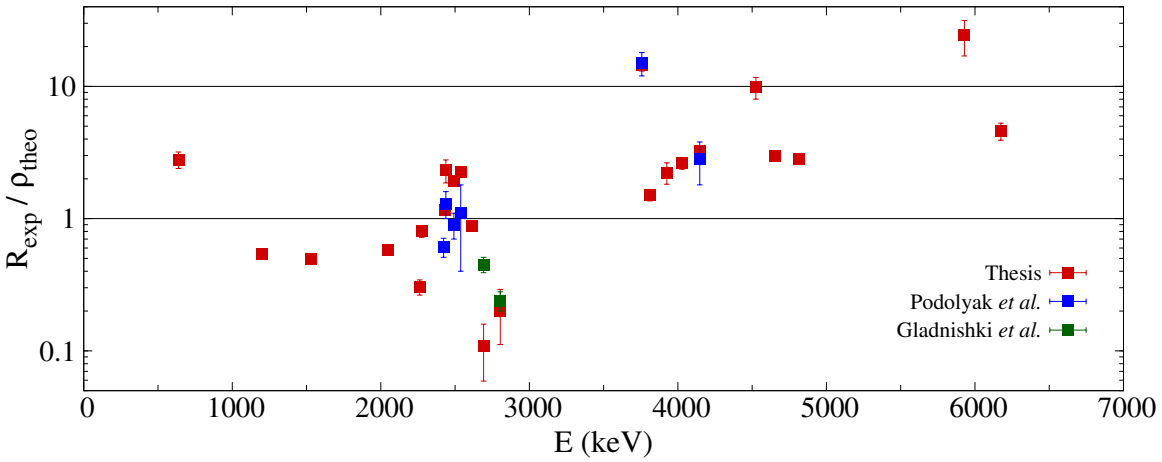

Figure 5.3: *Ratios between experimental and calculated isomeric ratios as a function of the excitation energy of the isomeric state, only for the highest spin-state of each nuclei. The red points correspond to the data obtained in this work, where the theoretical isomeric ratios have been calculated using Eqs.1.11 and 1.18. The blue and green points correspond to results from the literature [7, 32] respectively, where the ABRABLA code has been used for the theoretical calculations.*

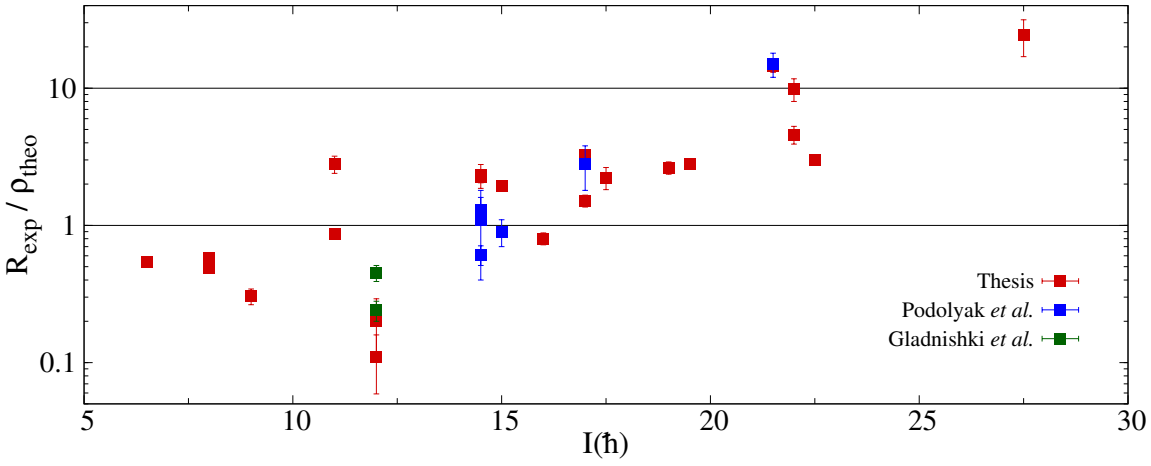

Figure 5.4: *Ratios between experimental and calculated isomeric ratios as a function of the spin of the isomeric state, only for the highest spin-state of each nuclei. The red points correspond to the data obtained in this work, where the theoretical isomeric ratios have been calculated using Eqs.1.11 and 1.18. The blue and green points correspond to results from the literature [7, 32] respectively, where the ABRABLA code has been used for the theoretical calculations.*

Other studies of the isomeric ratio have been carried out in different regions of the nuclear chart [115], with fragment masses between 142 and 152, using projectile fragmentation of a 1 GeV/A ^{208}Pb beam on a ^{9}Be target. In this case, the ratio between the experimental and theoretical isomeric ratios does not show any increase with spin and as expected, the theoretical calculation is larger than the measured isomeric ratio.

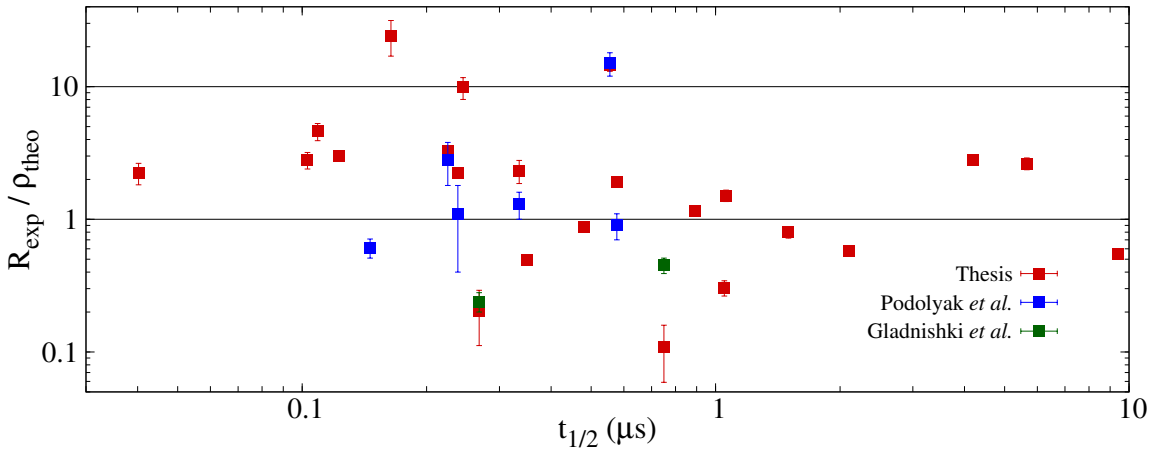

Figure 5.5: *Ratios between experimental and calculated isomeric ratios as a function of the half-life of the isomeric state, only for the highest spin-state of each nuclei. The red points correspond to the data obtained in this work, where the theoretical isomeric ratios have been calculated using Eqs.1.11 and 1.18. The blue and green points correspond to results from the literature [7, 32] respectively, where the ABRABLA code has been used for the theoretical calculations.*

The experimental isomeric ratios calculated in this work will be a valuable tool to test the abrasion-ablation model and other theories of fragmentation reactions. From the 24 nuclei studied in this work, inconsistencies have been found in two nuclei which were measured in two different data sets, where the isomeric ratios agree within two and three standard deviations. This can be attributed to the precision with which the efficiency calibration was done. As mentioned in Chapter 2, the efficiency calibration was carried out only for the settings in the active stopper configuration. The efficiency for the data sets in the passive stopper configuration, where the stopper was offset from the centre of the RISING array, was obtained from Geant4 Monte Carlo simulations. Another quantity to which the experimental isomeric ratio is sensitive to, is the number of implanted ions, decreasing its value if the nuclei identification is not sufficiently clean from neighbouring nuclei and other background contamination. This effect can only make the ratio between experimental and theoretical isomeric ratios increase, giving confidence in the validity of the large ratios obtained for spins larger than 17$\hbar$. Nevertheless, special attention should be taken in the future to obtain a quantitatively accurate efficiency calibration and a clean identification of the nuclei of interest when isomeric ratios need to be obtained. Also, when measuring states with short half-lives and transitions with energies lower than 150 keV, the use of more precise analogue timing could help achieving more accurate results.

Attempts have been made to explain the underestimation of the population of high spin states in the abrasion-ablation model. Podolyák *et al* [7] have suggested a collective contribution to the angular momentum, arising from a shift in the longitudinal momentum when nucleons are removed from the periphery of the projectile during the collision. Modifications of the abrasion-ablation model, such as the ART-SBD model [35], have tried to obtain a better agreement between theory and experiment by considering the abrasion stage in the framework of a relativistic transport model and the ablation stage as a sequential binary decay. A new version of the ABRABLA code has been developed at GSI, where the ablation stage also contributes to the angular momentum. As part of future work, the experimental isomeric ratios obtained in this work, can be compared with the predictions of all this different models. It would also be interesting to compare these theories with other experimental isomeric ratios from other mass regions and different projectile-target combinations and beam energies. However, the number of studies published in this area is limited to only few [7, 32, 115]. The results of this work and future measurements on isomeric ratios will be of great interest for the production of radioactive beams in an isomeric state for the future nuclear physics facilities such as FAIR.

References

[1] C. A. Bertulani and P. Danielewicz, *Introduction to Nuclear Reactions.* (CRC Press, 2004).

[2] H. Geissel *et al.*, Annu. Rev. Nucl. Part. Sci. , 163 (1995).

[3] A. S. Botvina and L. N. Mishustin, Phys. Lett. **B584**, 233 (2004).

[4] K.-H. Schmidt *et al.*, Nucl. Phys. **A701**, 115 (2002).

[5] J. Benlliure *et al.*, Nucl. Phys. **A660**, 87 (1999).

[6] T. Enqvist *et al.*, Nucl. Phys. **A658**, 47 (1999).

[7] Z. Podolyák *et al.*, Phys. Lett. **B632**, 203 (2006).

[8] Z. Podolyák *et al.*, AIP Conf. Proc. **831**, 114 (2006).

[9] Z. Podolyák, Acta Phys. Pol. **B36**, 1269 (2006).

[10] A. M. Denis Bacelar *et al.*, Acta Phys. Pol. **B40**, 889 (2009).

[11] G. M*ü*nzenberg, Nucl. Instr. and Meth. **B70**, 265 (1992).

[12] J.-J. Gaimard and K.-H. Schmidt, Nucl. Phys. **A531**, 709 (1991).

[13] M. de Jong, A. Ignatyuk, and K.-H. Schmidt, Nucl. Phys. **A613**, 435 (1997).

[14] R. Serber, Phys. Rev. **72**, 1114 (1947).

[15] A. A. Amsden, Phys. Rev. **C15**, 2059 (1977).

[16] A. A. Amsden, Phys. Rev. **C17**, 2080 (1978).

[17] K. Asahi *et al.*, Phys. Lett. **B251**, 488 (1990).

[18] H. Okuno *et al.*, pl **B335**, 29 (1994).

[19] N. Metropolis, R. Bivins, and M. Storm, Phys. Rev. **110**, 185,204 (1958).

[20] J. P. Bondorf *et al.*, Z. Phys. **A279**, 385 (1976).

[21] J. D. Stevenson, Phys. Rev. Lett. **41**, 1702 (1978).

[22] H. H*ü*fner, K. Sch*ä*fer, and B. Sch*ü*rmann, Phys. Rev. **C12**, 1888 (1975).

[23] J. Bowman, W. Swiatecki, and C. F. Tsang, Lawrance Berkeley Laboratory **Report LBL-2908** (1973).

[24] A. A. Ross, H. Mark, and R. D. Lawson, Phys. Rev. **102**, 1613 (1956).

[25] K.-H. Schmidt *et al.*, Z. Phys **A308**, 215 (1982).

[26] A. S. Goldhaber, Phys. Lett. **B53**, 306 (1974).

[27] A. V. Ignatyuk and Y. V. Sokolov, Sov. J. Nucl. Phys. **28**, 469 (1978).

[28] X. Campi and J. Hufner, Z. Phys **A308**, 215 (1982).

[29] G. Bertsch, Z. Phys. **A289**, 103 (1978).

[30] W. Nöremberg, Nucl. Phys. **A482**, 221 (1988).

[31] K.-H. Schmidt *et al.*, Nucl. Phys. **A452**, 699 (1992).

[32] K. Gladnishki *et al.*, Phys. Rev. **C69**, 024617 (2004).

[33] M. Pfützner *et al.*, Phys. Lett. **B444**, 32 (1998).

[34] M. Pfützner *et al.*, Phys. Rev. **C65**, 064604 (1994).

[35] S. Pal and R. Palit, Phys. Lett. **B665**, 164 (2008).

[36] O. Tarasov and D. Bazin, Nucl. Phys. **A746**, 411 (1992).

[37] Deformation calculator, `http://t2.lanl.gov/data/astro/molnix96/massd.html`, Site visited: 2010.

[38] H. J. Wollersheim *et al.*, Nucl. Instr. and Meth. **A537**, 637 (2005).

[39] `http://www.gsi.de`, Site visited: February 2009.

[40] `http://www-inj.gsi.de`, Site visited: June 2010.

[41] `http://www.gsi.de/beschleuniger/sis18/sis_e.html`, Site visited: June 2010.

[42] M. Steiner *et al.*, Nucl. Instr. and Meth. **A312**, 420 (1992).

[43] `http://www-linux.gsi.de/wolle/EB_at_GSI/FRSWORKING/FRS/GEISSEL/F09.pdf`, Site visited: August 2008.

[44] H. Geissel *et al.*, Nucl. Instr. and Meth. **B70**, 286 (1992).

[45] J. C. Maxwell, Philosophical Magazine **Volumes 21 and 23**, Series 3 (1861).

[46] H. A. Bethe, Ann. der Phy. **397**, 325 (1930).

[47] C. Scheidenberger *et al.*, Nucl. Inst. and Meth. **B142**, 441 (1998).

[48] `http://www-w2k.gsi.de/frs-setup/`, Site visited: February 2009.

[49] J. F. Knoll, *Radiation Detection and Measurement.* (Wiley, 1989).

[50] B. Voss *et al.*, Nucl. Instr. and Meth. **A364**, 150 (1995).

[51] `http://www.detectors.saint-gobain.com`, Site visited: February 2009.

[52] M. Pfützner *et al.*, Nucl. Instr. and Meth. **B86**, 213 (1994).

[53] http://www-w2k.gsi.de/frs/technical/FRSsetup/detectors/music.asp, Site visited: February 2009.

[54] R. Stelzer, Nucl. Instr. and Meth. **A310**, 103 (1991).

[55] http://www-linux.gsi.de/~weick/frs/mwpc.html, Site visited: February 2009.

[56] V. Hlinka *et al.*, Nucl. Instr. and Meth. **A419**, 503 (1998).

[57] S. Pietri *et al.*, Acta Phys. Pol. **B38**, 1255 (2007).

[58] http://www.xia.com/Manuals/DGF_UserManual.pdf, Site visited: August 2008.

[59] S. Agostinelli *et al.*, Nucl. Instr. and Meth. **A506**, 250 (2003).

[60] J. Allison *et al.*, IEEE Trans. on Nuc. Sci. **53 No. 1**, 270 (2006).

[61] The Geant4 simulation has been done by Konrad Steiger, Technische Universität München. December 2010.

[62] http://radware.phy.ornl.gov/gf3/gf3.html#5.3., Site visited: February 2009.

[63] http://www-w2k.gsi.de/frs/technical/daq/overview.asp, (Site visited: February 2009).

[64] K.-H. Schmidt *et al.*, Nucl. Instr. and Meth. **A260**, 287 (1987).

[65] A. H. Compton, Phys. Rev. **21, No. 5**, 483 (1923).

[66] Evaluated nuclear structure data file, http://www.nndc.bnl.gov/ensdf/, Site visited: 2010.

[67] A. R. Poletti *et al.*, Nucl. Phys. **A380**, 335 (1982).

[68] A. R. Poletti *et al.*, Phys. Rev. **C20**, 1768 (1979).

[69] A. R. Poletti *et al.*, Phys. Rev. Lett. **45**, 1475 (1980).

[70] K. H. Maier. *et al.*, Hyperfine Interactions. **9**, 87 (1981).

[71] A. R. Poletti *et al.*, Nucl. Phys. **A756**, 83 (2005).

[72] Conversion coefficient calculator, http://physics.anu.edu.au/nuclear/bricc/, Site visited: 2010.

[73] T. Kibédi *et al.*, Nucl. Instr. and Meth. **A589**, 202 (2008).

[74] A. R. Poletti *et al.*, Nucl. Phys. **A359**, 180 (1981).

[75] P. M. Davidson *et al.*, Nucl. Phys. **A560**, 822 (1993).

[76] A. P. Byrne *et al.*, Nucl. Phys. **A448**, 137 (1986).

[77] J. R. Beene *et al.*, Hyperfine Interactions. **3**, 397 (1977).

[78] A. P. Byrne *et al.*, Phys. Rev. **C42**, R6 (1990).

[79] O. Häusser *et al.*, Phys. Lett. **B63**, 279 (1976).

[80] M. E. Debray *et al.*, Phys. Rev. **C48**, 2246 (1993).

[81] A. P. Byrne *et al.*, Nucl. Phys. **A567**, 445 (1994).

[82] A. E. Stuchbery *et al.*, Nucl. Phys. **A548**, 159 (1992).

[83] Y. Yamazaki *et al.*, Phys. Rev. Lett. **33**, 1614 (1974).

[84] K. H. Maier *et al.*, Jour. Phys. **32** (1971).

[85] K. H. Maier *et al.*, Report No. UCLR-20426,P21, 1971 (unpublished).

[86] P. Kuusiniemi *et al.*, Eur. Phys. Jour. **A30**, 551 (2006).

[87] A. E. Stuchbery *et al.*, Nucl. Phys. **A641**, 401 (1998).

[88] A. Maj *et al.*, Nucl. Phys. **A509**, 413 (1990).

[89] T. Weckstrom *et al.*, Z. Phys. **A321**, 231 (1985).

[90] A. M. Baxter *et al.*, Nucl. Phys. **A515**, 493 (1990).

[91] O. Häusser *et al.*, Nucl. Phys. **A273**, 253 (1976).

[92] B. Fant *et al.*, Nucl. Phys. **A429**, 296 (1984).

[93] L. O. Orlin *et al.*, Z. Phys. **A322**, 463 (1985).

[94] I. Bergstrom *et al.*, Z. Phys. **A273**, 291 (1975).

[95] H.-E. Mahnke *et al.*, Phys. Lett. **B122**, 27 (1983).

[96] V. Rahkonen and T. Lonnroth, Z. Phys. **A322**, 333 (1985).

[97] G. D. Dracoulis *et al.*, Nucl. Phys. **A462**, 576 (1987).

[98] V. Rahkonen *et al.*, Z. Phys. **A284**, 353 (1978).

[99] P. Carle *et al.*, Hyperfine Interactions **34**, 777 (1987).

[100] S. Bayer *et al.*, Nucl. Phys. **A694**, 3 (2001).

[101] K. H. Maier *et al.*, Phys. Lett. **B35**, 401 (1971).

[102] G. D. Dracoulis *et al.*, Phys. Rev. **C80**, 054320 (2009).

[103] D. Horn *et al.*, Phys. Rev. Lett. **39**, 389 (1977).

[104] A. E. Stuchbery *et al.*, Nucl. Phys. **A486**, 397 (1988).

[105] A. E. Stuchbery *et al.*, Nucl. Phys. **A482**, 692 (1988).

[106] G. D. Dracoulis *et al.*, Nuc. Phys. **A467**, 305 (1987).

[107] T. Lönnroth *et al.*, Phys. Rev. **C27**, 180 (1983).

[108] G. D. Dracoulis *et al.*, Eur. Phys. Jour. **A40**, 127 (2009).

[109] D. Kanjilal *et al.*, Nucl. Phys. **A842**, 1 (2010).

[110] J. J. Ressler *et al.*, Phys. Rev. **C69**, 034331 (2004).

[111] K. Hauschild *et al.*, Nucl. Instr. and Meth. **A560**, 388 (2006).

[112] F. B. Hessberger *et al.*, Eur. Phys. Jour. **A22**, 253 (2004).

[113] T. Kohno *et al.*, Phys. Rev. **C33**, 392 (1986).

[114] D. J. Decman *et al.*, Z. Phys. **A310**, 55 (1983).

[115] S. Myalski *et al.*, Acta Phys. Pol. **B40**, 879 (2009).